Tampere University

Luis Vallejo Rodríguez

NUMERICAL AND EXPERIMENTAL EVALUATION OF DYNAMIC SHEAR RESPONSE OF A HIGH ENTROPY ALLOY

Master's thesis
Faculty of Engineering and Natural Sciences
Mikko Hokka
Matti Isakov
December 2021

ABSTRACT

Luis Vallejo Rodríguez: Numerical and Experimental Evaluation of Dynamic Shear Response of a High Entropy Alloy
Master's thesis
Tampere University
Material Science
December 2021

In this thesis two multi-principal element alloys, also known as high-entropy alloys (HEAs), were studied to evaluate their shear responses under quasi-static and dynamic loading conditions by means of geometries designed with the purpose of promoting shear localization at the gage section. Cantor and $Al_{0.3}$CrFeCoNi HEAs can replace the alloys used nowadays by mining, construction, railroads, automobile and defense industries. A common phenomenon on materials used in these applications is shear localization and adiabatic shear band (ASB) generation, which has been scarcely studied; however, only shear specimen geometries that did not allow the direct observation of shear localization have been used.

With the aim of speeding up the study of shear geometries and designing of new ones, a first simulation approach with the Finite Element Methods tool Abaqus is done based on the manufacturing conditions of the HEAs (2 mm thick Cantor plate and 8 mm $Al_{0.3}$CrFeCoNi plate) and the available equipment for the characterization the material response (Split Hopkinson Pressure Bars, Split Hopkinson Tensile Bars and 2D-DIC). The designs did not include the input and output bars from the SHB set-ups and afterwards, they were adjusted to quasi-static loading conditions and modified to optimize shear localization at the gage section. The resulting specimen geometries are variations of the S-shaped specimen with a thin gage section (Cantor HEA, tested in SHTB), and the flat-hat specimen ($Al_{0.3}$CrFeCoNi HEA, tested in SHPB); five specimens of each design were manufactured and tested in quasi-static and dynamic loading conditions, with shear strain rates ranging from 0.0025 s^{-1} to 11000 s^{-1} for the $Al_{0.3}$CrFeCoNi specimens and from 0.001 s^{-1} to 8500 s^{-1} for the Cantor specimens. The data from the experiments was processed with Matlab. The tests were coupled with 2D-Digital Image Correlation tool for analyzing strain field evolution in the gage section while the experiments were running to compare the strain fields obtained from there with those from the simulations. The data from the DIC measurements was processed with LaVision software.

In both DIC and Abaqus, the design used for testing the Cantor HEA concentrated the strains at the gage section, uniformly throughout its thickness and forming a shear band; however, as the yield stress does not increase with the strain rate in dynamic loading conditions, more tests are required. The design used for testing the $Al_{0.3}$CrFeCoNi HEA concentrates most of the strains at the gage section also, but the strains also spread out of the gage section and are not uniformly distributed throughout the specimen thickness because the gage section was not milled down as in the case of the Cantor specimen design. Furthermore, the material response of $Al_{0.3}$CrFeCoNi HEA was not in concordance with that from previous investigations, except for the yield stress obtained at low strain rate, which was considerably higher, decreasing considerably the strain-rate sensitivity of the alloy. Regarding the shear stress – shear strain curves from the model, using fitting models such as Johnson-Cook model, studying the mesh size sensitivity and including fracture modes in the simulations would be recommended for better agreement with the experimental curves.

Keywords: High-Entropy Alloys, Cantor HEA, Al0.3CrFeCoNi HEA, ASBs, high strain rate, dynamic shear testing, Split Hopkinson Pressure Bar, Split Hopkinson Tensile Bar, specimen design, shear geometries, flat-hat, FEM, Abaqus, Digital Image Correlation.

PREFACE

I would like to thank the people from the material science unit for the chance they gave me of joining their team, and big thanks to Mikko Hokka and Matti Isakov for their patience, support and guidance in this amazing project. Great thanks to my family and friends from Spain, you have shown me that being a couple of countries away does not prevent us for being as close as always; your care and support has filled me with joy every single day, especially the loneliest. Finally, great thanks to Veera (and her family), Aleksi and Betül, whose honest smiles and cheerful eyes have shown me that the dark days of winter can be as good as the long sunny days of summer, quite an achievement considering we are talking about Finland. I consider you as a family and I cannot be happier to have met you.

Tampere, 8th December 2021

Luis Vallejo Rodríguez

CONTENTS

LIST OF FIGURES

LIST OF SYMBOLS AND ABBREVIATIONS

HEA	High-Entropy Alloy
ASB	Adiabatic Shear Band
BCC	Body Centered Cubic
FCC	Face Centered Cubic
SHB	Split Hopkinson Bars
Cantor	FeCrMnNiCo HEA
XRD	X-Ray Diffraction
MD	Mean Difference
HESA	High-Entropy Superalloy
HERA	High Entropy Refractory Alloy
HSS	High Strength Steel
AHSS	Advanced HSS
TWIP	Twinning Induced Plasticity
TRIP	Transformation Induced Plasticity
MBIP	Microband Induced Plasticity
SFE	Stacking Fault Energy
SHTB	Split Hopkinson Tension Bar
SHPB	Split Hopkinson Pressure Bar
TSHB	Torsion Split Hopkinson Bar
UTM	Universal Testing Machine
DIC	Digital Image Correlation
IR	Infrared
VSG	Virtual Strain Gage
LED	Light Emitting Diode
FEA	Finite Element Analysis
FEM	Finite Element Method
ALLEN	All energy variables
ALLKE	Kinetic energy
PEEQ	Equivalent plastic strain

F	Force
m	Schmid factor
$\bar{m}$	Averaged Schmid factor
A_s, A_0	Cross-sectional areas of the slip plane
A_{cs}	Cross-sectional area
A_{bar}	Cross-sectional area of the SHB bars
L_s	Width of the age section
A_{gs}	Cross-sectional area of the gage section
Q	Shear force
k, h	Describe the shear angle generated at the geometry during shear deformation
k_0	Relative velocity to generate a specific strain rate
s	Second
N	Newton
Pa	Pascal
T	Temperature
T_0	Initial temperature
T_m	Melting temperature
A, B, n’	Material parameters (constant)
C_v	Heat capacity
S	Entropy in a system

k	Boltzmann's constant
w	Possible micro-states corresponding to the macroscopic state of the system
ln	Natural logarithm
ΔS_{mix}	Entropy of mixing
ΔH_{mix}	Enthalpy of mixing
ΔG_{mix}	Gibb's Free energy of mixing
x_1, x_2	Atomic fractions
R	Ideal gas constant
n	Number of elements in an equi-molar alloy
u	Displacement vector
$\dot{\mathbf{u}}$	Velocity vector
$\ddot{\mathbf{u}}$	Acceleration vector
M	Mass/lumped matrix
C	Damping matrix
K	Stiffness matrix
L_{lim}	Characteristic length of the smallest element dimension in the model
c	Dilatational wave speed in the material
E	Young's modulus
G	Shear modulus
p	Contact pressure
M'	Bending moment
Z	Impedance
F_{input}, F_{output}	Force at the SHB-specimen interface
U_{input}, U_{output}	Displacement at the SHB-specimen interface
V_{input}, V_{output}	Velocity at the SHB-specimen interface
λ	Angle between the applied force and the slip direction
Φ	Angle between the applied force and the slip plane normal
σ	Stress
σ_y	Yield strength
σ_{eff}	Maximum effective stress
ε_{eff}	Maximum effective strain
τ	Shear stress
τ_{pl}	Plastic shear stress
τ_{crit}	Critical shear stress
Υ	Shear strain
Υ_{pl}	Plastic shear strain
Υ_c	Critical shear strain
$\dot{\Upsilon}$	Shear strain rate
$\dot{\boldsymbol{\varepsilon}}$	Strain rate
v	Poisson's ratio
ρ	Density of the material
β	Efficiency of the conversion of work into heat
μ	Friction coefficient
ε_i	Incident pulse
ε_r	Reflected pulse
ε_t	Transmitted pulse

1. INTRODUCTION

The concept high entropy alloy or HEA was successfully introduced in 2004 [1], [2] as an alternative to conventional alloys, where there is one (sometimes two) main element tuned with minor amounts of secondary alloying elements. HEAs can be defined according to two guidelines: being composed of at least five major elements in near equi-atomic proportions; or having a high configurational (or mixing) entropy. The important principle behind multiple principal element HEAs is having high entropy of mixing to ease the formation of solid solution phases. At the same time, a high entropy of mixing inhibits the formation of intermetallic compounds and complicated and brittle structures. [3]

This thesis starts defining shear localization and the effect of strain rate on material properties; continuing with the origin of HEAs as they are known nowadays and the description of the four core effects of HEA that make them so interesting for multiple applications. Among the different types of HEAs, Cantor and $Al_{0.3}$FeNiCrCo bring interest as they have interesting properties at high strain rates. These alloys are lighter, have a better performance and are supposed to experience shear localization at higher strain rates than other alloys used for the same applications, such as high manganese steels. However, shear localization in ductile materials has not been understood completely yet and has been scarcely investigated in these HEAs.

Conventional dog-bone and solid cylindrical specimens can experience shear localization while being subjected to monotonic tension or compression, but they are not designed to force shear localization and study this phenomenon. Instead, using some specific shear geometries allow fulfilling such purpose.

In this thesis, some of those specimen geometries are presented, with special focus on those compatible with the available testing devices, Split Hopkinson Pressure and Tension Bars for dynamic loading testing and Universal Testing Machine for quasi-static loading testing. The most suitable geometries based on the available resources (2 mm thick Cantor plate, 7 mm thick $Al_{0.3}$FeNiCrCo plate and data from monotonic compression tests of Cantor alloy [4]) were virtually tested via Finite Element Analysis tool Abaqus at different strain rates before performing the experimental tests to reduce prototyping costs while improving the design of the specimens. The experimental tests were coupled with Digital Image Correlation tool for in-situ material characterization of shear localization in the HEAs.

2. SHEAR LOCALIZATION AND EFFECT OF STRAIN RATE ON MATERIAL PROPERTIES

This chapter describes the effect of strain rate on material properties and how shear localization is produced, covering the conceptual and analytical description of adiabatic shear bands (ASB) formation.

2.1 Effect of strain rate on material properties

Crystalline materials such as metals, have one main mechanism of plastic deformation, dislocations glide, and the resistance to their movement determines materials macroscopic strength [5], [6]. Movement of dislocations occurs with the coordinated jump of individual atoms from one low energy state (or Peierls valley) to another, overcoming a Peierls stress or energy barrier [7]–[9]. The atoms can overcome the energy barrier with their own thermal vibrations or by applying an external mechanical energy, i.e., shear stress. [7], [10]

Obstacles hinder or stop the movement of dislocation, and can be classified in short range or long range. Short range obstacles (e.g., solute atoms), also known as thermal obstacles, could be overcome if the thermal energy is high enough so dislocation atoms reach the next Peierls valley by atomic vibration. Figure 2.1 shows the external (stress) energy required at different temperatures for overcoming thermal obstacles. Long range obstacles (e. g., particles, grain boundaries) are barely affected by thermal vibration, they are usually called “athermal”. [7], [8]

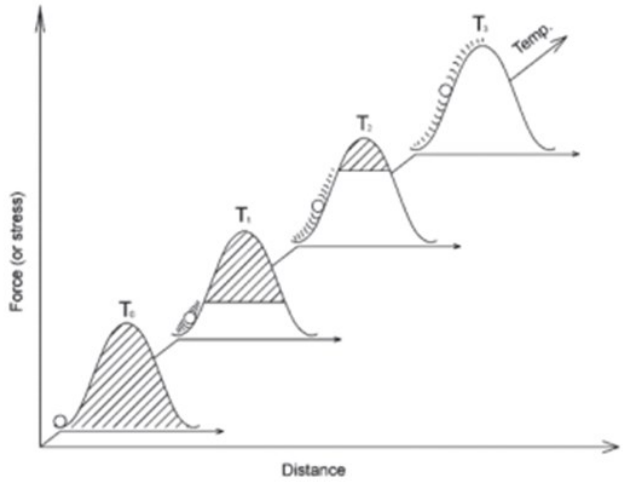

Figure 2.1 *Thermal and mechanical energies needed to overcome a thermal obstacle. Shaded area represents the mechanical energy required while the unshaded is the represents the thermal energy of the atom.* [7], [8]

The strength of athermal obstacles decreases slightly while increasing temperature due to the temperature dependence of the shear modulus. The strength of thermal obstacles decreases with increasing the temperature and increases with the strain rate. At higher strain rates, dislocations move faster and the probability for them to receive enough thermal vibration is low. Hence, obstacles need to be overcome by increasing the amount of external mechanical energy. Figure 2.2 shows the temperature and strain rate dependence of thermal and athermal components and the flow stress of the material. Increasing the strain rate increases the flow stress of the material, its yield strength, ultimate tensile strength and hardness. [11]

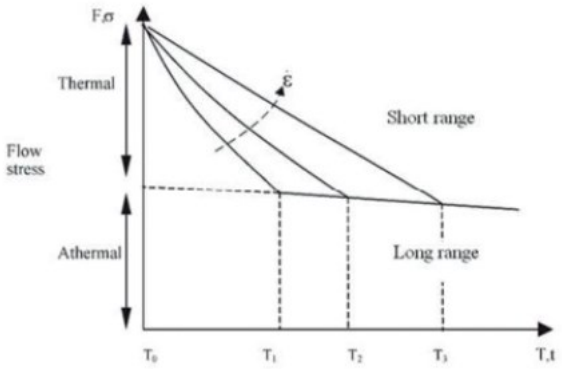

Figure 2.2 *The effect of strain rate and temperature on the flow stress of thermal and athermal obstacles.* [7]

The effect of strain rate and temperature differs in body centered cubic (BCC) and face centered cubic (FCC) metals [10]. The strain hardening rate is independent of the strain

rate in BCC metals because Peierls-Nabarro stresses (main thermal obstacle caused by lattice friction), meaning that the strain hardening rate is independent of the strain rate. On the other hand, the main thermal obstacles in FCC lattices are jog formation and intersections with other dislocations [10]. Increasing the strain means higher dislocation density and more jog formation which worsen dislocation movement; therefore, the strength of the material increases [11]. Figure 2.3 shows the effect of strain rate and temperature in the stress-strain curve of BCC and FCC metals.

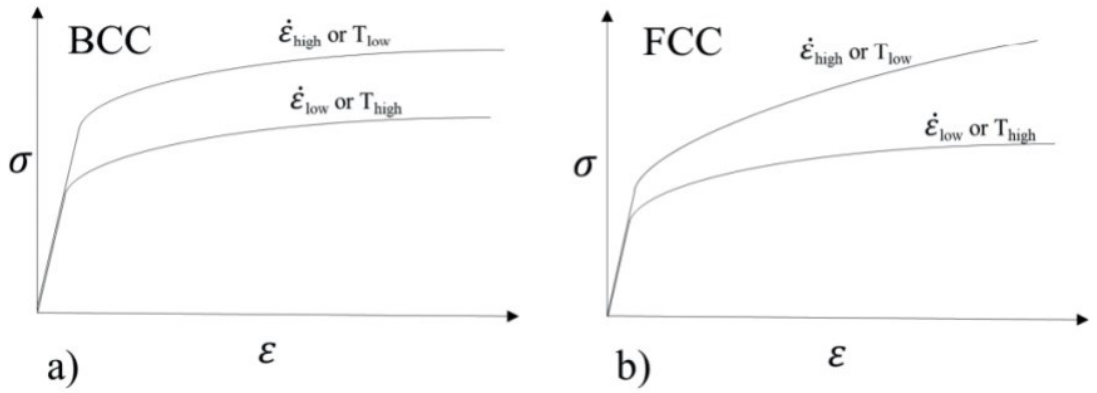

Figure 2.3 *Effect of temperature and strain rate on stress-strain curve of BCC and FCC metals. [7]*

2.2 Shear localization

Material testing can lead to plastic deformation and shear localization [11]. This is due to the conversion of uniaxial stresses into stresses applied over the slip planes. Once the critical resolved shear stress (τ_{CRSS}) is surpassed, dislocations glide over the crystallographic slip planes and produce plastic deformation in the direction of the Burger's vector [11]. In the case of a monocrystals subjected to uniaxial traction, the existing relationship between the τ_{RSS} and the external applied load is

$$\tau_{RSS} = \frac{F \cdot \cos\phi}{A_s} = \frac{F}{A_0} \cos\phi \cos\lambda = \frac{\sigma}{m} \qquad 1$$

where F is the applied force, A_S and A_0 are the cross-sectional areas of the slip plane and the specimen respectively; φ is the angle between the applied force F and the slip plane normal and λ is the angle between the applied force F and the slip direction; m is known as the Schmid factor $m = (\cos\varphi * \cos\lambda)^{-1}$, characteristic for each slip plane Figure 2.4 illustrates it.

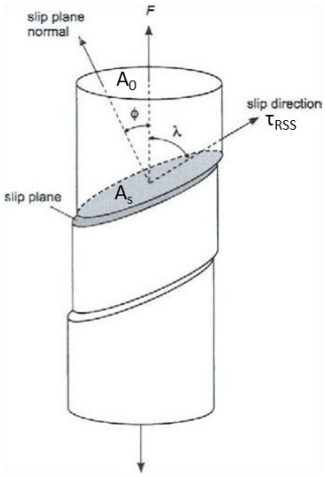

Figure 2.4 *Schematic representation of resolved shear stress in tensile test with a single crystal specimen. [12]*

Nevertheless, polycrystals have higher flow stresses due to the different orientations of each individual crystal of the aggregate with respect the tensile axis. This is because polycrystals have an average Schmid factor ($\bar{m}$), which results from averaging the Schmid factor's values of the least favourable oriented grains in the strain direction. For fcc structures $\bar{m}$ is 3.06, while for bcc structures, $\bar{m}$ equals 2.75. [12]

Macroscopically, ideal simple shear deformation considers out of plane deformations to be zero and the displacement in one direction only, as a linear function of the transverse coordinate. Figure 2.5 illustrates it.

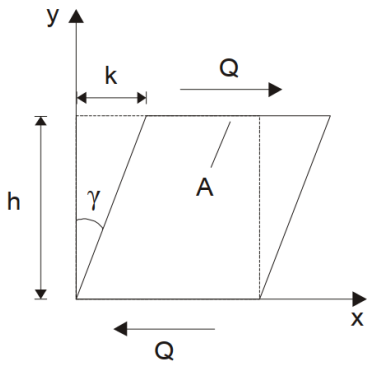

Figure 2.5 *Illustration of simple shear.*

Shear stress (τ), shear strain (γ) and shear strain rate ($\dot{\gamma}$) are described in the following equations,

$$\boldsymbol{\tau = \frac{Q}{A_{cs}}} \qquad \textbf{2}$$

$$\boldsymbol{\gamma = \frac{k}{h}} \qquad \boldsymbol{\dot{\gamma} = \frac{\dot{k}}{h}} \quad \textbf{3}$$

where Q is the applied shear force, A_{cs} is the cross-sectional area, k and h describe the angle change of the geometry during deformation and $\dot{k}$ is the relative velocity for generating a specific strain rate.

Under the adequate circumstances, any material exhibits shear band formation [13]. They are thermo-viscoplastic instabilities generated in those regions of the material where plastic deformation is highly concentrated [14], [15]. In military components, shear bands establish the shear failure path of the component (e.g., clean plugging of target in Figure 2.6-a) or the size, distribution and pattern of the fragments (Figure 2.6-c). In manufacturing applications (Figure 2.7), the shear bands formed introduce internal flaws in the final product, affecting its final properties. Nevertheless, the presence of adiabatic shear bands enables high machining rate operations, allowing smooth clean cuts and breaking up the chips formed by the cutting tool.

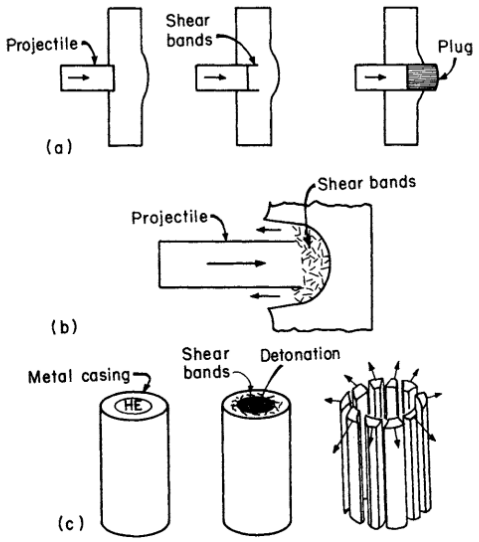

Figure 2.6 *Formation of shear bands in dynamic deformation events (military applications): (a) defeat of armor by plugging; (b) shear bands breaking up projectile; (c) shear bands determining fracture in exploding cylinders. [14]*

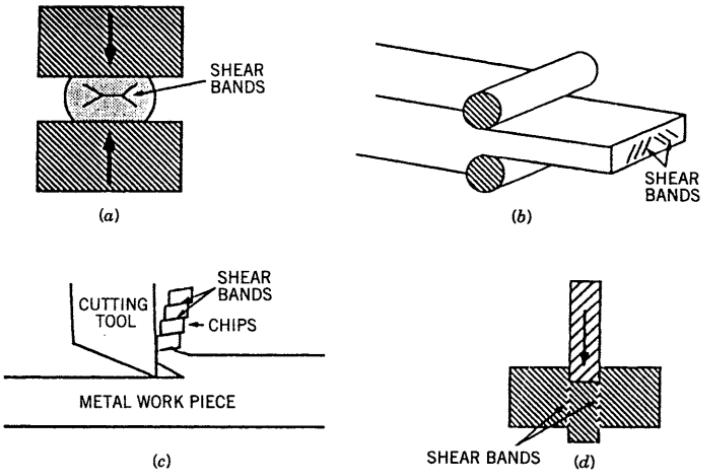

Figure 2.7 *Shear localization in plastic-forming processes: (a) upset forging; (b) rolling; (machining; (d) punching and shearing.* [14]

Zener and Hollomon [16] provided a simple explanation for the formation of shear bands. When a material is deformed adiabatically, material strength increases due to strain hardening and decrease because of the temperature rise. Figure 2.8 explains the mechanics of shear band formation. Before reaching a certain strain γ_c deformation is homogenously distributed, but with γ_c, a small fluctuation appears, accentuated as strain increases and leading to the localization of deformation in a band. At γ_c thermal softening overcomes work (or strain) hardening and the component reached its maximum strength. Marchand and Duffy [17] confirm the mentioned schematic description.

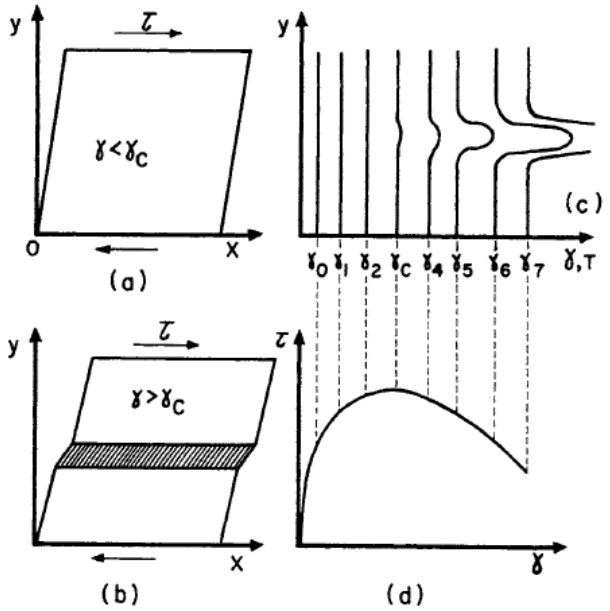

Figure 2.8 *Formation of shear instability when a parallelepiped is sheared by stress τ in an adiabatic mode: a) homogeneous shear; b) shear instability; c) strain (or temperature) profiles, localization starts at γ_C: d) adiabatic stress-strain curve.* [14]

Recht [18] expressed the competition between work hardening and thermal softening quantitatively with the following equations:

$$\boldsymbol{\tau = f(T, \gamma)}$$
$$\boldsymbol{d\tau = (\frac{d\tau}{dT})_{\gamma} dT + (\frac{d\tau}{d\gamma})_{T} d\gamma} \qquad \textbf{4}$$

$$\boldsymbol{\frac{d\tau}{d\gamma} = (\frac{d\tau}{dT})_{\gamma} \frac{dT}{d\gamma} + (\frac{d\tau}{d\gamma})_{T}}$$

Adiabatic shear bands (ASB) can form when material "softens", considering $\frac{d\tau}{d\gamma}$=0 the condition of instability:

$$\boldsymbol{\frac{d\tau}{d\gamma} \leq 0}$$
$$\boldsymbol{(\frac{d\tau}{d\gamma})_{T} = -(\frac{d\tau}{dT})_{\gamma} \frac{dT}{d\gamma}} \qquad \textbf{5}$$

Introducing strain rate dependence and generalizing the expression:

$$\boldsymbol{\tau = f(T, \gamma, \dot{\gamma})}$$
$$\boldsymbol{d\tau = (\frac{d\tau}{d\gamma})_{T,\dot{\gamma}} d\gamma + (\frac{d\tau}{d\dot{\gamma}})_{T,\gamma} d\dot{\gamma} + (\frac{d\tau}{dT})_{\gamma,\dot{\gamma}} dT} \qquad \textbf{6}$$

$$\boldsymbol{\frac{d\tau}{d\gamma} = (\frac{d\tau}{d\gamma})_{T,\dot{\gamma}} + (\frac{d\tau}{d\dot{\gamma}})_{T,\gamma} \frac{d\dot{\gamma}}{d\gamma} + (\frac{d\tau}{dT})_{\gamma,\dot{\gamma}} \frac{dT}{d\gamma}}$$

when the strain rate is constant, Equation 5 is used. With the analytical expressions for $(\frac{d\tau}{d\gamma})_T$ and $(\frac{d\tau}{dT})_\gamma$, it is possible to obtain the stress, strain, temperature and instability strain under adiabatic conditions. For isothermal work hardening, the power law is often used

$$\boldsymbol{\tau = A + B\gamma^{n'}} \qquad \textbf{7}$$

where A, B and n' are temperature dependent, although they are assumed to be constant.

The conversion of deformation energy into temperature considering material heat capacity C_v and density ρ allows the calculation of the increase in temperature generated by a shear strain increment:

$$\boldsymbol{dW = \tau d\gamma}$$
$$\boldsymbol{dT = \frac{\beta}{\rho C_v} dW}$$
$$\boldsymbol{dT = \frac{\beta}{\rho C_v} \tau d\gamma}$$
$$\boldsymbol{\frac{dT}{d\gamma} = \frac{\beta}{\rho C_v} \tau = \frac{\beta}{\rho C_v} (A + B\gamma^{n})} \qquad \textbf{8}$$

Integration yields

$$T = \frac{\beta}{\rho C_v}\int_0^{\gamma} \tau d\gamma \quad 9$$

where C_v is considered as constant and β is the efficiency of the conversion of work into heat (0.9-1).

A linear relationship expresses thermal softening component as follows

$$\tau_T = \tau_{T0}\frac{T_m - T}{T_m - T_0} \quad 10$$

where τ_T at temperature T decreases linearly from τ_{T0} at the initial temperature T_0 to the melting point T_m. Substituting Equation 7 into Equation 10

$$\tau_T = (A + B\gamma^n)\frac{T_m - T}{T_m - T_0}$$
$$d\tau = \frac{-(A+B\gamma^n)}{T_m - T_0} dT \ (constant\ \gamma) \quad 11$$

Substituting Equations 1 and 11 into Equation 4

$$\frac{d\tau}{d\gamma} = \left[\frac{-(A+B\gamma^n)}{T_m - T_0}\right]\left[\frac{\beta}{\rho C_v}(A + B\gamma^n)\right] \quad 12$$

This equation allows determining at which γ_c instability occurs. Lindholm and Johanson [19] proved the good correlation between the experimental γ_c and the theoretical values.

More advance constitutive models require more comprehensive formulations. They incorporate in the mathematical expressions perturbations (in stress, strain or temperature), the rate at which localization develops, strain rate hardening, heat conduction out of the shear band and geometric softening. The size of ASBs depends on the material and its history, but it can be estimated and is in the range of the μm. [11]

The mentioned constitutive models have been implemented for the study of shear band propagation using Finite Element Methods [20], [21]. However, characterizing the material strain rate and using small enough element mesh size and regularization methods are critical parameters for the correct simulation of ASB. Otherwise, simulations could reach prohibitive computational times. [22]

Finally, some studies analyse the relationship between ASB formation and dynamic recrystallization (DRX) [15]. DRX is a microstructural softening phenomenon that causes the rearrangement of the microstructure in materials undergoing high strain rate and temperature deformations [22]. Material loses mechanical strength and softens in the ASB region. There are some discrepancies in the initiation mechanism of DRX and the influence of temperature in the process. [23], [24]

3. HIGH-ENTROPY ALLOYS

This chapter describes the origin of the concept of high-entropy alloys together with their characteristic four core effects that make these alloys so promising. It includes a brief explanation of the different manufacturing routes that can be taken to produce the high-entropy alloys. The chapter concludes explaining some different applications where high-entropy alloys can be used, paying special attention to the Cantor and $Al_{0.3}CrFeCoNi$ high-entropy alloys, object of study in this thesis.

3.1 Origin and classification

In 2004, Jien-Wei Yeh et al. [1] and Brian Cantor et al. [2] published two papers that set a new milestone in the history of alloy development. Both successfully introduced the concept of 'multi-principal-element alloys' (MPEAs), known nowadays as high-entropy alloys (HEAs).

Cantor's research started with the study of two alloys composed of 20 and 16 elements in equal atomic proportions, 5 at. % and 6.25 at. % respectively. The resultant alloys were multiphase and brittle, but in both cases, there was a stable fcc phase particularly rich in the transition metals Fe, Co, Mn, Cr and Ni. Further study of a five component $Fe_{20}Cr_{20}Mn_{20}Ni_{20}Co_{20}$ alloy showed that forms an fcc solid solution that solidifies dendritically and can dissolve significant amounts of other transition metals like Nb, Ti and V. However, other elements with higher electronegativity such as Ge and Cu are excluded from the fcc primary phase into interdendritic regions. Cantor et al. [2] concluded that: "The total number of phases is always well below the maximum equilibrium number allowed by the Gibbs phase rule, and even further below the maximum number allowed under non-equilibrium solidification conditions." [2]

In 1995, Yeh et al. [25] began designing multicomponent alloys in equimolar or near-equimolar ratios. The alloy was based on the concept of high mixing entropy, which lowers the free energy of the system. The addition of passive elements such as Cr and Mo enhanced the corrosion resistance of the alloys. Yeh [25] also suggests that the high-entropy effect, the sluggish diffusion effect and lattice distortion effect are present in this kind of alloy. After further study, they provided experimental results and related theories that clarify the concept of HEAs. Their work also showed the suitability of these alloys for many potential applications due to their promising properties.

Different HEAs emerged from the growing number of investigations around this novel field. Hence, some studies have attempted to classify the different types of HEAs: [26]–[28]

- Transition metal based HEAs, like CrMnFeCoNi.
- Refractory HEAs, whose main elements are V, Cr, Nb, Ti, Hf, Mo, W and Ta.
- Low-density HEAs, where the main elements are Li, Be, Al, Mg, Si, Ti, Sc, Sn and Zn.
- Ceramic HEAS, which include metal diborides [29], oxides [30] and perovskite structures. [31]
- Other HEAs, like Lanthanide HEAs, precious metals [26] (for catalysis applications), bronzes and brasses; alloys whose purpose is reaching higher levels of strength via concentrated solid solutions.

3.2 HEAs core effects

Physical metallurgy establishes relationships between processing, composition, physical properties, mechanical properties, crystal structure and crystal microstructure [32], [33]. Such relationships are thermodynamics, kinetics, deformation theory, solid state physics, and different other theories. Figure 3.1 shows how HEAs core effects affect the conventional physical metallurgy principles.

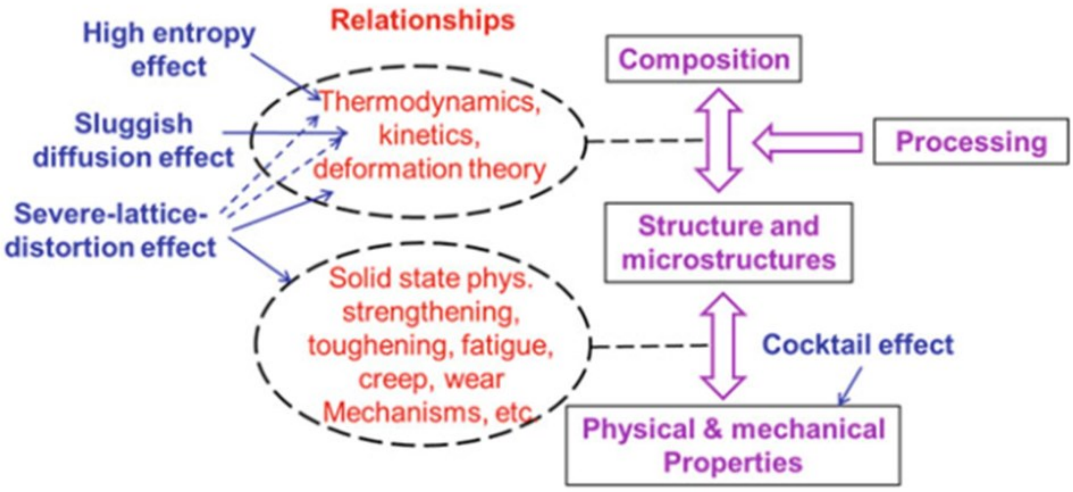

Figure 3.1 *Influence of the HEA's four core effects on the physical metallurgy.* [3]

Depending on the source, there are from four [3] to five [10] aspects or core effects of the HEAs. The four core effects of the HEAs considered for this thesis are the high-

entropy effect, the lattice-distortion effect, the sluggish diffusion effect, and the “cocktail” effect. The fifth core effect is the short-range order effect, which has been sparsely verified by experiments [34]–[36]. Therefore, including short-range order effect as a HEA core effect is controversial.

3.2.1 High entropy effect

Entropy is a term that Boltzmann developed, in terms of statistical mechanics, for analysing the thermodynamic stability of the microscopic components in alloys [37]–[40]. It was stated a linear dependence between the entropy of a system, S, and the natural logarithm of the number, w, of the possible micro-states corresponding to the macroscopic state of the system:

$$\boldsymbol{S = k \cdot ln\, w} \qquad \textbf{13}$$

where k Boltzmann’s constant (k = 1.38 x 10-23 $J \cdot K^{-1}$). If the system is composed of two components with atomic fractions x_1 and x_2, the entropy of mixing derived from Stirling’s approximation is:

$$\boldsymbol{\Delta S_{mix} = -k \cdot (x_1 \cdot ln\, x_1 + x_2 \cdot ln\, x_2)} \qquad \textbf{14}$$

For a random n-component solid solution, the ideal mixing entropy per mole is:

$$\boldsymbol{\Delta S_{mix} = -R \cdot \sum_{i=1}^{n} x_i \cdot ln\, x_i} \qquad \textbf{15}$$

where R is the gas constant (R = NA · k = 8.314 J/(K·mol), NA is Avogadro’s number) and considering for the mixing entropy the dominant factor to be configurational entropy, out of their four contributions: configurational, vibrational, magnetic dipole and electronic randomness [1]. In case of an equi-atomic alloy, $x_i = 1/n$, resulting in:

$$\boldsymbol{\Delta S_{mix} = -R \cdot ln(1/n) = -R \cdot ln(n)} \qquad \textbf{16}$$

where n is the number of elements that comprise the equi-molar alloy. The Gibbs free energy is expressed as:

$$\boldsymbol{\Delta G_{mix} = \Delta H_{mix} - T \cdot \Delta S_{mix}} \qquad \textbf{17}$$

where ΔH_{mix} is the mixing enthalpy, T is the temperature expressed in Kelvin and ΔS_{mix} is the mixing entropy from Equation 16. Only ΔH_{mix} and ΔS_{mix} determine the equilibrium state of the alloy in this analysis to simplify it; if lattice distortion effect caused by atomic size difference is considered, adding an extra term would be necessary [41]. If $\Delta S_{mix} < \Delta H_{mix}$, the system tends to order. If ΔH_{mix} is positive, atoms precipitate into segregates or tend to spinodal decomposition [1]. If ΔH_{mix} is negative, atoms form compounds. On the other hand, atoms form a solid solution occupying random positions in the crystal lattice if $\Delta S_{mix} > \Delta H_{mix}$ [42]. A high entropy of mixing also enhances the

synthesis, processing, analysis, manipulation, and use of HEAs [3] [1], [42]. Figure 3.2 (left) represents how the mixing entropy is a term that gains importance with the number of elements in the equimolar alloy as seen in Equation 16 [28]. In Figure 3.2 (right), alloys are classified based on their ideal mixing entropy values, according to Yeh et al. [1]

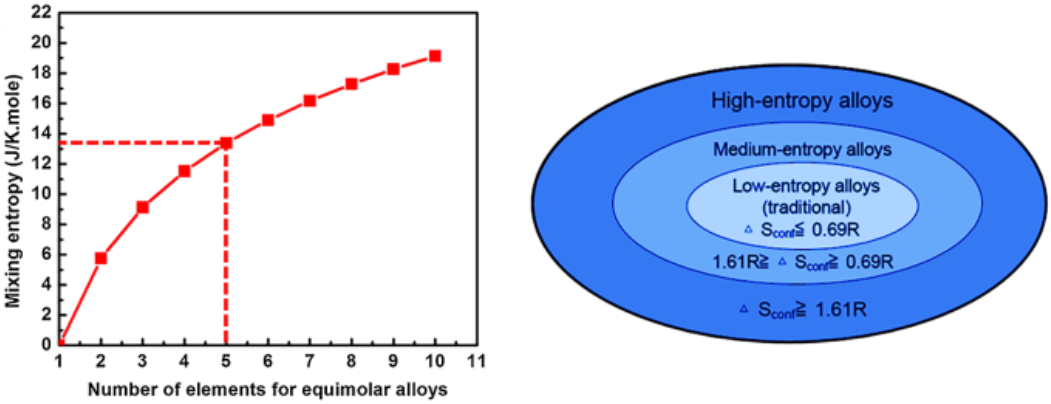

Figure 3.2 *(left) Mixing entropy of a system as a function of the number of equimolar elements. For a five equiatomic alloy, $\Delta S_{conf} = 1.61 \cdot R$. (right) Classification of the alloy systems based on the configurational (or mixing) entropy.* [28]

3.2.2 Severe lattice distortion effect

The unique atomic size of each element that composes the HEA leads to a severe lattice distortion and creates an irregular pattern of Peierls-Nabarro energy barriers that allow tuning HEA mechanical properties [43]. Figure 3.3 compares the Peierls-Nabarro energy barrier patterns of a diluted solid-solution and a HEA solid solution. [43]

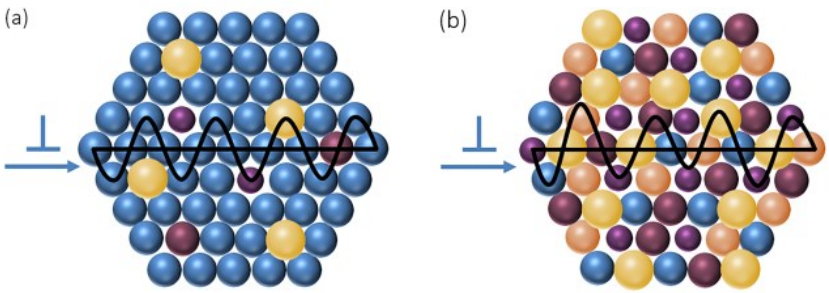

Figure 3.3 *Schematic drawing of dislocation motion overcoming Peierls-Nabarro energy barrier: a) in a dilute solid-solution; b) in a multicomponent solid solution.* [10]

However, lattice distortion effect causes a reduction of the peak intensity values when studying the HEAs under XRD, hindering their analysis. Figure 3.4 shows such phenomenon, investigated by Yeh et al. [44].

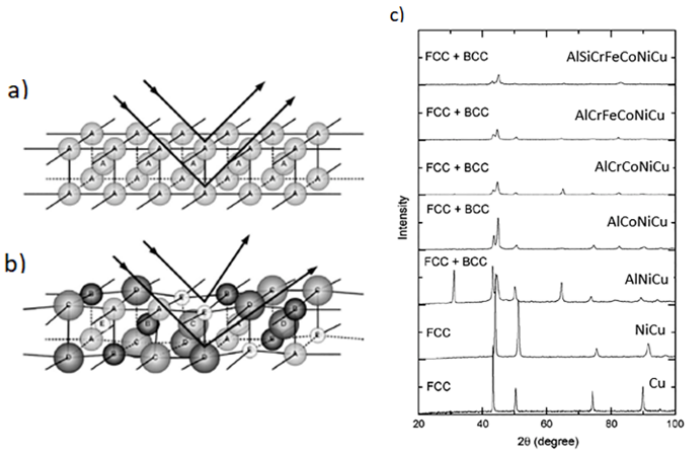

Figure 3.4 *(a) A schematic diagram of a perfect crystal structure with pure metals; (b) a schematic diagram of the structure of a HEA. The lattice distortion in (b) affects XRD intensities. (c) Experimental results of the XRD patterns as a function of the number of principal elements in the alloy.* [10]

Despite the sluggish diffusion and high-entropy effects promoting mixture and randomization in the crystal lattice, the atomic size the elements that compose the HEA is not large enough to cause the “confusion principle”. Such principle was firstly introduced by Turnbull [45], [46] and Greer [47], and stipulates that a higher number of elements in the alloy increases the probability of adopting an amorphous structure over a crystalline structure. [45], [46]

3.2.3 Sluggish diffusion effect

Atoms need to overcome a lattice potential energy barrier in order to migrate. Figure 3.5 shows the mean difference (MD) of migration from lattice site M to L, according to Tsai et al. [48] investigation. The MD in pure metals is close to zero as every atom is surrounded by its identical. When different atoms are added into the system (in equi-atomic ratio), apart from the fact of their unique atomic size, each one aims to keep a position consistent with the lowest lattice potential energy. This causes a severe “trapping” effect that increases the amount of energy required (activation energy) for migration. Therefore, diffusion in HEAs is sluggish and phase transformations are slower than in conventional alloys.

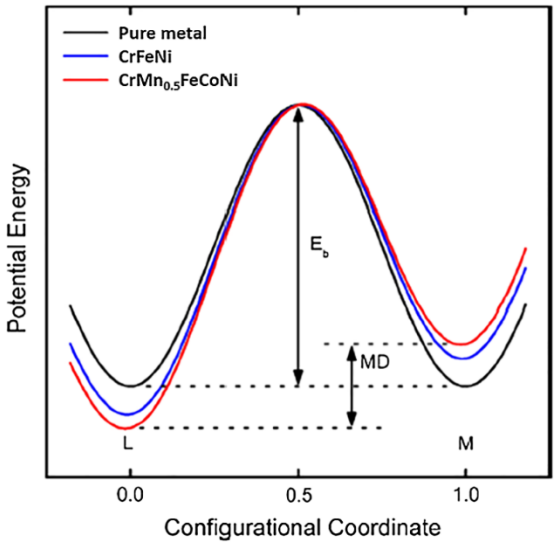

Figure 3.5 *LPE (Lattice Potential Energy) and mean difference of a Ni atom when migrates in pure Ni, CrFeNi alloy and CrMn0.5FeCoNi HEA. [48]*

This core effect provides great advantages to HEA alloys in terms of their mechanical properties. Obtaining a supersaturated state and fine precipitates, grain growth is slower, particle coarsening rate is reduced, recrystallization temperature is increased, and creep resistance is improved. [3]

3.2.4 Cocktail effect

Cocktail effect is a term without a rigorous scientific basis, proposed by Ranganathan [49]. In their work, it was stated that the properties of HEAs are not only the outcome of the basic properties of each element that it is composed of (following the mixture rule), but they are also the result of the mutual interaction between those atoms and the severe lattice distortion. Bulk metallic glasses, GUM alloys (Ti alloy with high elasticity, yield strength and ductility) and HEAs are examples of materials with unexpected and synergistic properties. [4]

3.3 Manufacturing routes

Figure 3.6 shows three major manufacturing routes for the synthesis of HEAs. Beginning with the route that produces HEAs from the liquid mix, the most common procedures are Bridgman solidification, laser cladding, laser melting, LENS (Laser Enhanced Net Shape forming), inductive melting, arc melting, and electric resistance melting. In the route that manufactures from the solid state, HEAs can be manufactured via high-pressure torsion, SPS (spark plasma sintering), mechanical alloying and the subsequent consolidation routes. The third route manufactures HEAs from the vapor state, including methods such

as sputtering, pulse laser deposition, molecular beam epitaxy and ion beam assisted deposition. [3], [50]

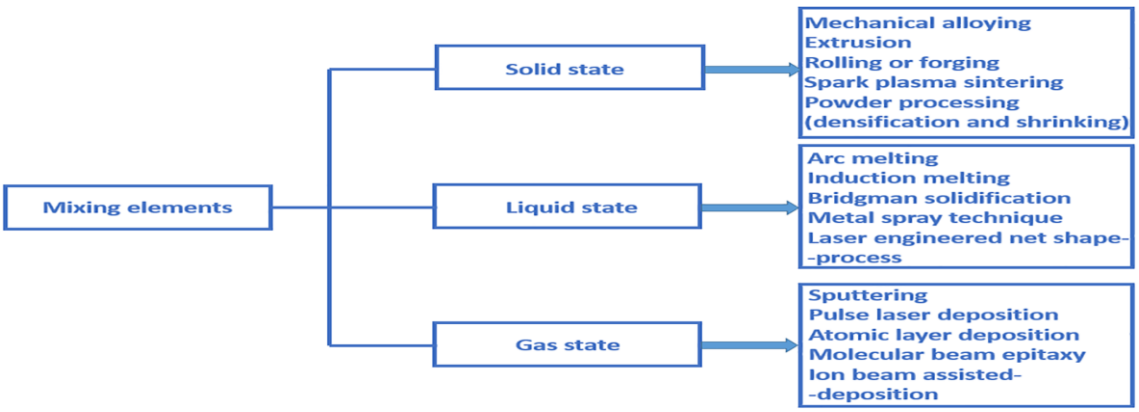

Figure 3.6 *Major manufacturing routes of HEAs.* [10]

3.4 Applications

The number of potential applications in which HEAs can be used is large, although they are still under investigation until they are fully understood, and their limitations properly defined. High entropy superalloys (HESAs) imitate the microstructure of conventional superalloys [51] [dispersion of coherent $L1_2$ γ', $Ni_3(Al,Ti)$ phase into the fcc γ matrix, i.e., superlattice] and offer materials with better mechanical properties at low and high temperature; higher creep resistance, thermal stability and castability, and with a density lower than 8 g/cm^3. [52]–[55]

High entropy refractories (HERAs) are alloys with a bcc microstructure particularly ductile under compression (exceeds 50%) and high strain rate. Other HERAs have better physical properties (lower density, higher melting temperature) and better mechanical properties (strength, hardness) at room temperature and high temperature. [56]–[61]

Some HEAs can also be used as cermets or binders due to their high hardness and toughness, corrosion and wear resistance and high temperature softening resistance. They have a better wetting capacity and toughness-hardness combination than conventional cermets and binders. [62]–[64]

Using HEAs as thin films, coating and diffusion barriers has been the objective of many researchers since HEAs appeared. Alloys such as $AlCoCrFeMo_{0.5}NiSiTi$ and $AlCrFeMo_{0.5}NiSiTi$ can be thermally sprayed and possess good properties, i.e., high hardness, wear and oxidation resistance at low and high temperatures, good surface quality, thermal stability, and low friction coefficient [65], [66]. The use of these HEAs improves the performance and the lifetime of the materials they coat. Their applicability could be extended to the microelectronics sector. [67]

Other HEAs show very good properties as irradiation-resistant materials, suitable for last generation fission reactors and future fusion reactors. After exposing these HEAs to radiation, grain coarsening and high defect concentration are minimized due to the lattice distortion effect and high phase stability against radiation. [68]–[70]

3.4.1 CrMnFeCoNi (Cantor) and $Al_{0.3}$CrFeCoNi HEAs

Cantor and $Al_{0.3}$CrFeCoNi can replace the alloys used nowadays by mining, construction, railroads, automobile and defence industries. These industries typically use high-strength steels (HSS), advanced high-strength steels (AHSS) or alloys able to activate one or several deformation mechanisms (e.g., TWIP: twinning-induced plasticity; TRIP: transformation induced plasticity; MBIP: microband induced plasticity). These materials have a good combination of strength and toughness, great energy-absorption capacity, good wear resistance and excellent work (strain)-hardening ability, addressing the demanding requirements of the mentioned industries.

In particular, TWIP steels are widely used by in these sectors as they can achieve the desired properties due to their low stacking fault energy, which increases considerably the amount of recrystallized and mechanical twins in the material. Mechanical twins can be generated through the continuous glide of Shockley partials on (1 1 1) parallel slip planes [71]. Mechanical twins act as dislocation motion/glide barrier that increases the density of dislocations in the twins and decreases the motion path of dislocations. Blocking the glide of dislocations allows the material accommodating larger plastic strains, enhancing ductility and work hardening ability. [10], [71]

Cantor HEAs have low stacking fault and twin-boundary energy low combined with high lattice-friction caused by the high-entropy and sever lattice distortion effects [3], [10]. Such combination hinders dislocation movement and eases forest dislocation hardening through the interaction of Shockley partial dislocations from intersecting crystallographic planes [10]. Moreover, Figure 3.7 shows that Cantor HEAs activate several deformation mechanisms based on the temperature and strain rate. At room temperature and low strain rates, dislocation slip is the dominant deformation mechanism; while at lower temperatures (even cryogenic range) or higher strain rates, mechanical twinning and nano-twinning gain importance until they become the dominant deformation mechanism. [72]

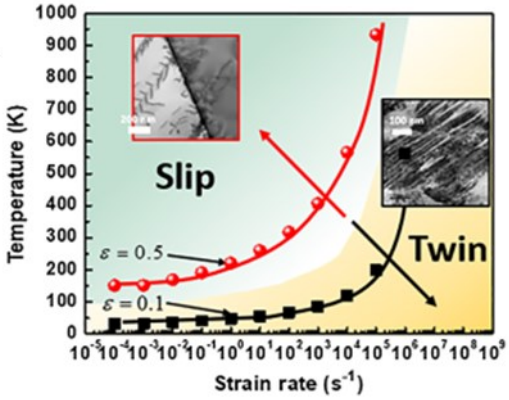

Figure 3.7 *Transition from slip to twinning regime for polycrystalline Cantor alloy at different strain levels. Twinning occurs at larger strain values when dislocation slip become difficult. [72]*

Alloying CrFeCoNi with Al instead of Mn (larger atomic radius) in $Al_{0.3}$CrFeCoNi leads to an increase in the lattice distortion effect and a decrease in the SFE and twin-boundary energy compared with the Cantor alloy [10], [73]. $Al_{0.3}$CrFeCoNi therefore develops mechanical twins under lower temperatures and higher strain rates than Cantor alloy [74], [75]. Z. Li et al. [74] proved this fact testing a hat-shaped specimen to high strain rate conditions; the material experienced twinning-induced continuous strain hardening. Figure 3.8 represents the deformation mechanism that $Al_{0.3}$CrFeCoNi alloy experienced during the experiment.

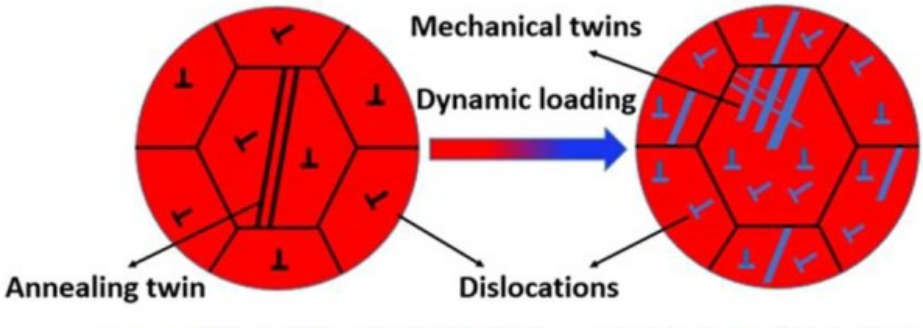

Figure 3.8 *Scheme of the deformation mechanisms $Al_{0.3}$CrFeCoNi experienced under dynamic loading. [74]*

Solid solution hardening combined with forest dislocation hardening and mechanical twinning give Cantor and $Al_{0.3}$CrFeCoNi alloys great plasticity and work-hardening ability [10], [74]–[77]. Figure 3.9 compares the work hardening capacity of different alloys. The subsequent increase in the strain-hardening rate of Cantor, $Al_{0.3}$CrFeCoNi HEAs and TWIP steels is due to twinning hardening activation.

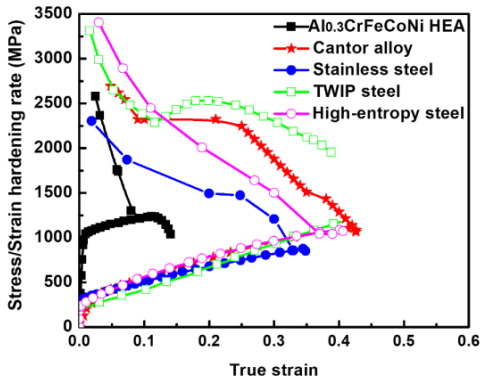

Figure 3.9 *Strain-hardening rate comparison as a function of true strain for different alloys. [10]*

Figure 3.10 shows the low thermal softening values of both Cantor and $Al_{0.3}$CrFeCoNi caused by the sluggish diffusion effect. This effect together with the severe lattice distortion in their lattices suppress shear localization and the formation of adiabatic shear bands until very high strain rates. Stacker [78] predicted that the critical shear strain for producing shear localization in $Al_{0.3}$CrFeCoNi is around 3.9, and approximately 7 for the Cantor alloy. The latter value is the only one experimentally tested [75]. In conclusion, despite these alloys show excellent strain hardening ability, low thermal softening and great resistance to shear localization, their dynamic properties have not been completely understood and explored. Hence, further investigation is required before they become the next generation of impact resistant structural materials.

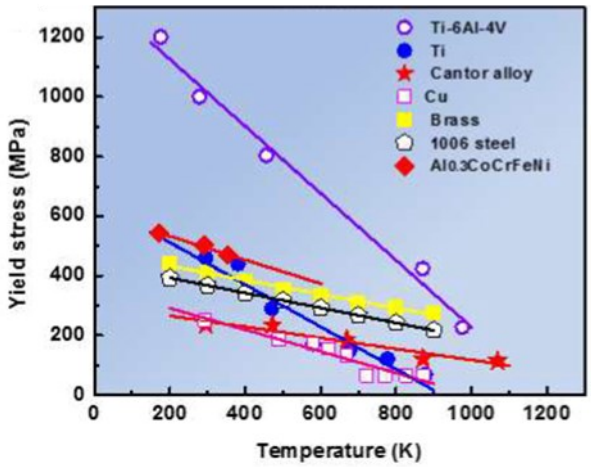

Figure 3.10 *Thermal softening effect of different materials. [75]*

4. SHEAR GEOMETRIES

Cylindrical specimens tested with Split Hopkinson tension (SHTB) and pressure (SHPB) set-ups under high-strain rate conditions can form ASB [79]–[82]. Siviour and Walley [88], [89], [83] improved the design of cylindrical specimens by reducing barrelling; however, cylindrical and dog-bone specimens cannot be used for the study of the formation of ASB as these geometries do not generate enough ASB while being deformed [81], [85]. For this reason, several researchers have designed and studied different specimen geometries that concentrate shear stresses in a specific region of the specimen while the rest remains elastic.

This chapter explains the basic design of several shear geometries, followed by the description of some variations of the basic design tested on different materials or with different equipment.

4.1 Rittel specimen

The so-called Rittel specimen consists of machining in a cylinder two opposed slots at 45° with respect to its longitudinal axis [86], [87].Those slots define the gage section, where shear deformation concentrates and the distribution of stresses and strains is constant. Figure 4.1 (a) shows the original design with rectangular slots and a clearance to improve the visual access to the gage section. These rectangular slots were replaced by semi-circular ones as they increase the values of plastic strain achieved in the tests, provide more reliable data and allow the Rittel specimens not to be restricted to shear (in compression) tests [88], [89]. Figure 4.1 (b-d) show the different variants of the Rittel specimen tested in both shear (in compression) and shear (in tension) conditions using the SHB set-ups [95]–[97]. Rittel specimen has been validated with FEM simulations, different materials (Al, Ti alloys, Cu, and steels) and in a wide spectrum of strain rates, ranging from quasi-static tests to dynamic.

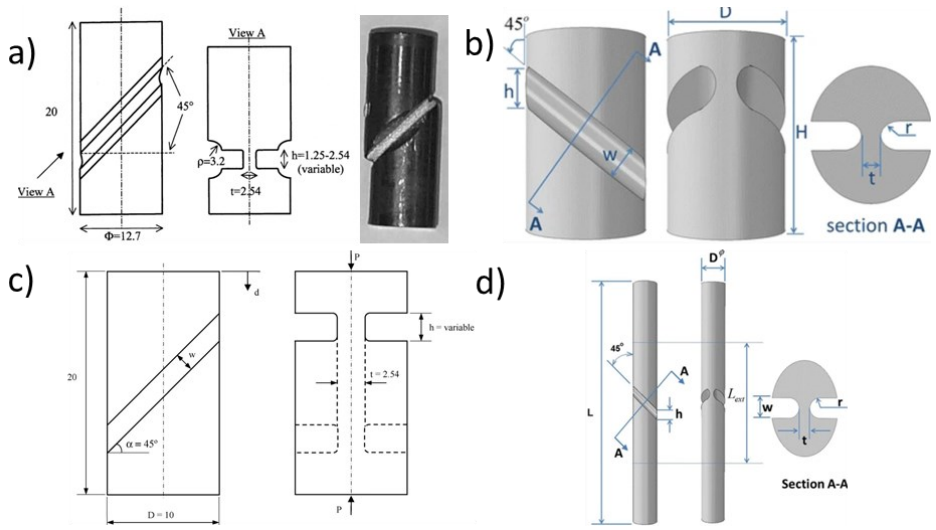

Figure 4.1 *Schematic representation of the Rittel specimen (a) original; (b) with semi-circular slots; (c) adapted to sheets [95], [96]; (d) for SHTB. [90]*

4.2 Punch and double notch specimens

Punch and double notch specimens are two shear geometries that require a hollow SHPB output bar [91]–[94]. The inner diameter of the output bar needs to be larger than the diameter of the input bar so the specimen can be subjected to shear deformation.

There are two types of punch specimens, with and without notch. The concentration of stresses at the gage section is easier for the notched punch specimen. Tests with this geometry are easy to assemble and perform, but the determination of the shear area is based on the nominal clearance, as it cannot be measured accurately [95]. The clearance together with the specimen geometry, radii and stress concentration affect strongly the results [96]. Figure 4.2 (a) shows a punch specimen with a notch.

Double notch specimens consist of a rectangular bar with a pair of notches near the ends as shown in Figure 4.2 (b). This geometry allows the direct observation of the temperature and deformation evolution. However, the stress distribution is not uniform and pure shear stresses are not assured at large deformation values [93], [97]. The results obtained with this geometry tend to be unreliable unless very specific testing conditions are met. Therefore, the use of this geometry is scarce.

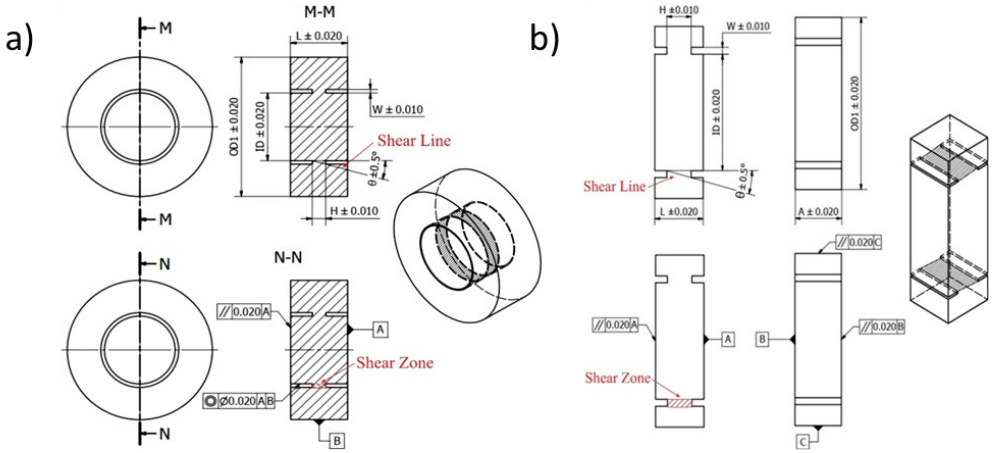

Figure 4.2 *Schematic representation of: (a) punch specimen; (b) double notch specimen. [98]*

4.3 S-shaped specimen

Compact-force-simple-shear specimens or S-shaped specimen geometries align shear plane parallel to the loading direction [99], [100]. This design allows studying large shear strains, damage and failure mechanisms evolution on materials with microstructural or crystallographic anisotropy. The S-shaped specimen provides accurate stress-strain curves thanks to its manufacturing simplicity and its capacity for reaching force equilibrium and providing a homogeneous stress field in the shear region [101]. A. Arab et al. [100] validated the geometry by experimentally testing the specimen on a Ti6Al4V alloy coupled with 2D Digital Image Correlation (DIC) method and FEM simulations [107]. Figure 4.3 shows a scheme of the design.

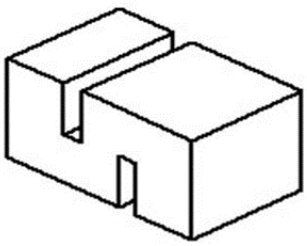

Figure 4.3 *Schematic representation of the S-shaped specimen.*

Researchers developed similar geometries to the S-shaped specimen and tested them on different materials (steels) and loading conditions, i.e., Shear (in tension) tests on SHTB [102]. Changing the dimensions of the gage section can lead to a purer shear stress state in the gage section [101]. Figure 4.4 shows these different designs, some of them more complex than the original one, but valid for the testing.

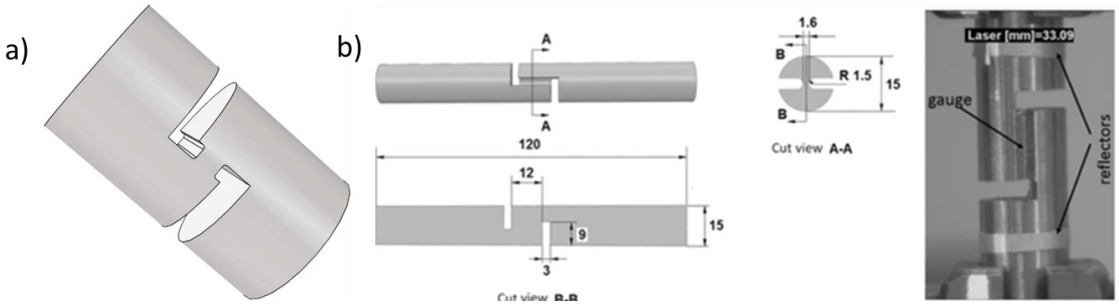

Figure 4.4 *Variants of the S-shaped geometry: (a) suitable for SHPB* [101]*; (b) suitable for SHTB.* [102]

The American Society for Testing and Materials (ASTM) published a design suitable for the characterization of thin specimens under shear conditions resulting in the ASTM B831 specimen design from Figure 4.5 a). Isakov et al. [103] modified such design, milling the thickness of the gage section a 50% [110]. The reason is that in the original model deformation field is complex, non-uniform and spreads out the gage section. Meanwhile, Isakov's design [103] ensures the localization of plastic deformation and final fracture within the gage section. The design keeps ideal shear deformation conditions up to relatively high deformations, but the final fracture undergoes a complex multiaxial loading derived from the simple shear loading. Figure 4.5 b) shows Isakov's design [103] tested on an AISI 444 steel. The experiments were coupled with 3D-DIC set-up.

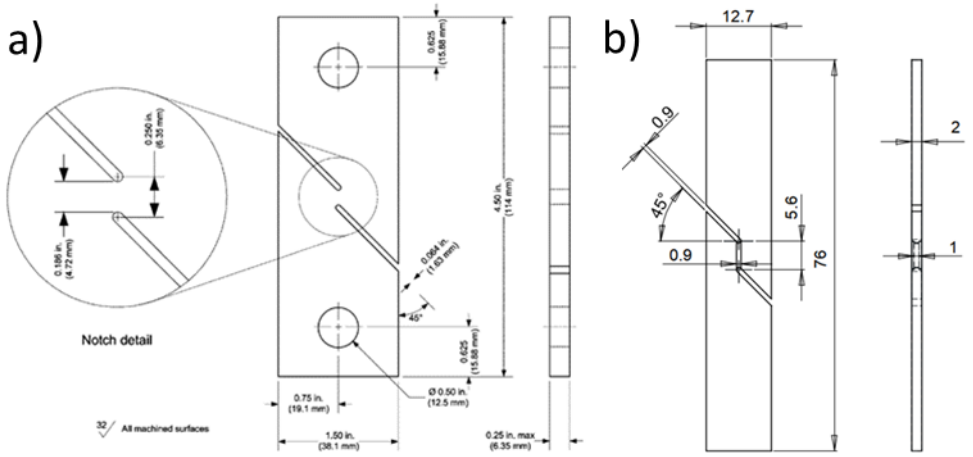

Figure 4.5 *Schematic representation of: (a) ASTM B831 specimen geometry for thin metallic sheets [104]; (b) localized strain geometry design [103].*

Figure 4.6 shows the next improvement on the design performed by the same team [104]. The 45° cut-outs in the designs from Figure 4.5 were replaced by 90° cut-outs, resembling S-shaped geometries. This modification enabled reaching force equilibrium faster and obtaining satisfactory data in high-strain rate tests. The design was tested on 2024-T351 Aluminum plate and under quasi-static (0.01 s^{-1}) and dynamic (up to 2000 s^{-1}) conditions.

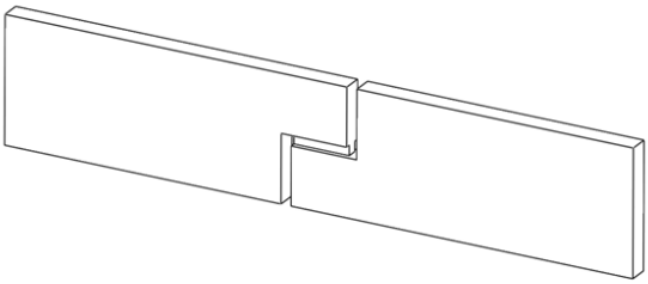

Figure 4.6 *Schematic representation of the 90° cut S-shaped specimen geometry for the testing of thin metallic sheets. [104]*

4.4 Hat specimen

Meyer and Manwaring [105] designed the hat specimen to study the influence of temperature, original microstructure, and strain rate on the generation and evolution of ASB. The design (Figure 4.7) consists of an axisymmetric specimen with an upper hat and a lower brim that concentrates shear strains in the region in between when the specimen is compressed. Specimens are easy to manufacture and, by controlling the size of the shear area and using stopping rings, the comparison of the behaviour of the component at both low and large strains and strain rates is possible [106]. However, as main drawbacks, the width of the shear region and the radius of the corners affects the stress-strain curves and strain concentration; additionally, force equilibrium is difficult to fulfil [96]. The design has been tested on multiple strain rates and materials [107]–[114]; and it is the only known geometry used for the study of ASB formation in Cantor HEAs. [115]

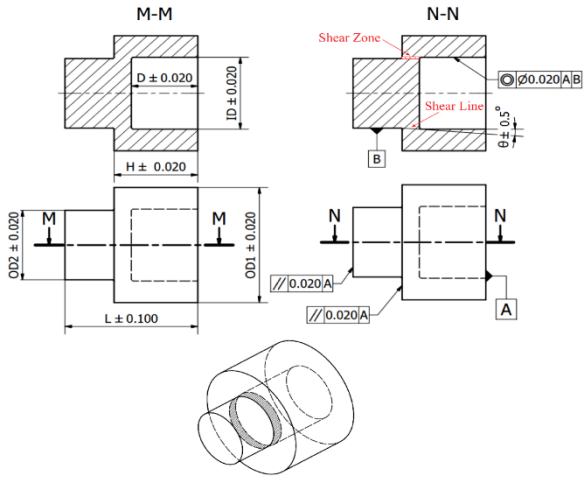

Figure 4.7 *Schematic representation of the hat specimen. [98]*

A variation of the hat specimens are the hat-like-shaped specimens or “plate shear” specimens and the flat-hat specimens [116]–[119], [105-108], used for examining how

strain rate affects shear localization. Plate shear specimens (Figure 4.8-a) were designed by Meyers [116], [117] and require of a holder to constrain the movement in the axis perpendicular to the compression. The design has been tested in many materials (including bulk metallic glasses) and verified throughout extensive Finite Element Analysis [116], [117]. Figure 4.8 b) shows the flat-hat specimen developed by Clos et al. [118], [119] to reduce the edge effect present in the hat specimens. The design does not require of a holder as the brims are connected by a base below the shear region. The direct visualization of the gage section allows coupling the specimens during their testing with imaging tools such as DIC or Infrared Thermography.

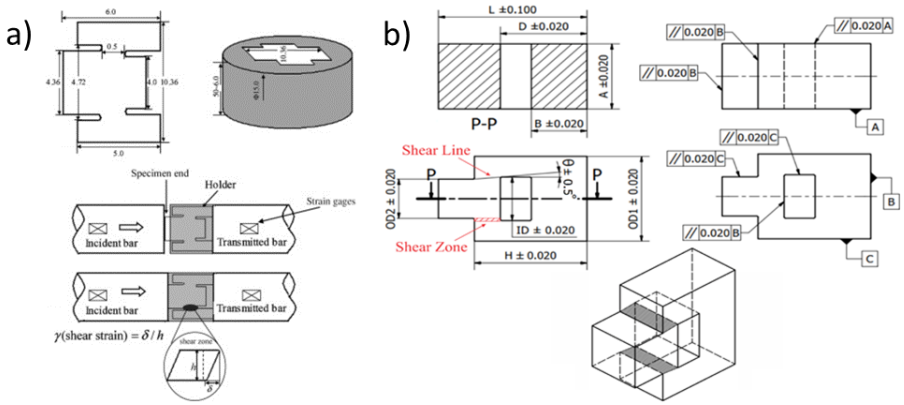

Figure 4.8 *Schematic representation of: (a) plate-shear specimen geometry* [115]*; (b) flat hat specimen geometry.* [98]

5. FINITE ELEMENT METHODS

Finite Element Analysis (FEA) has grown so much in the last decades with the aim of contributing to the improvement of materials science and engineering prototyping, design, testing and analysis. FEA is a numerical method used for designing components and predicting accurately their response to multiple physical effects. To solve and analyse the model, the component is divided into small parts called elements. The whole set of elements is called mesh and keeping an adequate element size is important to ensure correct computer calculations and minimize computational cost. [120]. Finite element calculations use either implicit techniques or explicit techniques; in some cases, both techniques are combined for achieving a more accurate solution. In any case, consider the following finite element equation as the one governing,

$$\boldsymbol{M\ddot{u} + C\dot{u} + Ku = F^{ext}} \qquad \textbf{18}$$

where u, $\dot{u}$ and $\ddot{u}$ are the displacement, velocity and acceleration nodal vectors respectively. M, C and K are the mass, damping and stiffness matrixes respectively [121], and with the nodes from Figure 5.1 as the calculation points for solving the equation with any of the mentioned techniques.

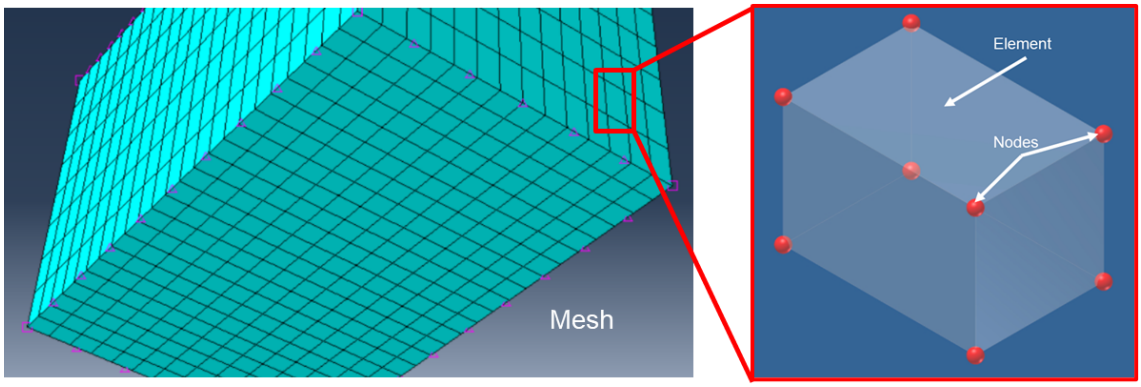

Figure 5.1 *Representation of the mesh, elements and nodes.*

Matrix M is a diagonal, also called “lumped”, matrix. K stiffness matrix defines the physical behaviour of its element and, when assembled with the rest of elemental stiffness matrixes, it forms a global stiffness matrix similar to the simplified below for a 2-element case.

$$\textit{Element 1 } \boldsymbol{K_1} = \begin{bmatrix} \boldsymbol{k_{11}^1} & \boldsymbol{k_{12}^1} \\ \boldsymbol{k_{21}^1} & \boldsymbol{k_{22}^1} \end{bmatrix}; \qquad \textit{Element 2 } \boldsymbol{K_2} = \begin{bmatrix} \boldsymbol{k_{11}^2} & \boldsymbol{k_{12}^2} \\ \boldsymbol{k_{21}^2} & \boldsymbol{k_{22}^2} \end{bmatrix}$$

Global 2-element matrix $$K_G = \begin{bmatrix} k_{11}^1 & k_{12}^1 & 0 \\ k_{21}^1 & k_{22}^1 + k_{11}^2 & k_{12}^2 \\ 0 & k_{21}^2 & k_{22}^2 \end{bmatrix} \quad 19$$

For the implicit model the equation to be solved is

$$u = K^{-1}(F^{ext} - M\ddot{u} - C\dot{u}) \quad 20$$

This technique needs to reach global equilibrium to solve the problem [120], which requires creating the inverse K matrix for thousands of elements that form the model; such operation is computationally intensive (costly) [127]. A function is implicit when it is not able to discriminate the variables in it, just like in the case of

$$x^y = e^{xy} + x \quad 21$$

The best approach for solving Equation 21 is through a lengthy iterative process until reaching equilibrium. Hence, the general governing finite element equation for the implicit technique is

$$\{u\}_{n+1} = f(\{\dot{u}\}_{n+1}, \{\ddot{u}\}_{n+1}, \{u\}_n, \{\dot{u}\}_n, \{\ddot{u}\}_n, \dots) \quad 22$$

To solve the equation and find out the unknown values, the model uses the current and later values. Newton-Raphson is one of the iterative methods used for evaluating the local variables until achieving convergence and reaching global equilibrium [127]. For these reasons it is said that implicit techniques are unconditionally stable. Implicit techniques provide accurate results and allows using very large time increments. Implicit solution techniques are suitable for the analysis of static (matrices M and C can be neglected), low-speed dynamic (e.g., low frequency response, vibration, or oscillation) or steady-state transport cases, like mass diffusion and heat transfer. [121], [122]

The explicit model solves the following equation

$$\ddot{u} = M^{-1}(F^{ext} - Ku - C\dot{u}) \quad 23$$

It is said that a function is explicit when is possible to discriminate the variables in it, the following example illustrates it

$$x = e^{xy};\ ln\, x = xy\ ; y = \frac{x}{ln\, x} \quad 24$$

A general governing equation for the explicit model can be defined as

$$\{u\}_{n+1} = f(\{u\}_n, \{\dot{u}\}_n, \{\ddot{u}\}_n, \{u\}_{n-1}, \{\dot{u}\}_{n-1}, \{\ddot{u}\}_{n-1}, \dots) \quad 25$$

The explicit techniques directly evaluate the local variables at later time knowing the previous values only, reaching a direct solution. Global equilibrium calculations are not needed for each increment, but keeping numerical stability is important; indeed, it is said that explicit techniques are conditionally stable [127], [128]. Making small increments

(time step) for their calculations is important for this technique to avoid unstable solutions or significant error. This suggests that the number of increments to be analysed is extremely large, but computationally inexpensive. The reasons are that calculating the inverse of the diagonal mass matrix M is simple. Using small increments do not require of iterations for reaching the direct solution and does not need to form the tangent (stiffness K) matrix. Small increments also simplify the treatment of contacts. The stability limit for time step is defined as follows

$$\Delta t = \frac{L_{min}}{c} \qquad 26$$

where L_{min} is the characteristic length of the smallest element dimension in the model (mesh) and c is the current dilatational wave speed, whose simplest form is

$$c = \sqrt{\frac{E}{\rho}} \qquad 27$$

where E is the Young's modulus and ρ is the density of the material [130]. Explicit solution techniques are suitable for solving simultaneous large displacement and contact problems, wave propagation (car crash, tool test, impact, blast…) studies or "event and response" applications where the total dynamic response time is only a few orders of magnitude larger than the stability limit. [121], [122]

5.1 Abaqus

Abaqus is the FEM tool used in this thesis, and consists of three stages, pre-processing, simulation and postprocessing [129]. Abaqus CAE is used in the pre-processing stage for graphically define the model of the physical problem and the Abaqus input file; other pre-processors could be used. The model includes the geometry of the component, material data, element section properties, loads and/or boundary conditions of the problem, analysis type (implicit, explicit and their derivatives) and output request for a proper results interpretation [122]. In the simulation stage, the software solves the numerical problem defined in the input file. The magnitude and complexity of the input file and power of the computer determines how long the computer takes to create an output file with the solution of such problem and ready for postprocessing. Abaqus viewer is a tool with which the user can evaluate the results in an interactive way; other postprocessors could be used.

5.1.1 Software assumptions

All deformable elements of the model are based on the Lagrangian or material description behaviour [121], [122], which means that the material associated with an element remains associated to it throughout the analysis, not being able to flow across the boundaries as in the Eulerian, or spatial, description elements.

Independently of the material behaviour in a physical experiment, if the inputted data of the material is in terms of true stress-strain, Abaqus considers such data as suitable for both tension and compression simulations. [129]

Contact is considered a discontinuous constrain that is only applied when the two selected surfaces are in contact, i.e., when the contact clearance or distance between contacting surfaces is smaller or equal to 0 [121]. The existing forces across the interface of the contacting surfaces are normal forces, and shear forces if friction is considered. Abaqus implements Coulomb's friction model (most common), using a friction coefficient μ to describe interaction between the surfaces in contact. From a critical value of shear stress on, tangential motion occurs and the contacting surfaces slip [121]. The critical shear stress value depends on the contact pressure and the friction coefficient as described in

$$\tau_{crit} = \mu \cdot p \qquad 28$$

Large values of the friction coefficient in Abaqus explicit usually do not lead to any calculation problems. While for Abaqus standard (implicit), values equal or larger than 0.2 add an extra unsymmetric term that the solver needs to consider for a good results convergence, doubling the computational costs of the simulation. [121]

There are two possible contact approaches, pure master-slave and balanced master slave. The latter approach applies pure master-slave twice, reversing the surfaces on the second pass. Pure master-slave approach means that contact constrains are only applied when slave nodes try to penetrate master facets, while penetrations of mater nodes into slave facets can go undetected [120]. For this reason, slave surface should be the one more finely meshed, or associated to the softer material if the mesh densities are similar.

Besides the contact approach, defining the constrain enforcement method chosen (penalty or kinematic) is important. The kinematic constrain enforcement method uses a corrector contact algorithm to strictly enforce contact constrains (e.g., not allowing penetrations). The penalty contact method applies equal and opposite contact forces to both master and slave nodes at the penetration point; such forces result from the multiplication of the stiffness penalty matrix times the penetration distance. Penalty-

contact constrain is weaker than kinematic contact constrain but allows treating a higher number of contact types. [121]

Regarding element mesh, two of the most common elements meshes used in stress-strain analyses can be differentiated based on the number of integration points an element has and how data is interpolated inside them. The integration points of an element are at their nodes, inside the element or at their edges; they act as calculation points for the multiple degrees of freedom (DOF) a deformable body has in finite element calculations [127], [131]. Meshes can contain first (linear) or second (quadratic) order elements with reduced or full integration. [131]

First order, reduced integration mesh is the most suitable for problems involving large distortions, contact problems, large strains or when high strain gradients are expected [120], [124]. This mesh can be used by both Abaqus implicit and explicit solvers [124], the computational time is low and prevents volumetric and shear-locking, common issue in linear, full integration elements or quadratic, reduced integration ones. Numerical formulation of the recently mentioned element meshes makes them stiffer by rising shear strains that do not exist [124]. However, linear, reduced integration elements can experience hour glassing (Figure 5.2- b). This issue is an uncontrolled distortion of the mesh due to the large flexibility of its elements. [124]

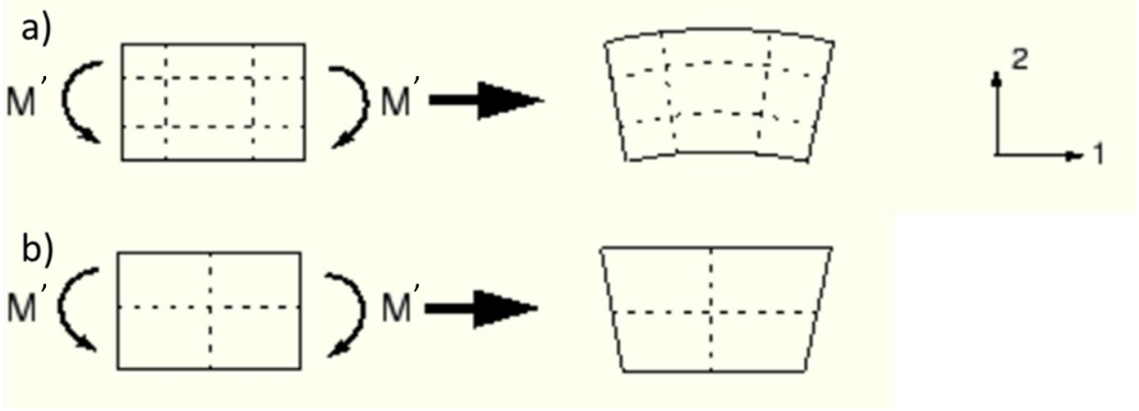

Figure 5.2 (a) *Deformation of material subjected to bending moment M'; (b) Deformation of a linear, reduced integration element subjected to bending moment M'.* [120]

Finely meshed components with a small amount of "hourglass stiffness" (hourglass control) limit the propagation of hourglass mode, preventing this issue [120], [124]. Quadratic, full integration elements could be another alternative to these problems, but the computational cost is very high. Finally, Tetrahedral elements are too stiff for stress analysis problems, so hexahedral elements are used instead [124].

6. EXPERIMENTAL METHODS FOR CHARACTERIZATION OF HIGH STRAIN RATE SHEAR RESPONSE

This chapter explains the basic concepts of the equipment that can be used during the experimental testing of the specimens (Torsion Split Hopkinson Bar system is not used in this thesis) for gathering materials response under dynamic loading. It includes a formula guide to calculate the shear stress – shear strain response of the component based of the signals gathered by the Split Hopkinson Bar set-up. The chapter ends with the explanation of the working principles of Digital Image Correlation tool.

6.1 Split Hopkinson Bar

John Hopkinson and his son Bentram Hopkinson invented the Split Hopkinson Bars (SHB), the set-up was further improved by Davies and Kolsky, so they are also known as Kolsky bars [125]. This dynamic testing method can subject the specimens to strain rates [125] between 10^2 and 10^4 s^{-1} [126]. Both brittle and ductile materials can be tested with the following SHB set-ups: compression, tension, and torsion split Hopkinson bars.

6.1.1 Split Hopkinson Pressure Bar (SHPB)

Figure 6.1 shows a scheme of the SHB set-up most used out of the mentioned ones [127]. The SHB consists of three bars: incident (or input) bar, transmitter (or output) bar and striker (or projectile) bar; the composition of the bars (aluminum, titanium, polymers, stainless steel, maraging steel, high strength structural steel or Inconel nickel alloy) and dimensions (length/diameter = 20) ensure the propagation of uniaxial stress according to the one-dimensional elastic wave theory [126]. Lubrication at the surfaces of the input and output bars that are in contact with the specimen is important to avoid the effects of friction.

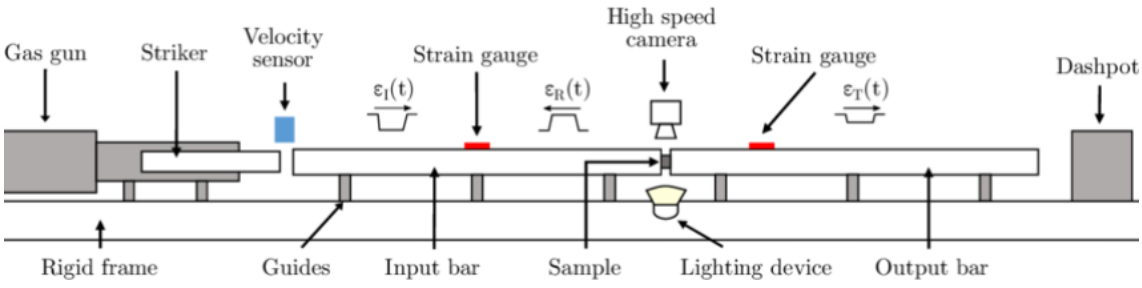

Figure 6.1 *Schematic picture of the SHPB. [127]*

The SHPB operates according to this sequence: a gas gun launches the projectile towards the free end of the incident bar, generating at the impacted region an elastic incident pulse (its length is large compared with the dimensions of the specimen) that travels throughout the bar. The specimen, placed between the input and output bars, is sandwiched and, subsequently, the impact generates two new pulses from the incident one, a reflected pulse that travels back through the incident bar and a transmitted pulse that travels through the output bar [126]. The strain gages measure the amplitudes of the incident, transmitted and reflected pulses, ε_i, ε_r and ε_t respectively; a buffer placed after the output bar absorbs the remaining energy. Placing the strain gages at the middle of the input and output bars and using a projectile whose length is 40 to 45 % input or output's bar length is important to avoid overlapping in the gathered data [133], [134]. The difference of impedance Z between the bars and the specimen makes the incident and transmitted pulses differ from each other and generates the reflected pulses. Impedance Z is expressed as follows,

$$\boldsymbol{Z = \rho \cdot A \cdot c} \quad \textbf{29}$$

where ρ is the density, A is the cross-sectional area and c is the speed of the wave in the material. Wave propagation in the specimen is not considered, but keep in mind that reverberations are produced when the incident pulse initially enters the specimen, and it takes around three reverberations to reach equilibrium in the specimen [126], [127]. Figure 6.2 illustrates an example of the measured pulses' strain amplitude with respect the time.

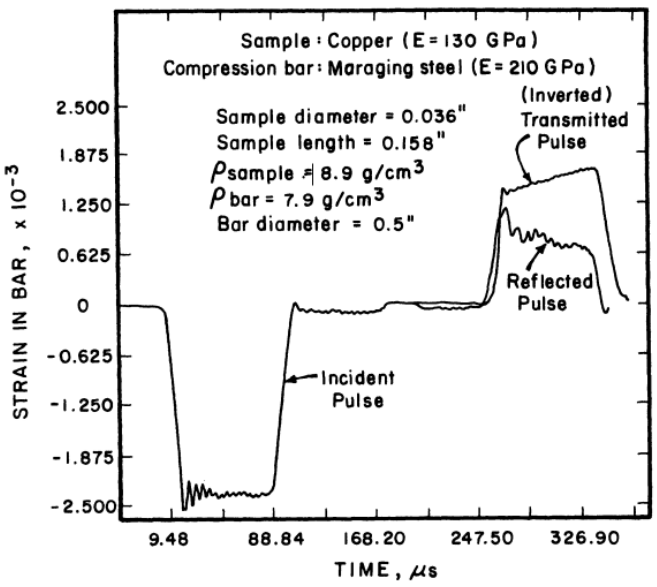

Figure 6.2 *Example of the signals collected during a SHB test.* [126]

From the three recorded pulses it is possible to obtain the stress-strain response of the specimen. DIC (Digital Image Correlation) is a tool of great use for the comparison of the calculated strains through the Full Field Data analysis of a video recording of a specimen with a dotted pattern.

6.1.2 Split Hopkinson Tensile Bar (SHTB)

Figure 6.3 illustrates the SHTB set-up which differs with the SHPB set-up in the generation of the incident pulse, the geometry or the specimen and its placement between the input and output bars. Nevertheless, the testing principles and the methodology for data collection are similar between the two set-ups

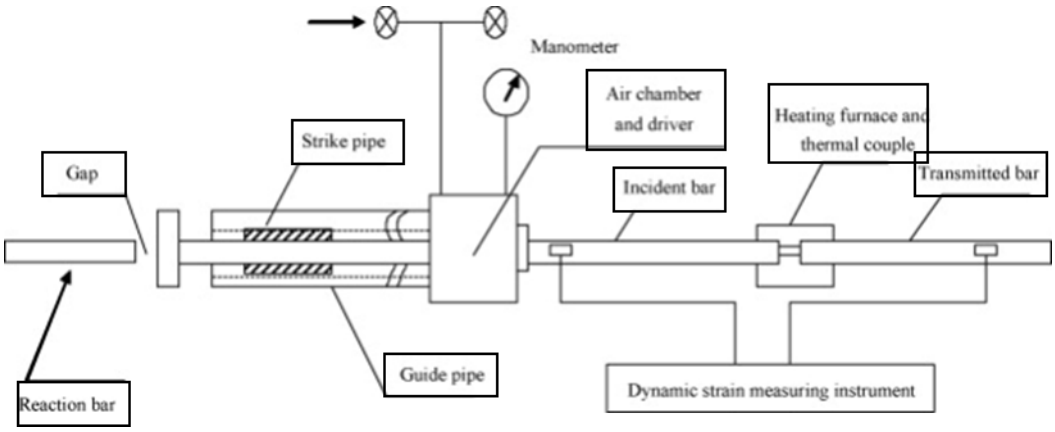

Figure 6.3 *Schematic representation of the SHTB.*

Around the loading bar (input bar with an impact flange) sits a striker tube, which generates the incident (tensile stress) pulse when launched against the impact flange using compressed air. Adjustments in the gas pressure determine the amplitude of the mentioned pulse. Nemat-Nasser at al. [128] proposed adding a wave-trapping method to be able to analyse specimens that did not break.

The specimen can be mounted in the system in different ways. The specimen can be bolted, glued, screwed directly to the bars; or it could be glued to grips and then screw the grips to the bars.

Moreover, the SHPB set-up can adopt other tensile testing methods. Figure 6.4 a) shows a hat-shaped specimen placed between a solid incident bar and a hollow output bar; the gage section of the specimen experiences tensile strain when it is sandwiched. In Figure 6.4 b) a collar isolates the specimen from the compression wave and return it as a tension wave to the specimen. Finally, in the inertial set-up from Figure 6.4 c), the striker hits the main tube creating a compression wave that pulls the specimen while the inertial bar

counteracts the movement of the main structure, generating a tension pulse in the specimen.

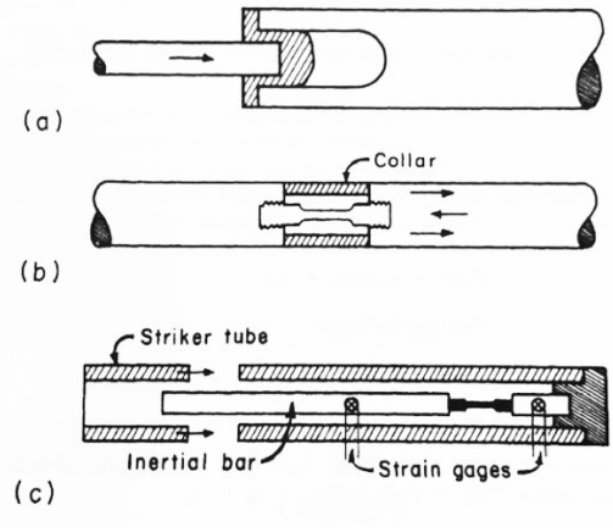

Figure 6.4 *Schematic picture of alternative SHTB set-ups.* [126]

6.1.3 Torsion Split Hopkinson Bar (TSHB)

Figure 6.5 represents the TSHB, firstly introduced by Baker and Yew in 1966 [129]. With a rotatory actuator placed at the end of the input bar and a clamp that retains it until the experiment begins, the TSHB system applies a dynamic torsional load on the specimen when suddenly releasing the actuator. As in the previous techniques, the behaviour of the bars should remain in the elastic regime during the test.

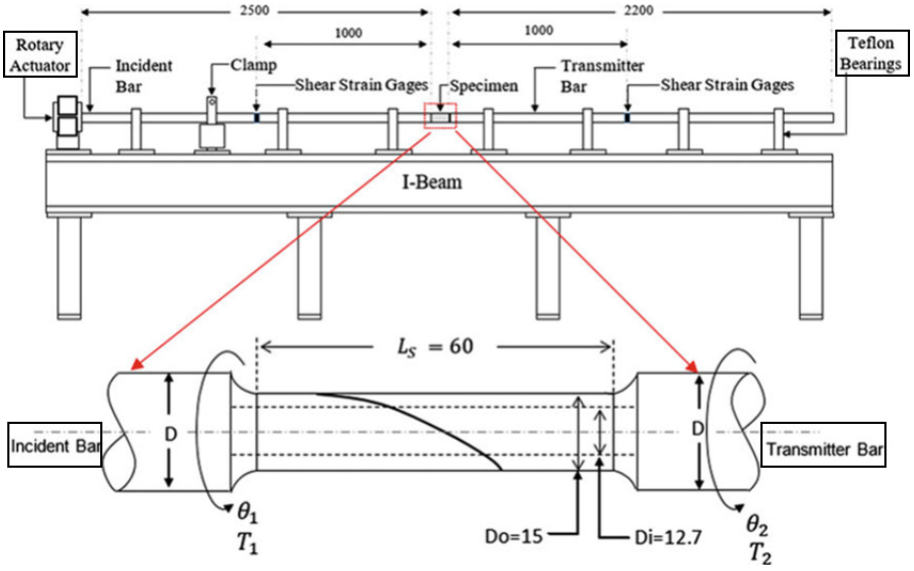

Figure 6.5 *Schematic representation of a TSHB with a spiral notch specimen mounted into place.*

There are other loading methods such as direct, flywheel, explosive and electromagnetic [130]–[133]. Beginning with the direct impact loading, an impact pin attached to the end of the incident bat generates the torsional load [132]. The flywheel loading consists of a flywheel accelerated to the desired speed using a motor, following by detaching the flywheel from the motor and attaching it to the input bar while the flywheel is still rotating [130]. The explosive loading consists of detonating simultaneously two little charges placed on each end of the incident bar [133]. And in the electromagnetic loading, the incident bar rotates when applying a strong magnetic field on it. [131]

Despite being the TSHB a very effective technique for the generation of a shear stress-shear strain response in the material, Meyer and Manwaring [105] introduced the hat specimen to generate the same mechanical response using the SHPB. That geometry was the starting point for numerous researchers to study the compatibility of certain geometries to generate a shear response with the SHPB.

6.2 Shear stress-strain calculation

The strain gages detect and measure the incident ε_i, reflected ε_r and transmitted ε_t pulses. The displacement and forces at the interface of the bars can be calculated by applying the one-dimensional elastic wave theory as follows,

$$F_{input} = A_{bar}E_1(\varepsilon_i(t) + \varepsilon_r(t)) \quad 30$$

$$F_{output} = A_{bar}E_2\varepsilon_t(t) \quad 31$$

$$U_{input} = -C_1 \int_0^t \left(\varepsilon_i(t) - \varepsilon_r(t)\right) dt \quad 32$$

$$U_{output} = -C_2 \int_0^t \varepsilon_t(t)dt \quad 33$$

$$V_{input} = -C_1(\varepsilon_i(t) - \varepsilon_r(t)) \quad 34$$

$$V_{output} = -C_2(\varepsilon_t(t)) \quad 35$$

where F represents the force, U the displacement, “input” and “output” refer to the incident and transmitted bars respectively; A_{bar} is the cross-sectional area of each bar; E is the Young’s modulus and C is the wave speed in each bar, from Equation 27.

Force equilibrium is assumed and the properties of the bars are homogeneous, isotropic and elastic during the test. Therefore, F_{output} was used in the calculation of the stress-strain response of the tested specimens. Applying this assumption to the study, the shear stress, shear strain and shear strain rate (Equations 2 and 3) would be as follows

$$\tau = \frac{F_{output}}{A_{gs}} \qquad 36$$

$$\gamma = \frac{U_{input} - U_{output}}{L_s} \qquad 37$$

$$\dot{\gamma} = \frac{V_{input} - V_{output}}{L_s} \qquad 38$$

where A_{gs} and L_s are the cross-sectional area and width of the shear zones respectively. As needs to be adjusted if two rectangular gage sections are considered instead of one (i.e., flat-hat, punch, or double notch specimens), if Rittel specimen is used, or if the gage section is cylindrical, like the hat specimen.

6.3 Digital Image Correlation (DIC)

DIC is a non-interferometric, optical technique introduced in the 1980s that analyses the images taken from the surface of the component before, during and after the experiment, and correlates those images with the deformation experienced by such component. The accuracy of DIC is high, and the quality enhancement of the cameras and new algorithms led to big improvements of this technique since its conception. DIC is not restricted to optical images; indeed, the system can be coupled with infrared (IR) cameras [134], Electron Backscattered Diffraction (EBSD) [135], [136], X-Rays [137]–[139] or SEM microscopes [136].

Setting-up the DIC system does not require of low-vibration environments, meticulous surface preparation nor special lightning conditions; and it is suitable for outdoor measurements, reducing the costs of inspection [136]. A camera (2D, Figure 6.6-a) or group of cameras (3D, Figure 6.6-b) capture images of the surface of the specimen; but before, placing them in the right position is important, so calibration plates similar to the one shown in Figure 6.6 c) are necessary. [140], [141]

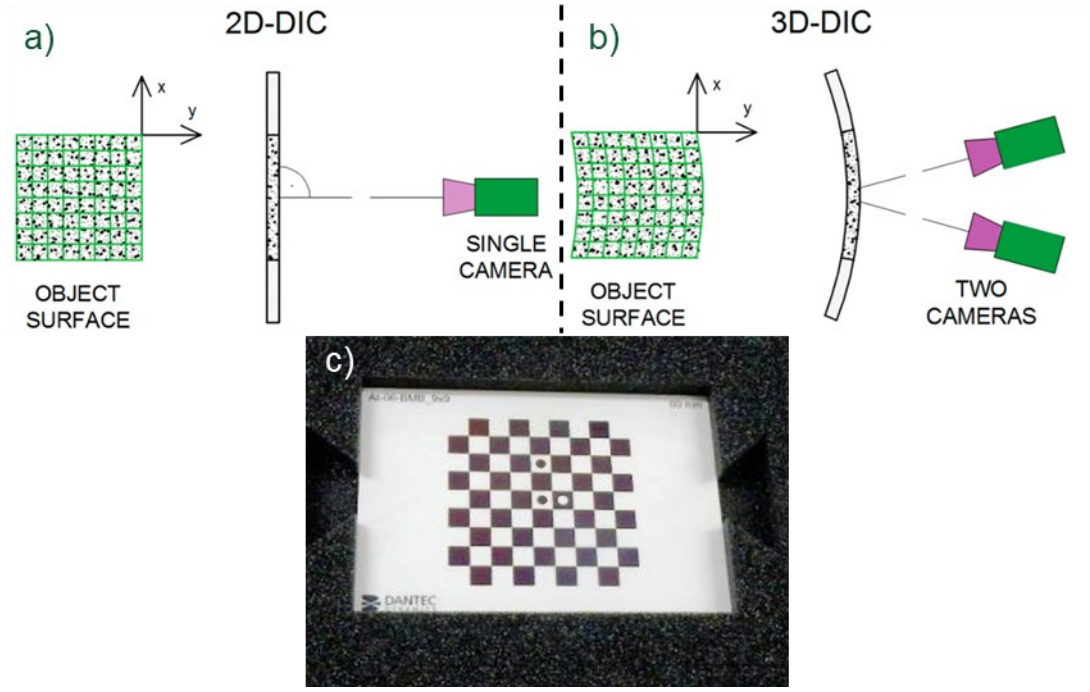

Figure 6.6 *(a-b) Scheme of the possible DIC system set-ups; c) example of calibration target.* [142]

Also, the software needs to register the position of every region or subset facet of the specimen so the software can track them during the test. Therefore, a recognizable pattern over the surface of interest before taking any image is necessary. Such pattern can be either the natural texture of the specimen or painted speckles on its surface as Figure 6.7 shows.

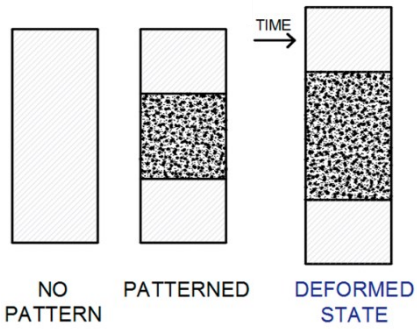

Figure 6.7 *Example of surface preparation for DIC measurements via sprayed/painted speckles before and after deformation.* [142]

Figure 6.8 shows an image of the specimen prior to the test that works as “reference image” for the software to set a grid of points. Every squared subdivision of the grid is a facet, which acts as calculation area. [141], [143]

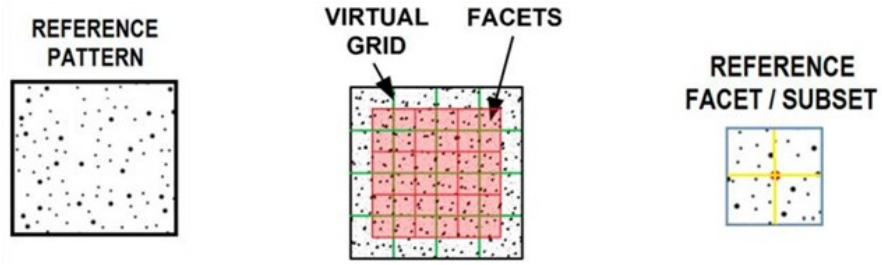

Figure 6.8 *Scheme of the virtual grid and facets generated by the DIC software.* [142]

To make accurate enough calculations, each of the black and white “dots” in the facet needs to be, ideally, between 3 and 5 pixels each. Dots larger than 5 pixels imply using larger subsets, decreasing spatial resolution; while features smaller than 3 pixels produce aliasing. Aliasing adds errors to the results because the features cannot be converted into digital image. Aliasing can be solved by doing a more suitable pattern, defocusing the image or changing the optics of the camera. [142], [143]

After deformation, a matching mathematical function tracks the facets and a subset shape function correlates the facets before and after deformation, as showed in Figure 6.9. In this correlation, the function decomposes the deformation of the subsets into a combination of deformation processes (e.g., uniform deformation, translation, non-linear deformation) easier to represent mathematically. Finally, an interpolant sets a step size for the calculations based on the dimensions of the sample and grid. [143]

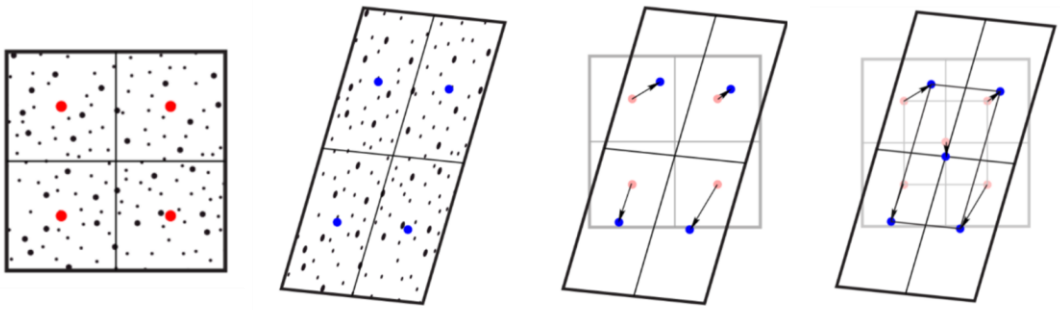

Figure 6.9 *Graphical representation of a possible facet tracking from their original state to their deformed state.* [144]

For the calculation of displacement and strains, DIC software “places” along the specimen lots of extensometers (Virtual Strain Gage or VSG). Small VSG increases spatial resolution; while large VSG reduces the noise in the gathered data. Noise sets the minimum resolution of the equipment. Other applications of large VSG are smoothening the strain field gradient and giving the position of the maxima; however, it does not provide its value. [141]

Displacements or deformation maps of the surface of the specimen are generated. The amount of displacement vectors is so big that it is considered as continuum data, also known as Full Field Data. Stress-strain maps can be developed complementing the displacement/strain maps with the gathered data from the testing devices.

DIC is a non-contact technique, independent from the material of the specimen or its length, and used for many different applications. DIC can be used in characterization of deformation of solids, and crack generation and propagation examination, even if the edges of the cracks are not properly defined [140], [145]. More uses are damage development detection in composites [138], quasi-static and dynamic analyses [85], [146]–[150], strain mapping at high temperature and study of structural deflections. Mining, medicine [145], conservation of natural heritage [151] are other possible uses for the DIC out of the field of engineering. In this study, DIC compares the stress-strain curve obtained by means of testing devices and the Finite Element tools.

7. METHODS

This chapter specifies which equipment was used for this thesis, and the available materials and information from previous studies on the Cantor and $Al_{0.3}CrFeCoNi$ HEAs. Some shear geometries were selected for their testing in the laboratory; then, it is described a first approach to the explicit and implicit models. Those models are explained in more detail followed by a brief introduction on the modifications performed to the designs to improve shear localization at the gage section. The chapter continues explaining how the specimens were manufactured for their testing, the testing conditions and how to obtain the stress-strain curves. The chapter concludes with an explanation of the DIC methodology.

7.1 Materials and equipment

The following true stress – true strain tables are from Soares et al. [4] investigation on the material response of Cantor cylinders tested under compression at different strain rates. This data is used in First simulation approach.

***Table 1**. Cantor alloy data under dynamic conditions (strain rate: 2800s^{-1}).* [4]

True stress (MPa)	Plastic strain
600	0
680	0.03
730	0.05
840	0.10
1000	0.2
1100	0.30
1200	0.39
1220	0.4

***Table 2** Cantor alloy data under quasi-static conditions (strain rate: 10^{-1} s^{-1}).* [4]

True stress (MPa)	Plastic strain
540	0
670	0.05
760	0.10
890	0.2
980	0.3
1040	0.4
1090	0.5
1110	0.55

Table 3 *Cantor alloy data under quasi-static conditions (strain rate: $3*10^{-4}$ s^{-1}).* [4]

True stress (MPa)	Plastic strain
480	0
620	0.05
700	0.1
820	0.2
910	0.3
980	0.40
1060	0.50
1090	0.54

And the general properties of the Cantor HEA valuable for this thesis are

Table 4 *Cantor alloy properties.*

Density (kg/m^3) [4]	7.958
Young's modulus E (GPa) [152]	202
Shear modulus G (GPa) [152]	80
Poisson's ratio v (dimensionless)	0.26

where Poisson's ratio is calculated considering the material as homogeneous and isotropic using the following equation,

$$E = \frac{2G}{(1+\nu)} \qquad 39$$

However, to use the data from Table 1 in the shear specimens, the true stress was considered as maximum effective stress, and converted into plastic shear stress using the von Mises criterion,

$$\sigma_{eff} = \sqrt{3}\,\tau_{pl} \qquad 40$$

$$\varepsilon_{eff} = \frac{1}{\sqrt{3}}\gamma_{pl} \qquad 41$$

where τ_{pl} and γ_{pl} are the shear stress (τ) and strain (γ) from Equations 36 and 37.

Manufacturing of Cantor HEA has been described by Soares [4], and the $Al_{0.3}$CrFeCoNi plate was manufactured similarly. Both HEAs were cast, homogenized in vacuum, and hot rolled into plates. Hence, the available materials were a 7mm thick $Al_{0.3}$CrFeCoNi plate and two 2mm thick Cantor plates, shown in Figure 7.1.

Figure 7.1 *Cantor (left) and $Al_{0.3}$FeCoCrNi (right) plates.*

A servo hydraulic testing machine was used for the quasi-static tests and SHPB and SHTB set-ups were used for the dynamic test; the specimens in the SHTB set-up were

glued to the bars. Table 5 shows the properties and diameter of the bars and typical operating parameters of the SHB at Tampere University.

Table 5 *Properties and range of action of the SHB systems from TUNI.*

Bar	Material	Density (g/cm^3)	Elastic modulus (GPa)	Propagation speed of the wave (m/s)	Diameter (mm)	Maximum force of the set-up (kN)
Input (SHPB)	Maraging	8.47	198	4835	21.8	50-100
Output (SHPB)	Maraging	8.47	198	4835	21.8	
Input (SHTB)	HSS 4340	7.84	209.18	5166	21.8	6-10
Output (SHTB)	Aluminum 2007	2.72	70.2	5080	22.1	

7.2 Preliminary selection of sample geometries

The SHB set-ups used in the laboratory are composed of solid bars. As punch and double notch specimens need a hollow output bar, they were no suitable for his study. Other reasons to discard these geometries were their manufacturing complexity (especially the notched-punch specimen) and the unreliability of results (double notched specimen) for the shear tests. [96], [97]

The HEA plates were 7 and 2 mm thick, which was not enough for manufacturing cylindrical samples such as cylindrical Rittel or hat specimens. Nevertheless, Rittel's specimen contains Abaqus sketches of the Rittel specimen in case further research is done. Another reason to discard the hat specimen was its incompatibility with DIC.

Therefore, non-cylindrical S-shaped specimens and flat-hat specimens were studied and analysed. A modified S-shaped geometry, used for testing a steel and Al alloys [104], was used for studying the performance of the Cantor alloy in shear-SHTB tests. For the shear-SHPB tests ($Al_{0.3}$CrFeCoNi alloy) were studied flat-hat specimen and S-shaped geometry, which have been tested in Cantor, Ti and Al alloys [98], [100]**.** The dimensions of the gage sections were firstly the same as the ones used by Budiwantoro [98], Arab [100] and Gardner [104], except for the thickness, which was adapted to the thickness of the available plates. Budiwantoro et al. [98] studied the dynamic response of the aluminum alloy 6061-T651 testing multiple geometries with different dimension of the gage section each; those geometries with a 5° shear angle provided the best data and therefore, the same dimensions were chosen for the preliminary flat-hat. The dimensions of the gage sections used in the models of the shear geometries are shown in Table 6.

Table 6 *Preliminary gage section dimensions.*

Specimen	Length (mm)	Width (mm)	Thickness (mm)	Shear-area (mm^2)
Standard S-shaped [100]	2	0.2	5	10
Flat hat [98]	2	0.2	5	10 x 2 =20
Shear (in tension) [104]	5	1	1	5

The shear stress used for the calculation of the shear force at the interface of the SHB and cause a strain rate of 2800 s^{-1} was the maximum flow stress from Table 1 to Table 3 (Table 1: 1220 MPa at 40 % plastic strain). The reason why 1220 MPa were used in Equations 2 and 3 without applying Von Mises criterion was to keep a safety margin for operating the SHB. Table 7 shows the force values at the specimen-bar interface, which were within the typical operating parameters.

Table 7 *Operating requirements for generating a shear strain rate of 2800 s^{-1} on the gage section of the preliminary geometries.*

Specimen	Velocity at the interface (m/s)	Force at the interface (kN)	Maximum force of the SHB system (kN)
Standard S-shape	0.56	12.2	50 - 100
Flat hat	0.56	24.4	50 - 100
Shear (in tension)	2.8	6.1	6 -10

7.3 First simulation approach

Abaqus gives freedom when choosing the units of the physical problem, but it is important to keep a consistent system of units [121]. Otherwise, problem resolution and analysis of results will be wrong. The system of units used it highlighted in Figure 7.2.

MASS	LENGTH	TIME	FORCE	STRESS	ENERGY	DENSITY	YOUNG's Modulus	GRAVITY
kg	m	s	N	Pa	J	7.83e+03	2.07e+11	9.806
kg	cm	s	1.0e-02 N			7.83e-03	2.07e+09	9.806e+02
kg	cm	ms	1.0e+04 N			7.83e-03	2.07e+03	9.806e-04
kg	cm	us	1.0e+10 N			7.83e-03	2.07e-03	9.806e-10
kg	mm	ms	kN	GPa	kN-mm	7.83e-06	2.07e+02	9.806e-03
g	cm	s	dyne	dyne/cm²	erg	7.83e+00	2.07e+12	9.806e+02
g	cm	us	1.0e+07 N	Mbar	1.0e+07 Ncm	7.83e+00	2.07e+00	9.806e-10
g	mm	s	1.0e-06 N	Pa		7.83e-03	2.07e+11	9.806e+03
g	mm	ms	N	MPa	N-mm	7.83e-03	2.07e+05	9.806e-03
ton	mm	s	N	MPa	N-mm	7.83e-09	2.07e+05	9.806e+03
g	cm	ms	1.0e+1 N	1.0e+05 Pa		7.83e+00	2.07e+06	9.806e-04
kg	mm	s	mN	1.0e+03 Pa		7.83e-06	2.07e+08	9.806e+03
lbf-s²/in	in	s	lbf	psi	lbf-in	7.33e-04	3.00e+07	386
slug	ft	s	lbf	psf	lbf-ft	1.52e+01	4.32e+09	32.17
kgf-s²/mm	mm	s	kgf	kgf/mm²	kgf-mm	7.98e-10	2.11e+04	9.806e+03

Figure 7.2 *Reference table for consistent system of units. [153]*

The material models used in this work assume that the material has the same behaviour in tension and in compression as the inputted data was in terms of true stress – true

strain (Tables 1 to 3) [121]. As the only available mechanical response is from the Cantor alloy [4], such data served as reference for designing both Cantor and $Al_{0.3}CrFeCoNi$ HEAs at $3*10^{-4}$ s^{-1}, 10^{-1} s^{-1} and 2800 s^{-1}.

Neither of the models included the projectile, input and output bars in the high-strain rate tests, nor the grips used in the quasi-static tests. The main reason was to reduce the computational time of the simulations. Additionally, it was possible to check if applying the boundary conditions directly to the bars-specimen interface provides accurate enough results. Adequate boundary conditions were applied on the surface of the specimen to mimic the restrictions they experienced as if they were mounted in the set-ups, as represented in Figure 7.3.

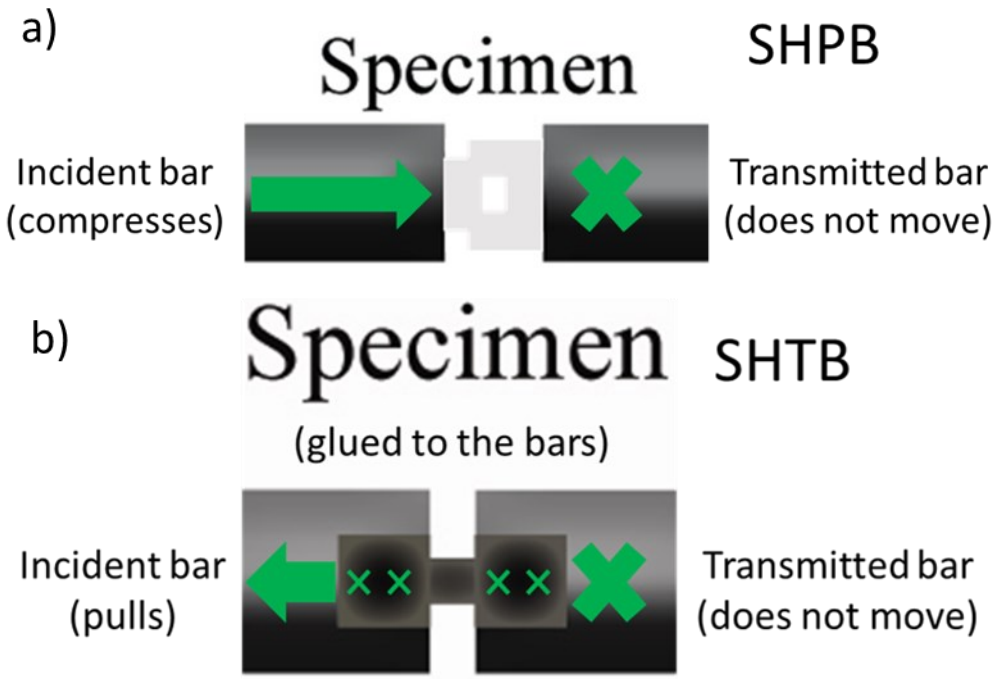

Figure 7.3 *(a) Schematic representation of the boundary conditions in (a) shear (in compression) and (b) shear (in tension) simulations.*

7.4 Explicit-dynamic simulations

7.4.1 Geometry and mesh

In the part module, the geometries of the model were created as an extruded solid 3D deformable based on the design assumptions. The extrusion “depth” was the same as the thicknesses of the available plates. Figure 7.4 shows the sketches of the standard S-shaped specimen and flat-hat specimen.

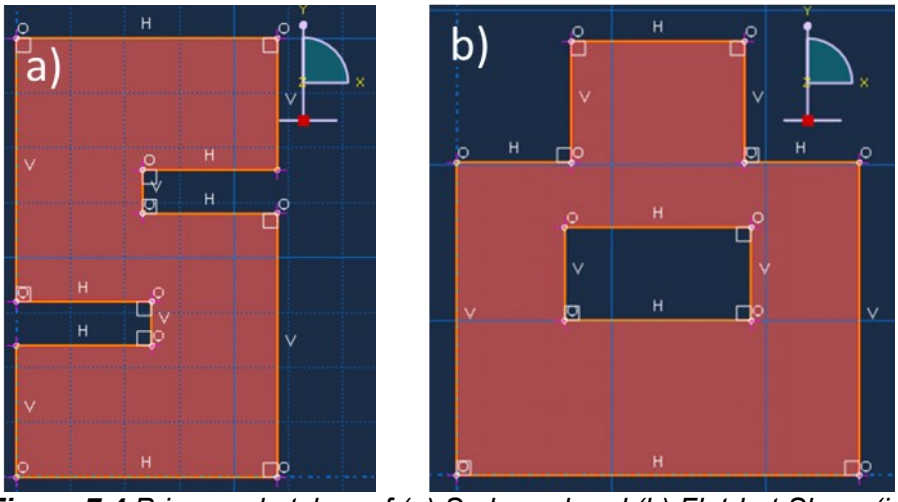

Figure 7.4 *Primary sketches of (a) S-shaped and (b) Flat-hat Shear (in compression) specimens.*

In the case of Shear (in tension) specimen, generating the geometry included a few more steps. After defining the contour (like in Figure 7.4-a), “Create cut: Extrude” feature was used to mill the gage section. This step is shown in Figure 7.5 and was done for both sides. Subdividing the geometry by creating partitions simplifies this labour.

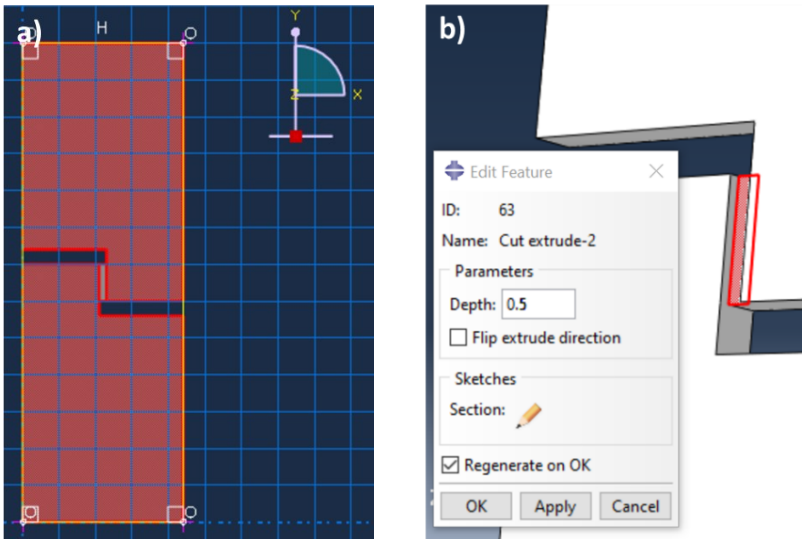

Figure 7.5 (a) *Preliminary sketch of the Shear (in tension) specimen; (b) close-up at the milled gage section.*

Shear (in compression) specimens had 0.1 mm radius fillet and Shear (in tension) specimen had 0.5 mm radius fillet. The addition of roundings or fillets at the corners of the gage sections (Figure 7.6) reduces stress concentration in those regions, increasing the probabilities of the component to fail due to ASB formation and not due to a design error. Also, it helps Abaqus software by not making too stiff that region, leading to more accurate results [121]. This relates to the mesh generation.

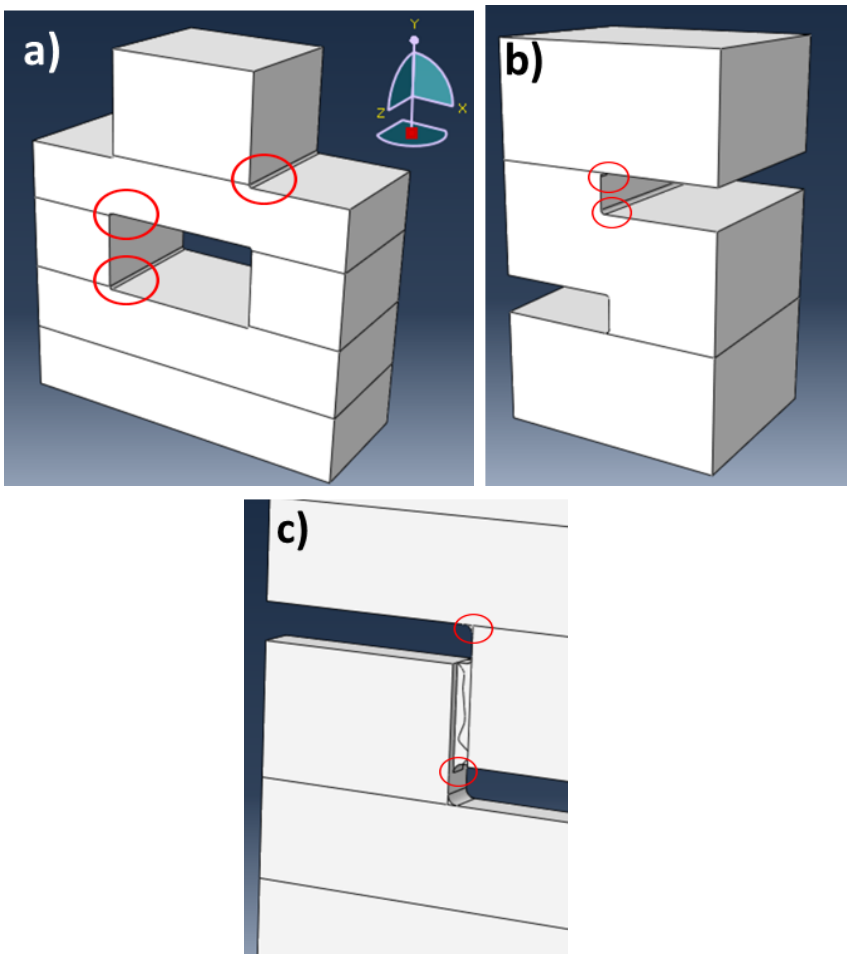

Figure 7.6 *Fillet placing in the (a, b) Shear (in compression) and (c) Shear (in tension) specimens in regions of potential stress concentration.*

According to Abaqus guidelines, the 3D-stress linear hexahedral mesh with reduced integration elements should be used (C3D8R) [120]. Choosing the mesh type is as important as choosing the optimum mesh size. The gage section should contain a fine mesh due to the large distortions and stress concentrations that it experiences. While those regions that are not supposed to suffer any plastic deformation have a larger mesh size to reduce the computational cost. The difference in mesh size at the interface of the mentioned regions should not be large; otherwise, stress calculation is inaccurate [121]. The creation of the previously mentioned cell partitions with a fixed number of seeds can overcome this issue. Fillets also contain a fixed number of seeds due to the importance of analysing the stress and strains evolution in that region [128], [131]. The rest of the cell partitions in the specimen ensure mesh compatibility between its different parts. Figure 7.7 shows the meshes originally used for the simulations.

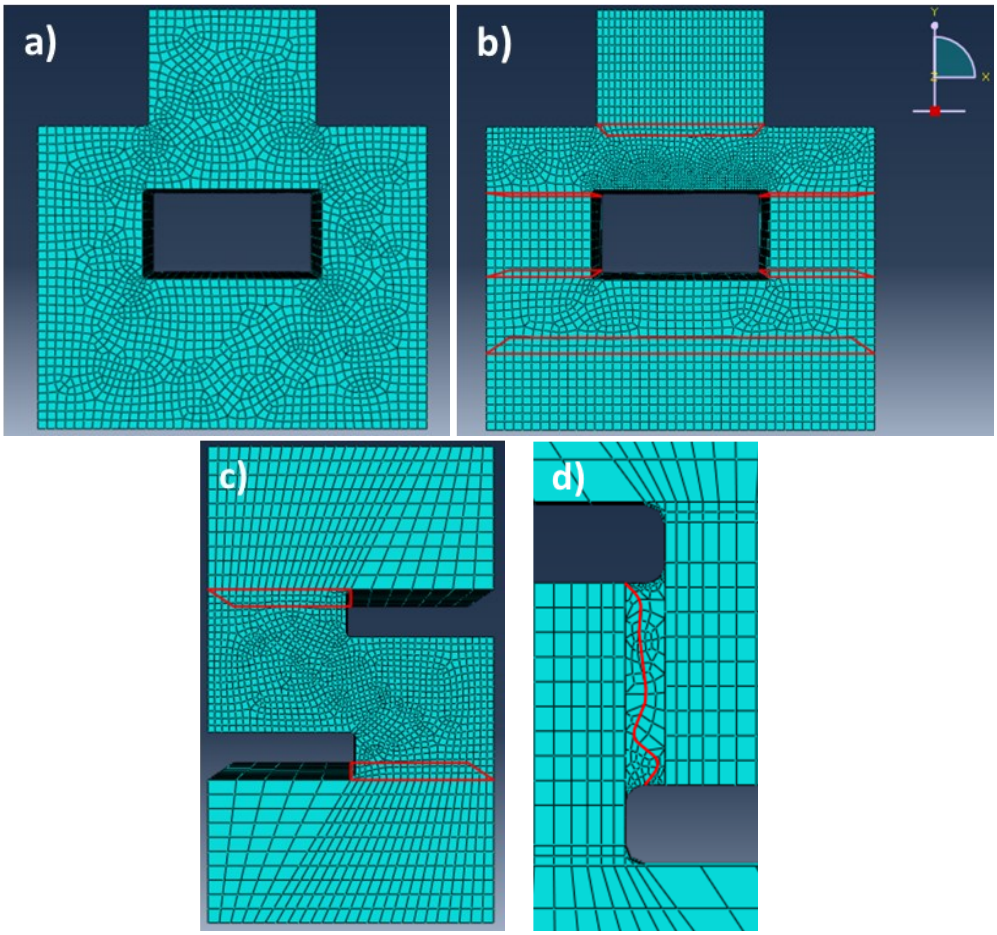

Figure 7.7 *Difference in mesh generation (a) before and (b) after the creation of cell partitions (highlighted) in the flat-hat specimen. (c) Mesh distribution in the S-shaped specimen; (d) mesh distribution in the gage of the Shear (in tension) specimen.*

7.4.2 Loads and boundary conditions

Figure 7.3 was a first approximation of how to implement the boundary conditions in the model. However, as the SHB were not included, loads and boundary conditions need to be implemented in the most realistic way, physically speaking. Shear-SHPB specimens were sandwiched, meaning that while one surface (input bar ≈ upper surface) compresses the specimen at a certain velocity, the other (output bar ≈ lower surface) kept its position. Shear-SHTB surfaces were glued to the bars and pulled. The surfaces of the specimen glued to the output bar kept their position while the surfaces glued to the input part were pulled from their original position at a certain velocity. Figure 7.8 shows the boundary conditions applied in each model, and the velocity values are those from Table 7.

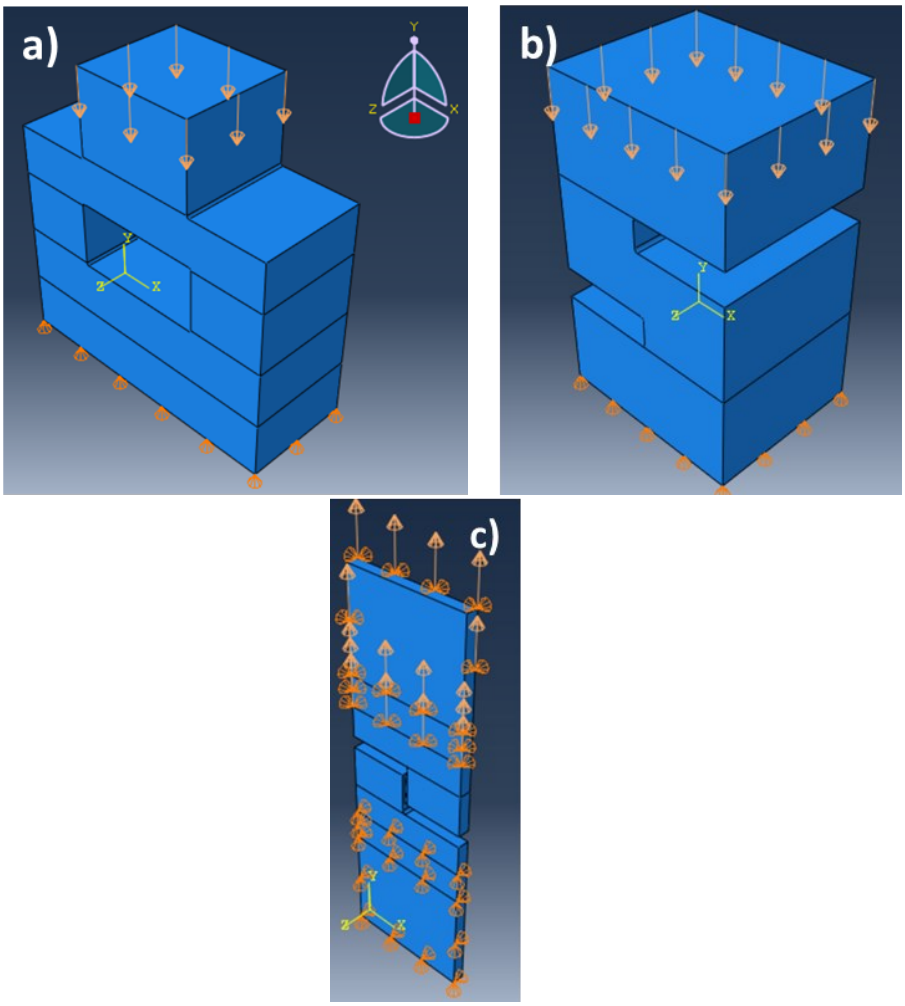

Figure 7.8 *Boundary condition application on (a-b) Shear (in compression) and (c) Shear (in tension) specimens.*

7.4.3 Simulation parameters

Material properties were the same as described Materials and equipment, and the time step was dynamic explicit to solve this dynamic model. The software automatically estimates the number of time increments based on the duration (time step) of the simulation, which was 160 µs for the SHPB and 600 µs for the SHTB. These models include non-linear effects of large displacements (Nlgeom).

Specifying the field and history outputs is important. Field output is generated from data spatially distributed over the model and in most cases, Field outputs are visualized using deformed shape plots. History output is generated from data at specific points of the model, commonly visualized with XY plots [120], [121]. Abaqus generates a large quantity of data, so certain variables were stored every X units of time, either respect the time of the experiment or the time of the simulation. Table 8 shows the general variables selected for the field output. For the history output, ALLEN (all energy variables) includes

ALLKE (kinetic energy), a term that should not vary throughout the simulations to ensure the model works properly.

Table 8 *General field output variables.*

S	Stress components and invariants
MISES	Mises equivalent stress
PE	Plastic strain components
PEEQ	Equivalent plastic strain
LE	Logarithmic strain components
U	Translations and rotations
V	Translational and rotational velocities
A	Translational and rotational accelerations
RF	Reaction forces and moments

To extract and analyse afterwards the forces and displacement at specific regions of the specimen during the simulations, the variables should be gathered in a history output for a set of nodes. For the shear-SHPB geometries, a set of nodes was created at the contacting surfaces of the flat-hat specimen and at the elastic region of the S-shaped specimen to obtain the displacement and velocity values (U2 and V2 respectively). To obtain the force at the specimen-input bar contacting surface, i.e., when the load is applied, a reference point can be created and coupled to such surface. The load is applied to the reference point instead of the contacting surface. An advantage of making this choice it that the history output of the reference point (RF2: reaction force in y-axis) averaged the force values experienced at the coupled surface.

Shear-SHTB cannot make use of reference points as the boundary conditions are applied over the two glued surfaces. Instead, an inner surface that cuts through the specimen was created [121]. Write in the input file, before "*End Assembly" the following lines,

```
*Surface, type=CUTTING SURFACE, name=RAMON_2
0,37,2,0,1,0
ALL
```

where, 0, 37 and 2 were respective X, Y and Z coordinates of a point in the cutting plane in the initial configuration, which was in the grip section. The values 0,1 and 0 were the respective X, Y and Z coordinates of a vector normal to the cutting plane in the initial configuration, i.e., the Y direction in these models. The third line (ALL, by default) refers to the number of cut elements or set of elements included in the element-based surface created. Adding an integrated output in the history output section of the input file, before "*End Step", is necessary to generate a history output for the cutting surface,

```
*INTEGRATED OUTPUT, SURFACE=RAMON_2, VARIABLE=ALL
```

where ALL includes all the integrated output variables applicable to this procedure. Nevertheless, the variable SOF2 (total force on the surface) provides the averaged reaction force that the specimen experienced during the simulation.

Finally, run the simulations creating a job with full nodal output and double precision to obtain more accurate results. This choice implies using 20 to 30% more CPU compared to single-precision executable [124].

7.5 Implicit, quasi-static simulations

These simulations were done after performing the physical experiments as a reasonable time-period for the simulation was necessary to establish. The models followed the same sequence previously described in Explicit-dynamic simulations using the final specimen designs. However, the velocity of the compression (loading condition) was adjusted, as well as the interaction between contacting surfaces and the time step to those suitable for the implicit model. Table 9 shows the time-period used for each simulation and sample and the number of incrementations. The later term was slightly above the default 100 to ensure simulations end at the established time-period. The jobs created have single precision with single nodal precision output as double precision analysis is restricted to Explicit models.

Table 9 *Experimental strain rate and simulation strain rate, time-period and number of increments of the implicit models.*

sample	Experiment strain rate (s^{-1})	Data strain rate (s^{-1})	Exp. and simulated time-period (s)	Number of increments
Shear (in tension) 5	10^{-1}	10^{-1}	30	105
Shear (in tension) 4	10^{-3}	$3*10^{-4}$	2597	103
Shear (in compression) 1	$2.5*10^{-3}$	$3*10^{-4}$	1910	101

One of the most noticeable differences between the models was in the force-displacement curves. Vibrations in the explicit model made necessary the further treatment of data for better readability, e.g., using smoothening functions; while the curves from the implicit model can be used directly.

7.6 Modifications of the preliminary designs

This section explains briefly the changes performed in the design of the preliminary geometries and shows the final designs and dimensions of the gage section.

The Shear (in tension) geometry, a variation of a S-shaped geometry, was adapted to the metric system, and the length of the region glued to the bars increased so the DIC

cameras can focus properly the gage section and avoid any reflections from the testing bars.

The S-shaped Shear (in compression) geometry was not manufactured because the models showed a complex stress state at the gage section that hindered shear stress and strain concentration.

The flat-hat geometry experienced the highest number of modifications. First, the removal of the base that keeps connected the two brims to ease sample manufacturing. Then, the length of the brims and head of the geometry were shortened, and the dimensions of the gage section were changed so both SHTB and SHPB specimens have similar shear angle. These modifications led to the creation of an additional part in the model called “holder”; made of steel and kept elastic during the simulations, the function of the holder was to prevent the brims from splitting. Assembly and interaction (frictionless holder-brim contact) modules were necessary to place both parts and establish a contact interaction between them.

The following section shows the final geometries used for carrying out the experiments and analysing shear localization, the detailed designs are shown in Specimen designs. Table 10 shows the dimensions of the gage section together with the re-calculation of the force needed to induce a strain rate of 2800 s^{-1}, it was still within the typical operating parameters.

Table 10 *Final dimensions of the gage sections for the simulated models.*

Sample	Gage length (mm)	Gage width (mm)	Gage thickness (mm)	Gage shear area (mm^2)	Velocity at the interface (m/s)	Force at the interface (kN)
Shear (in compression)	2	0.4	5	10 * 2 = 20	1.12	24.4
Shear (in tension)	5	1	1	5	2.8	6.1

7.7 Specimen manufacturing and experimental testing

Figure 7.9 a) shows the specimens manufactured from Figure 7.1 plates. The specimens were EDM (Electron Discharge Machining) cut and the gage section from the Shear (in tension) specimens milled by an external company. The Heavy Lab from Tampere University produced the holders for the Shear (in compression) specimens. Five specimens were manufactured from each plate. Table 11 and Table 12 show the averaged dimensions of the manufactured specimens according to symbols from Figure 7.9 b) and c), and using a calliper and a micrometre (tool’s tolerance: ±0.01 and ±0.001 mm respectively).

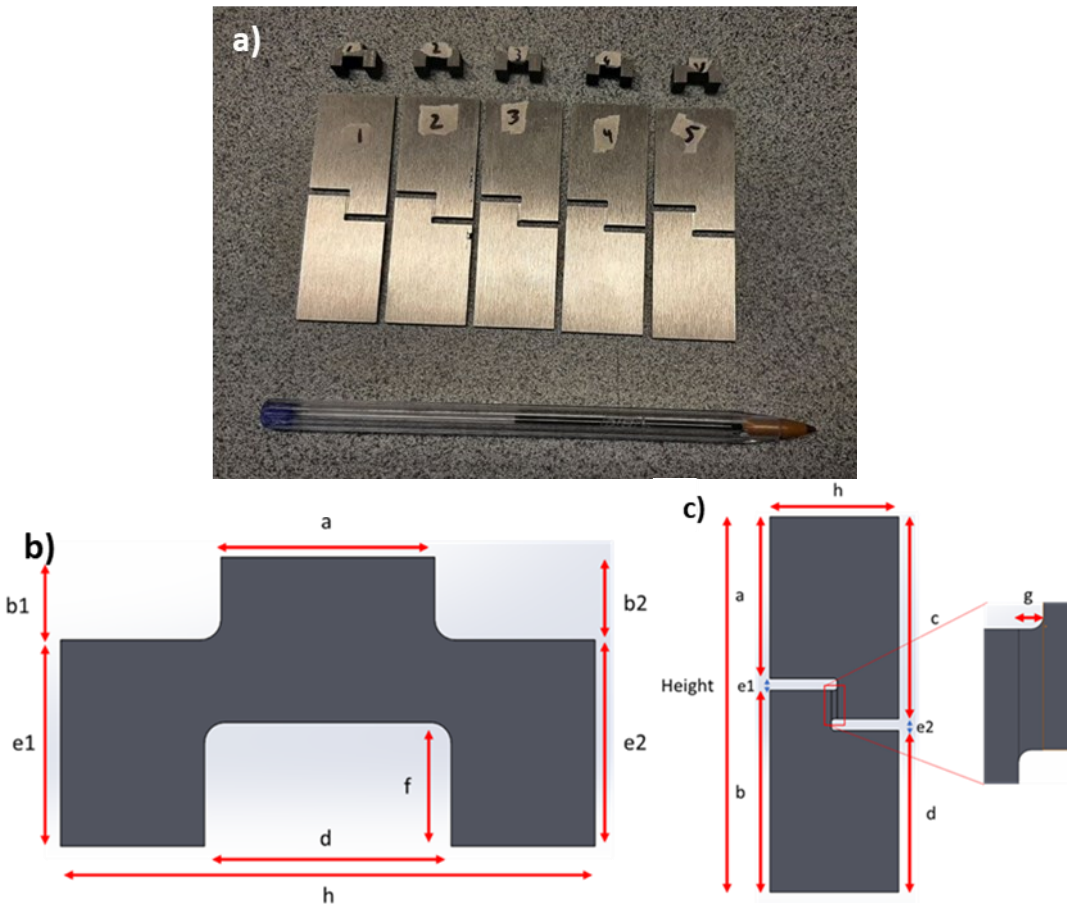

Figure 7.9 *(a) Manufactured samples; schematic representation of (b) Shear (in compression) and (c) Shear (in tension) specimen with its different dimension names.*

Table 11 *Shear (in tension) averaged dimensions. Units in millimeters.*

	Sample 1	Sample 2	Sample 3	Sample 4	Sample 5
*a	28.02	28.03	28.00	28.00	28.02
*b	34.99	35.00	34.94	34.99	34.99
*c	35.00	35.00	34.95	34.97	34.98
*d	28.05	28.01	28.00	27.99	28.01
e1 = Height - (a + b)	1.99	1.97	2.04	2.01	1.99
e2 = Height - (c + d)	1.96	1.99	2.03	2.04	2.02
*g (width of the gage section)	0.96	0.95	0.94	0.96	0.94
*h	21.98	21.98	21.93	21.95	21.95
** Thickness in the grip region	1.977	1.992	2.082	2.012	1.983
** Thickness of the gage section	1.150	1.100	1.020	1.110	1.140
Length of the gage section = b-d-e2	4.99	4.99	4.91	4.95	4.97
*Height	65.00	65.00	64.98	65.00	65.00

**** Measured with the caliper. ** Measured with the micrometer.***

Table 12 *Shear (in compression) averaged dimensions. Units in millimeters.*

	Sample 1	Sample 2	Sample 3	Sample 4	Sample 5
**a	5.206	5.206	5.219	5.210	5.201
*b1	2.00	2.00	2.00	2.00	2.00
*b2	2.00	2.00	2.00	1.98	2.00
*d	5.99	5.99	6.00	5.99	5.99
** e1	5.084	5.017	5.005	5.019	5.015
** e2	5.079	5.007	5.006	5.014	5.040
*f	3.00	2.99	2.99	2.99	3.00
gage length = (e - f)	2.084	2.027	2.015	2.029	2.015
gage width = (d - a) / 2	0.393	0.390	0.389	0.392	0.395
** h	13.019	13.024	13.019	13.030	13.021
** Thickness	7.485	7.470	7.4073	7.312	7.554

**** Measured with the caliper. ** Measured with the micrometer.***

Shear (in compression) samples were thicker compared to the models. Table 13 presents the force and velocity at the interface recalculated; the force values were still within the typical operating parameters. Hence and, based on the idea that a higher thickness does not affect the stresses values nor their distribution, the thickness of the samples was not reduced, nor the models recalculated.

Table 13 *Requirements for replicating the reference mechanical response in SHB systems.*

Specimen	Velocity at the interface (m/s)	Force at the interface (kN)	Maximum force of the SHB system (kN)
Shear (in tension)	2.66	6.7	6 - 10
Shear (in compression)	1.1	37.00	50 - 100

However, Shear (in tension) specimens were slightly grinded in the grip section for ensuring good adhesion. Shear (in compression) brims and holders were filed down in the areas that were in contact for good fitting. The resulting samples are shown in Figure 7.10.

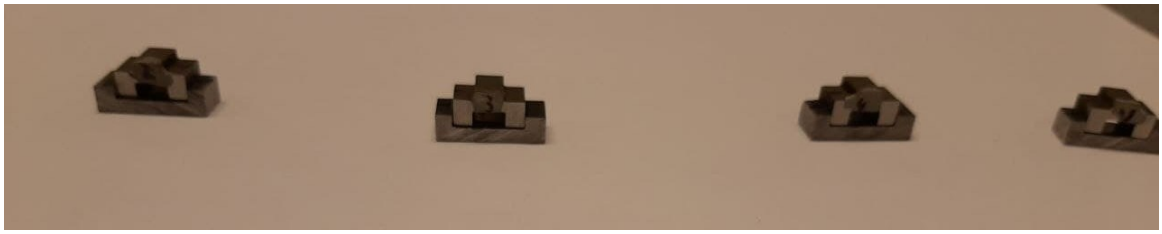

Figure 7.10 *Shear (in compression) samples fitted in their holders.*

Sample 1 from the Shear (in compression) design and samples 4 and 5 from the Shear (in tension) design were tested in the universal testing machine (UTM) in the quasi-static regime. Shear (in compression) test use compression plates, while Shear (in tension) tests use wedge grips. The strain rate was imposed by fixing the velocity of the movable head. The rest of the samples were tested in the SHB in the dynamic regime. A rubber band held the position of the Shear (in compression) specimen fitted in the holder

between the SHPB input and output bars until the experiment started. The Shear (in tension) specimens were glued to the SHTB input and output bars, using a glue and an accelerator. The strain rates were not imposed before the tests. Instead, the pressure of the air chamber that launched the projectile was fixed, and the strain rate was calculated afterwards from the gathered data using the equations from Shear stress-strain calculation. Table 14 summarizes the state of the experiments.

Table 14 *State of the experiments*

	Shear strain rate (UTM)	Launch Pressure (SHB)
Shear (in compression) sample 1	$2.5*10^{-3}$ s^{-1}	-
Shear (in compression) sample 2	-	0.8 bars
Shear (in compression) sample 3	-	0.8 bars
Shear (in compression) sample 4	-	1.6 bars
Shear (in compression) sample 5	-	1.6 bars
Shear (in tension) sample 1	-	7.3 bars
Shear (in tension) sample 2	-	6 bars
Shear (in tension) sample 3	-	3 bars
Shear (in tension) sample 4	10^{-3} s^{-1}	-
Shear (in tension) sample 5	10^{-1} s^{-1}	-

7.8 Data analysis

This section explains how to obtain the force-displacement and shear stress – shear strain from the data gathered from the outputs of the simulations and the ε_i, ε_r and ε_t obtained from the SHB experiments.

7.8.1 Simulated models

An .odb file was created after finishing the simulations, and with Abaqus (Viewer) the user can access to the file and all the requested field and history outputs. The most interesting outputs to analyse are the reaction force at the reference point (SHPB geometry) or the cutting surface (SHTB geometry) and the displacement in the y-axis of the nodes in the region adjacent to the input bars, i.e., where the load was applied. The force – displacement curve can be extracted directly from the .odb file, but by applying Equations 36 and 37 and considering the final dimensions of the geometries from Table 10, the user obtains also the shear stress-strain values. Figure 7.11 exemplify the mentioned procedure with the Shear (in compression) model subjected to a strain rate of $3*10^{-4}$ s^{-1}.

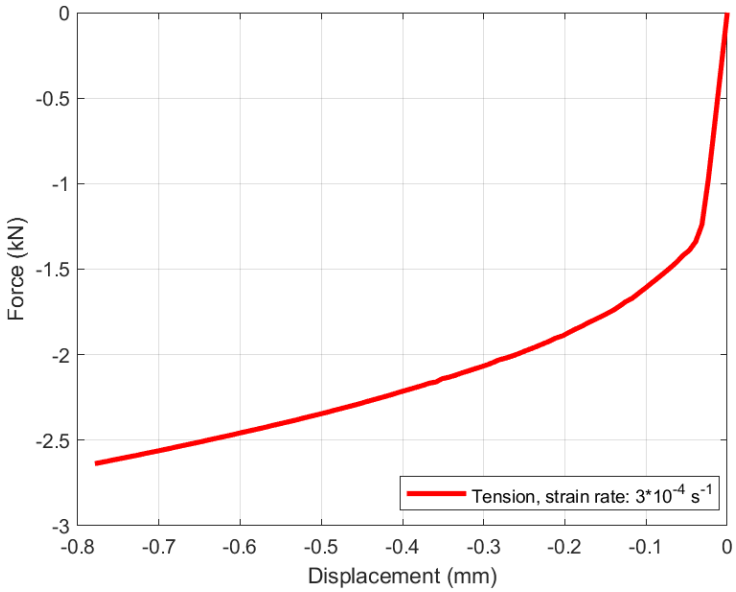

Figure 7.11 *Force-displacement curve of the Shear (in compression) specimen implicit model (shear rate = 3*10^{-4} s^{-1}).*

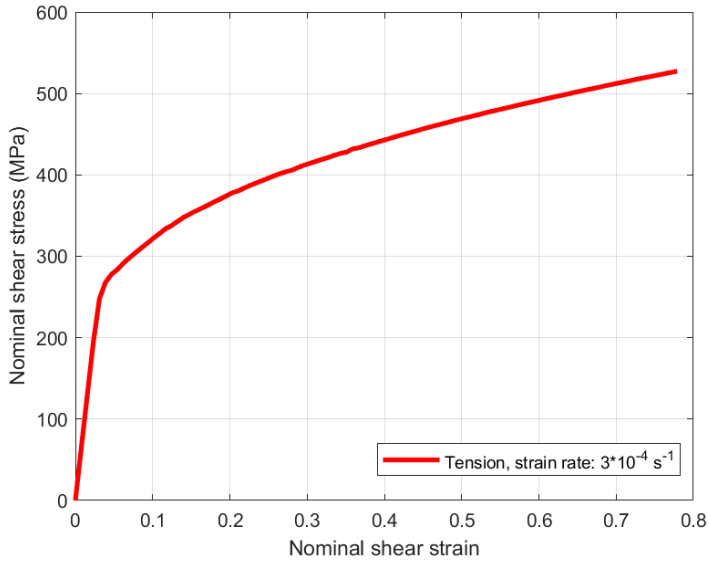

Figure 7.12 *Shear-stress-shear strain curve of the Shear (in compression) specimen implicit model (shear rate = 3*10-4 s^{-1}).*

7.8.2 Force-displacement curves

Five Shear (in compression) and Shear (in tension) samples were tested in quasi-static and dynamic conditions as described in the previous section (Table 14). In the quasi-static tests, the velocity of the movable head was measured as well as the force and the displacement, data gathered by the loading cell and the extensometer respectively. Therefore, Equations 36 to 38 can be applied directly. However, Table 5 and Equations from 30 to 38 were used to obtain the shear stress and shear strain values in the SHB tests, shown in Figure 7.13. During the tests, force equilibrium was assumed, and the bar properties were considered homogenous, isotropic and elastic.

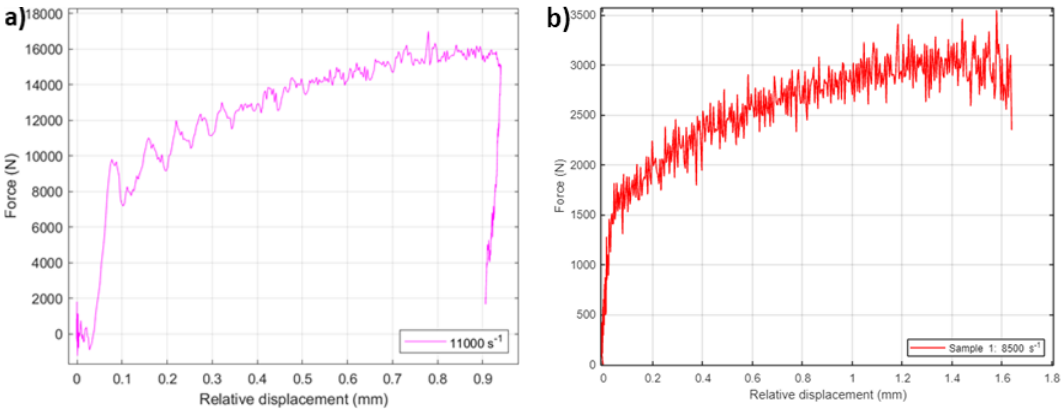

Figure 7.13 *Experimental force - relative displacement curves of (a) SHPB sample 5 and (b) SHTB sample 1.*

The first reverberations in the SHPB curves (Figure 7.13-a) were cleaned as they might be caused by the lubricant present at the interface between the bars and the sample. Also, last data points for both SHPB and SHTB samples after failure were removed. Figure 7.14 shows the resultant smoothened shear stress-strain curves via a “smooth” MATLAB function with the method “rloess” or robust local regression using a polynomic model of second order.

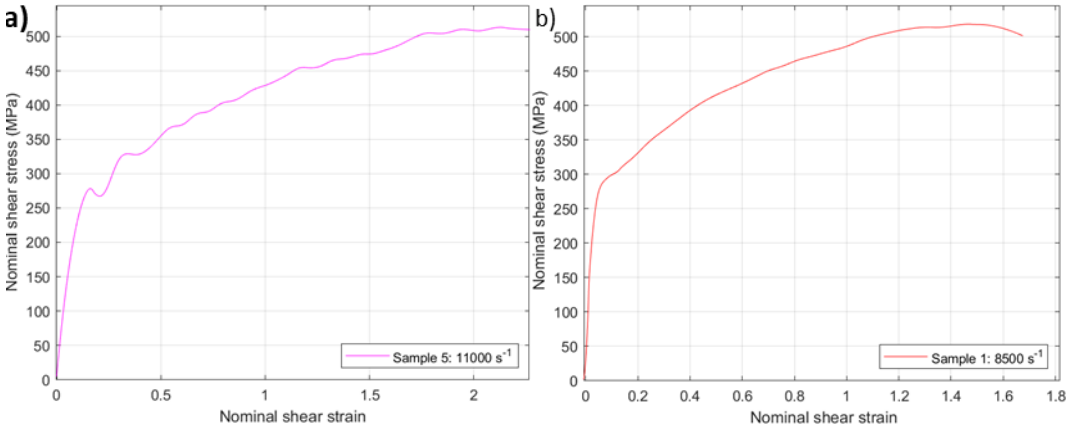

Figure 7.14 *Smoothened experimental shear stress-strain curves of (a) SHPB sample 5 and (b) SHTB sample 1.*

7.9 2D-DIC methodology

The DIC camera stood on a frame together with two LED lights on each side of the camera. A 2D calibration plate with a 0.5 mm pattern was used to calibrate the system for lens distortion, illumination of the images and scaling of the measurements. Figure 7.15 illustrates the DIC set-up.

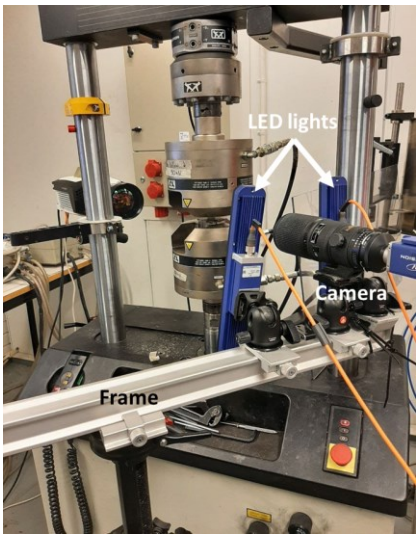

Figure 7.15 *DIC system set-up for the quasi-static tests.*

The samples were cleaned with acetone and ethanol before painting the contrast pattern. The painted pattern can be either only black dots or a white background with black dots. The latter pattern provides better contrast and reduces the brightness of the surfaces while improves the performance of the software. Figure 7.16 shows an example of the patterned surfaces. Performing the tests right after applying the pattern is important so the paint does not fly off from the samples during the tests.

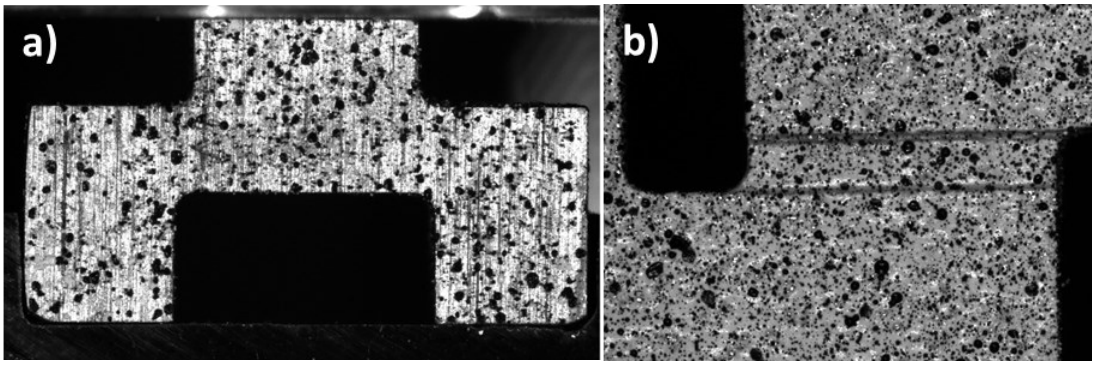

Figure 7.16 *Close-up to the patterned surface of the (a) Shear (in compression) sample and (b) Shear (in tension) sample.*

The DIC system successfully recorded all the tests. Figure 7.17 shows the shear band developed at the gage section of Shear (in tension) sample 5, such phenomenon led to the failure of all the specimens and was expected from the models.

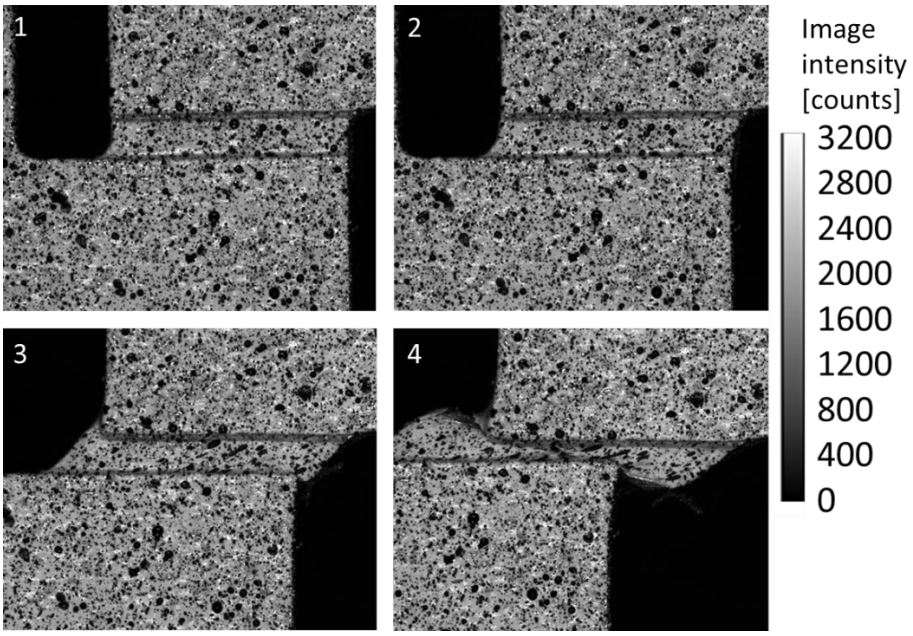

Figure 7.17 *Series of images obtained during the testing of Shear (in tension) sample 5 (strain rate= 10^{-1} s^{-1}).*

The Shear (in compression) samples developed a shear band in the gage section too, but not all the specimens failed similarly. Samples 1 (quasi-static regime), 2 and 3 (dynamic regime, launch pressure =0.8 bars) got stuck in the holder. While samples 4 and 5 (dynamic regime, launch pressure =1.6 bars) broke into three and two pieces (Figure 7.18) respectively.

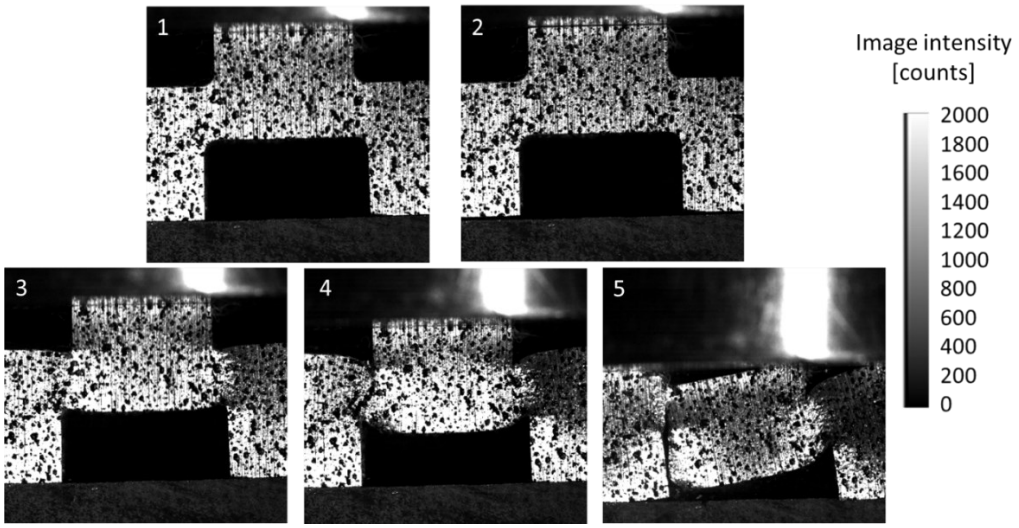

Figure 7.18 *Series of images obtained during the testing of Shear (in compression) sample 5 (pressure = 1.6 bars; strain rate= $1.1*10^{4}$ s^{-1}).*

The mask or region delimited for the calculation was drawn automatically by the software. Some points of the mask were manually adjusted for better fitting or, as in Figure 7.19 a), to exclude reflections. The pixel subset size was manually fixed for each case, but samples tested in quasi-static conditions had a pixel subset size three times larger than samples tested in dynamic conditions. The step size was automatically calculated based

on the pixel subset size. The calculation mode was set to accurate to ensure a high number of iterations per calculation. The second-order shape function provides a better precision than the first order one for larger and non-uniform deformations; this relates to the correlation mode 'Sum of differential'. 'Sum of differential' is used when the displacement between the first and the last image is larger than the pixel subset size and allows a safer calculation mode at a cost of lowering accuracy (errors stack). [147], [148]

Images were taken at the very early stages of the tests (image 2 in both Figure 7.17 and Figure 7.18), right before sample fails (image 4) and approximately in an intermediate point between the previous two (image 3). At the mentioned frames, displacement, von mises strain and shear strain were calculated. Table 15 summarizes the parameters used in the DIC calculations.

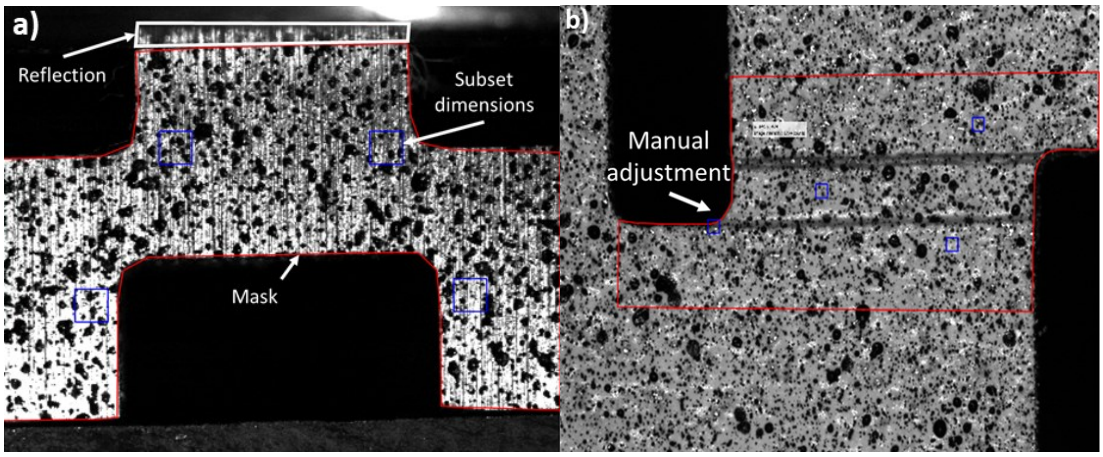

Figure 7.19 Example of the mask created for the DIC calculations of the (a) *Shear (in compression)* specimen and (b) *Shear (in tension)* specimen.

Table 15 *DIC calculation settings.*

Specimen		Recording frequency (Hz)	Subset size (pixels)	Step size (pixels)	Calculation mode	2nd order shape function	Correlation mode
Compression	Low loading rate (Sample 1)	2	75	25	Accurate	On	Sum of differential
	High loading rate (Sample 5)	$6.2*10^4$	25	8	Accurate	On	Sum of differential
Tension	Low loading rate (Sample 5)	5 and 17	49	16	Accurate	On	Sum of differential
	High loading rate (Sample 1)	$1.6*10^5$	15	5	Accurate	On	Sum of differential

8. RESULTS AND DISCUSSION

The chapter explains in more detail the changes done to the preliminary designs to improve shear localization at the gage section and manufacturability. Results from the simulated models are shown and compared with the DIC measurements of samples tested under similar loading conditions, either quasi-static or dynamic. The chapter concludes showing the shear stress – strain curves obtained from the experiments and comparing them with the literature values. Throughout the comparison, possible sources of error are explained together with the offering of alternatives for improving future investigations in this area.

8.1 Final designs

This section explains in more detail the changes done to the preliminary designs already mentioned in Modifications of the preliminary designs.

8.1.1 Shear (in tension) specimen

In the closest region to the gage section, the 0.5 mm radius fillets (Figure 8.1-a) were changed to elliptical fillets (Figure 8.1-b). The reason was improving the transmission of stresses between the gage and the elastic parts of the specimen. Stresses were more localized around the gage using elliptical fillets, but the specimen was more difficult to manufacture. Therefore, the 0.5 mm radius fillet was chosen for the model. Figure 8.1 c) shows an additional simulation where the length of the shear area was increased from 5 mm to 7 mm and the width was reduced from 1 mm to 0.7 mm. The purpose was already mentioned previously, to examine the behaviour of both Shear (in compression) and Shear (in tension) geometries under the same shear angle. However, with the latter design there was a greater risk of deviation from the ideal simple shear stress state, and a higher localization of the stresses and strains out of the gage section. Hence, the preliminary geometry kept a gage length of 5 mm, 1 mm width and 0.5 mm radius fillets.

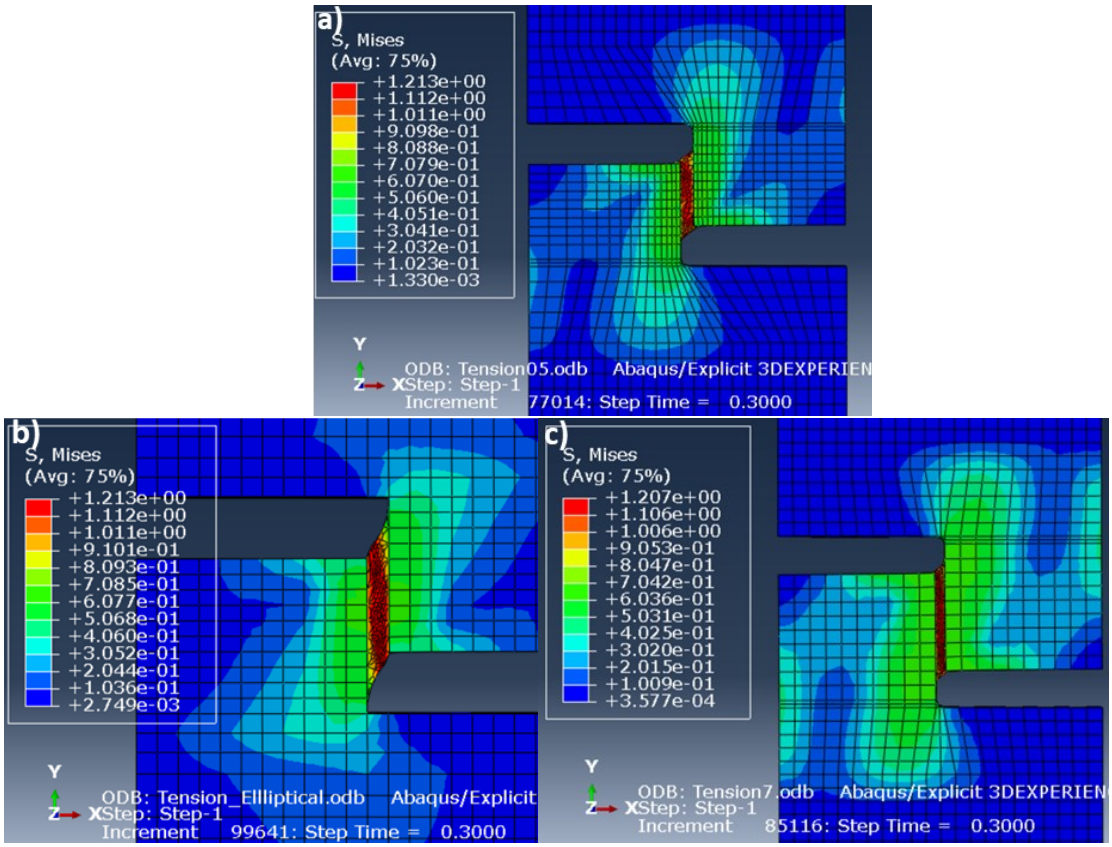

Figure 8.1 *Von mises stress distribution in the Shear (in tension) specimen: (a) 0.5 mm radius fillets and 5 mm gage length; (b) elliptical fillets and 5 mm gage length; (c) 0.5 mm radius fillets and 7 mm gage length.*

Figure 7.9 shows the final design of the shear-SHTB specimen. Its dimensions are specified in section 10.2. The length of the region glued to the bars was larger (28 mm) than the required (25 mm) so the DIC camera can focus on the gage section and avoid any reflection from the bars.

8.1.2 Shear (in compression) specimen

The S-shaped shear-SHPB was discarded at the modelling stage considering the resultant field output. Figure 8.2 shows the two reasons that led to that decision. First, the complex stress state at the shear region hindered shear-stress concentration. Secondly, the areas highlighted with a circle were too close at the end of the virtual test, which could compromise the gathered data if those regions make contact during the test.

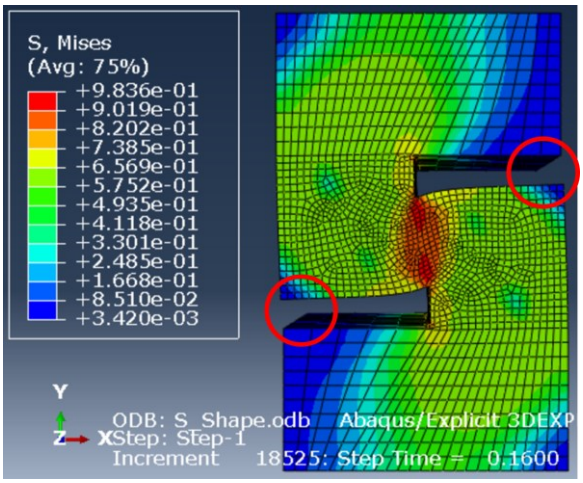

Figure 8.2 *Von mises stress distribution in the S-shaped Shear (in compression) specimen.*

Regarding the flat-hat design, Figure 8.3 shows the stress and strain at high-strain rate impact. Most of the specimen remained in the elastic regime, and the region that concentrated most of the stress and plastic strain was the gage section, although their distribution was not homogeneous. It resembles a behaviour already observed in other materials tested with the same geometry [107]–[114]. However, manufacturing the flat hat according to the preliminary concept brought out some difficulties.

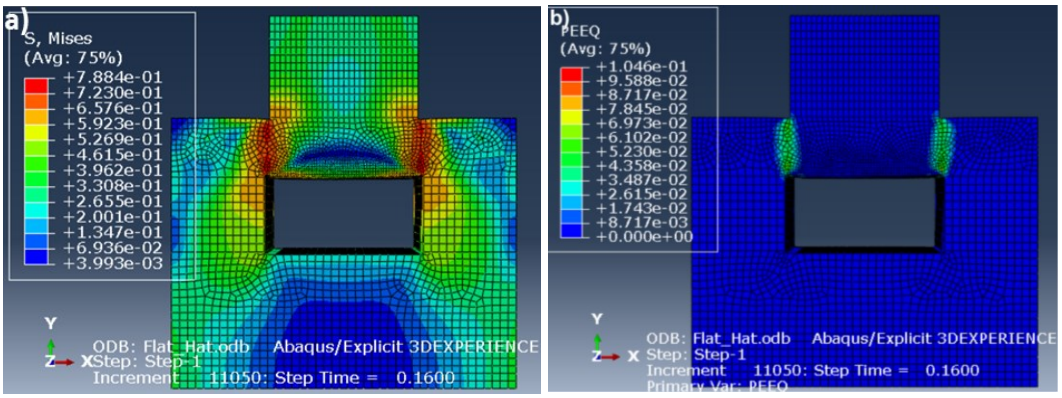

Figure 8.3 *Distribution of (a) Von mises stress and (b) equivalent plastic strain in the flat-hat specimen.*

First, the reduced dimensions and location of the base that connected the brims required precise, and expensive tools. Removing such connection led to the geometry seen in Figure 8.4, which replicated the behaviour of the preliminary flat-hat model only at the beginning of the impact. Brims split and the stresses and strains were no longer concentrated in the gage section.

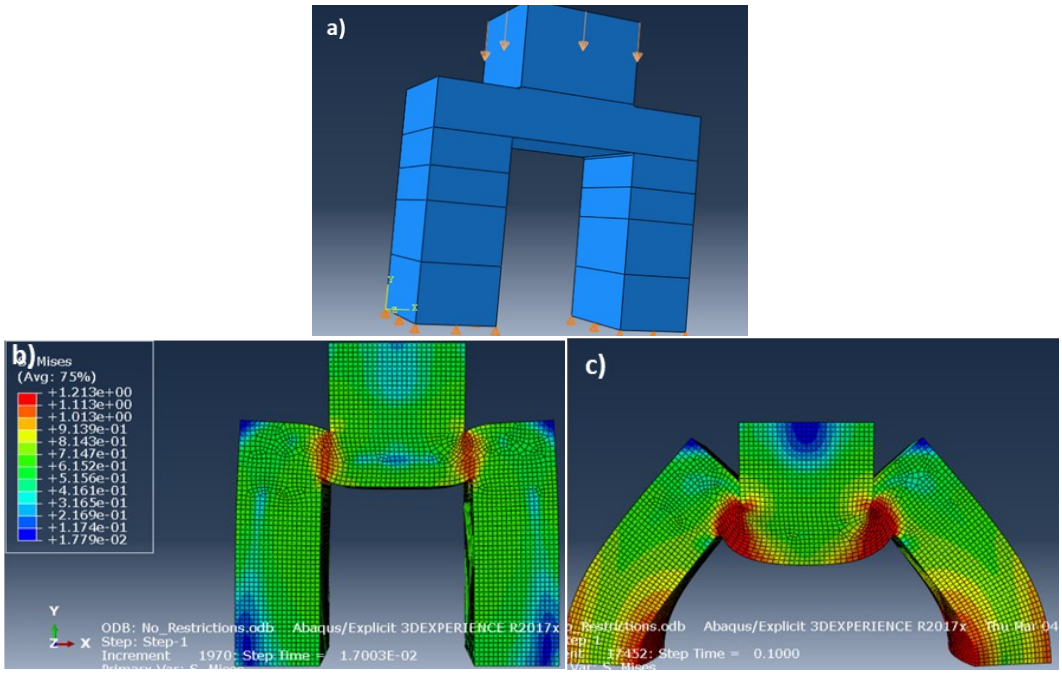

Figure 8.4 (a) *Application of the boundary conditions on the modified hat-specimen. Distribution of the Von mises stresses at (a) the beginning of the test (t= 2 μs) and (b) at t = 100 μs.*

A solution to the splitting of the brims was limiting their movement in the direction perpendicular to the compression. In the simulations, extra boundary conditions were added, like those from Figure 8.5 (a-c). Stresses and strains were once again concentrated in the shear region throughout the whole simulation.

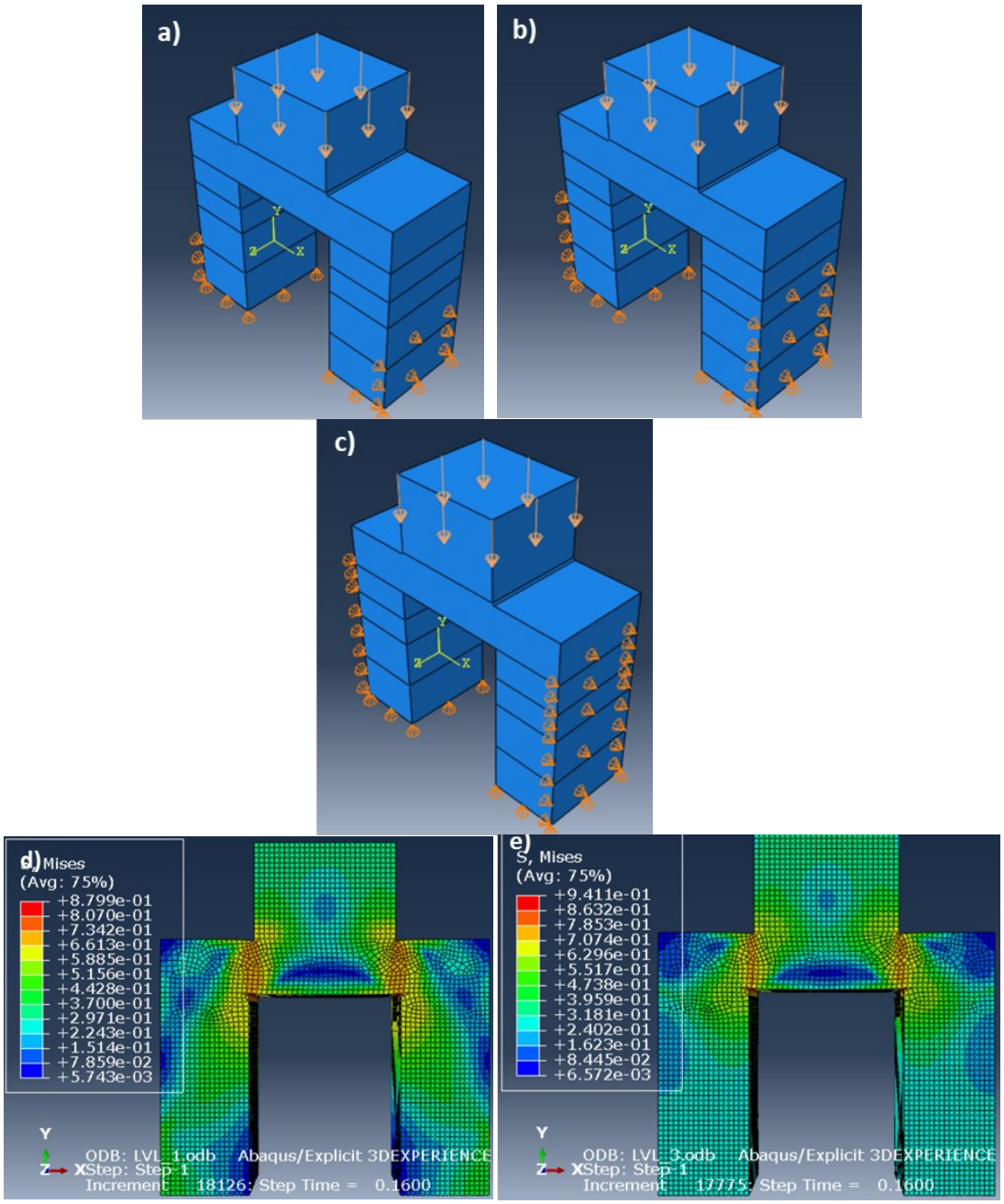

Figure 8.5 *(a-c) Brim movement constrain applied at different altitudes of the brims; (d) von mises stress distribution on the modified flat hat specimen with movement restriction from a); (e) von mises stress distribution on the modified flat hat specimen with c) movement restriction. Stresses in e) are more localized in the shear area and reach higher values compared with those from d).*

The length of the brims was reduced from 10 mm to 5 mm (Figure 8.6) to decrease the risk of splitting of the brims and material consumption. This modification kept a similar distribution of the stresses and strains at the gage section compared to Figure 8.5.

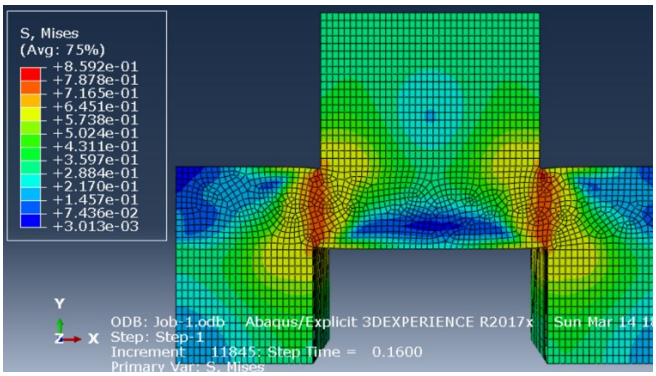

Figure 8.6 *Von mises stress distribution of the modified flat-hat specimen with reduced length of the brims.*

The width of the brims and the head were increased from 3.5 mm and 5.4 mm (Figure 8.7-a) to 5 mm and 7 mm (Figure 8.7-b) or 5 mm and 8 mm (Figure 8.7-c) respectively. The width of the gage section remains constant. These changes did not improve the stress concentration when compared with the previous Figure, so they were not applied.

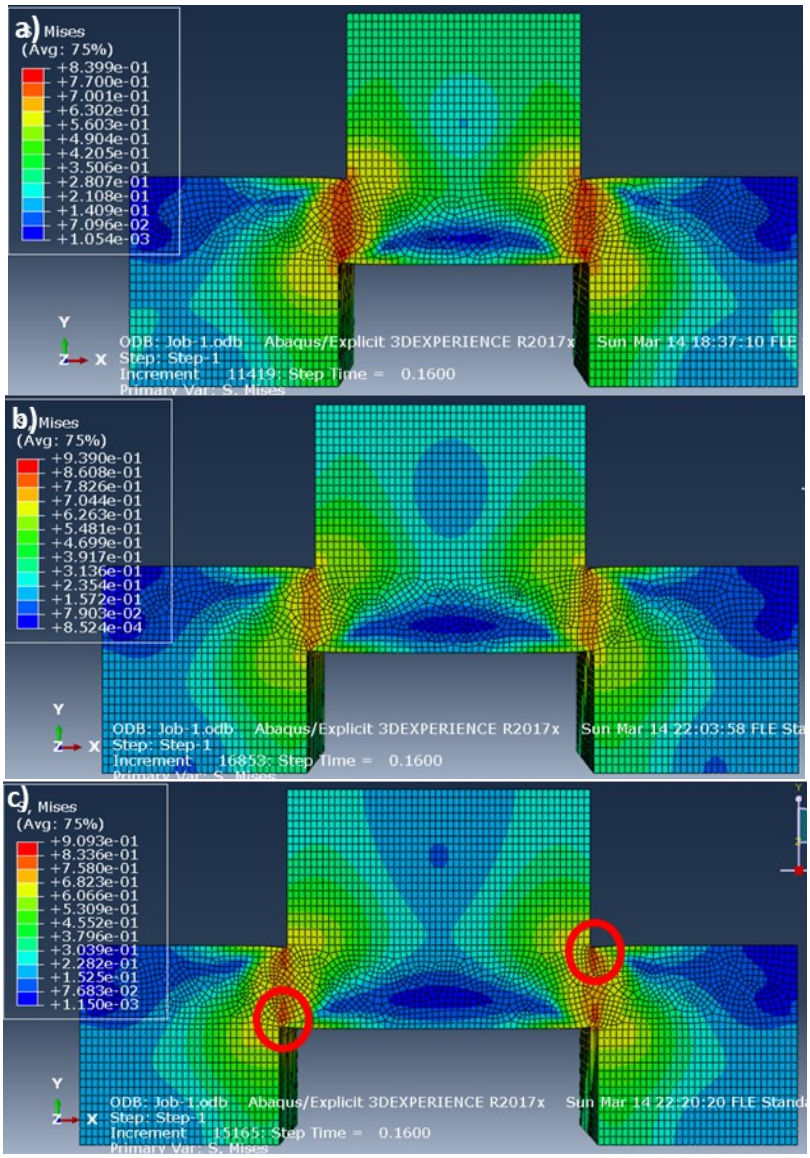

Figure 8.7 *Von mises stress distribution of the modified flat-hat model with shorter and thicker brims and a) 5.4 mm head width, (b) 7 mm head width, and (c) 8 mm head width. Notice that in the last model, stresses are more concentrated at the corners rather than inside the shear area; the specimen could fail by a design error.*

Figure 8.8 shows that further reductions in the length of the head did not alter the stress state.

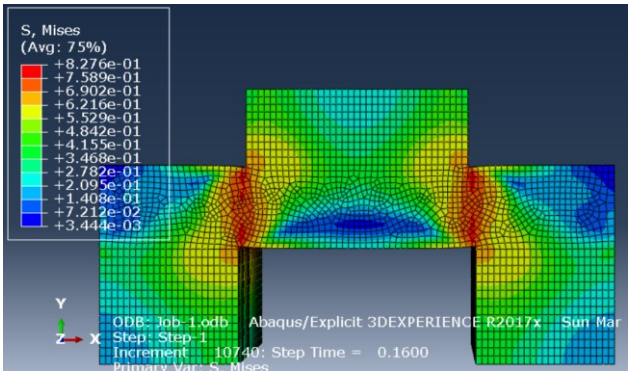

Figure 8.8 *Von mises stress distribution of the modified flat-hat model with shorter brims and head.*

For the physical experiment, limiting the splitting of the brims required using a holder that imitated the boundary conditions described in the simulations. An example would be the plate-shear holder from Figure 4.8 a). However, that holder does not allow the direct observation of the shear area while performing the test. Figure 8.9 shows an alternative design for the holder made of steel.

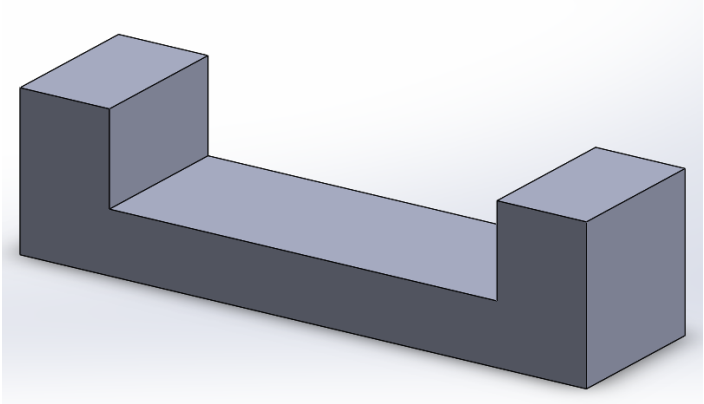

Figure 8.9 *Representation of the holder.*

The addition of the holder led to the redefinition of the model. An additional part made of steel (density: 7800 kg/m3, Young's modulus: 210 GPa, Poisson's ratio: 0.3) was created assuming it remained elastic during the simulation. The specimen was fitted in the holder using the assembly module; and the contact (frictionless) between the brims and the holder were defined in the interaction module. Based on the contact assumptions of the software described in Software assumptions, the region of the holder in contact with the flat-hat was chosen as master (first) surface; while the surface of the flat-hat in contact with the holder was the slave surface as it is made of a softer material. Consequently, the mesh size of the holder was larger than the mesh size of the brims. To reduce the total number of elements in the model, irregular cell partitions were created close to the contact region as seen in Figure 8.10 a). Figure 8.10 b) shows that the boundary conditions previously applied around the brims are now applied to the surface of the holder in contact with the output bar.

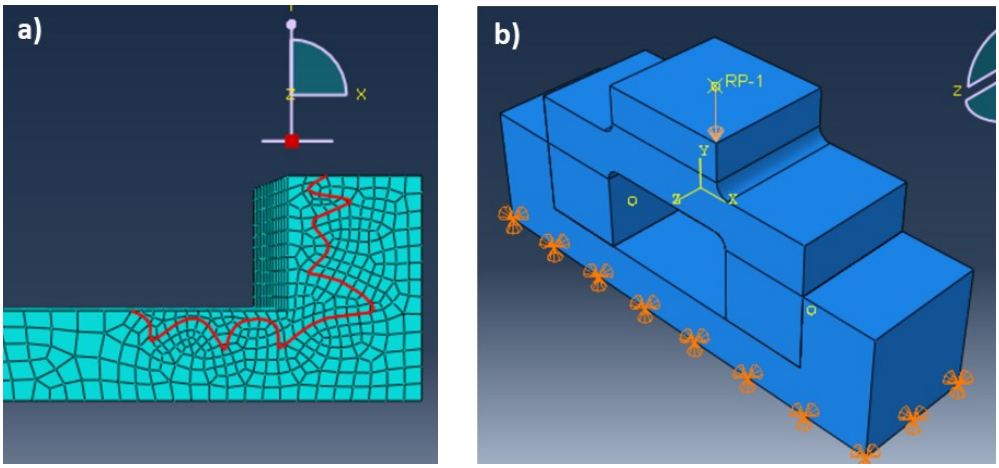

Figure 8.10 (a) *Mesh distribution in the holder, focused on the region in contact with the specimen; (b) Boundary conditions applied to the model.*

The last adjustments concern the fillets of the gage section and the dimensions of the gage section itself. Originally, Budiwantoro et al. [98] recommended having a shear angle of 5° to obtain the most reliable results. However, the width of the Shear (in tension) gage section could not be milled down to 0.5 mm to obtain such angle due to the available tooling (0.7 mm diameter drill); and increasing the length of the gage section did not provide the desired stress state according to the simulations (Figure 8.1-c). Therefore, the width of Shear (in compression) gage section was increased from 0.2 mm to 0.4 mm. This modification increased the velocity necessary at the interface for generating the same shear strain rate (2800 s^{-1}). Table 11 shows the final dimensions of both Shear (in tension) and Shear (in compression) geometries, where the shear angle is approximately 11° in both specimens; this allows performing a comparative study of ASB formation between both alloys and designs. Finally, increasing the radius of the fillets from 0.1 mm (Figure 8.11-a) to 0.5 mm (Figure 8.11-b) eased sample manufacturing and reduced the possibilities of failing due to a design error as the stress concentration there decreased. Figure 8.11 c) and d) exemplify how the specimens should be machined with respect the available plate. Specimen designs contains the final design and dimensions of the geometry.

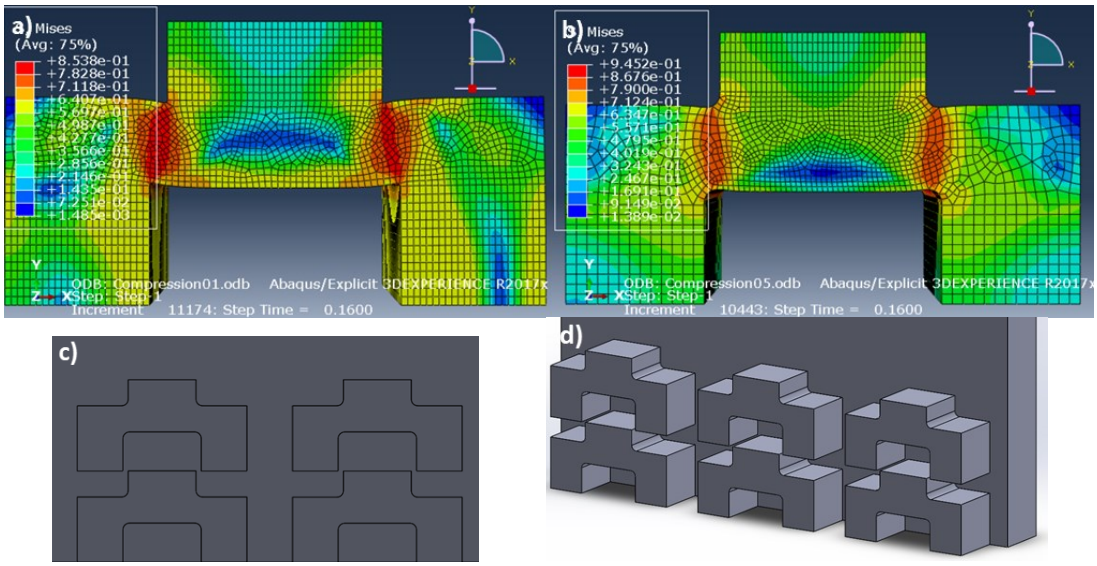

Figure 8.11 *(a) Von mises stress map in the shea-compression specimen with wider gage and 0.1 mm radius fillet; (b) Von mises stress map in the shea-compression specimen with wider gage and 0.5 mm radius fillet; (c-d) disposal of the specimens for their machining.*

8.2 Comparison of DIC and Abaqus results

This section compares the displacement and strain developed in the geometries during the simulations and the experiments.

8.2.1 Shear (in compression) samples

Figure 8.12, Figure 8.13 and Figure 8.14 present the DIC displacement and strain measurements of Shear (in compression) sample 5, one of the samples with the most interesting fracture case, which broke into two pieces (see Figure 7.18).

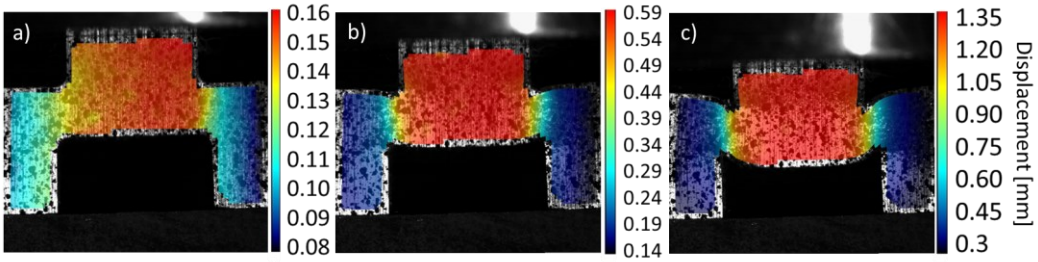

Figure 8.12 *DIC displacement measurements of the head of sample 5 (strain rate: 11000 s^{-1}) at different moments during the test.*

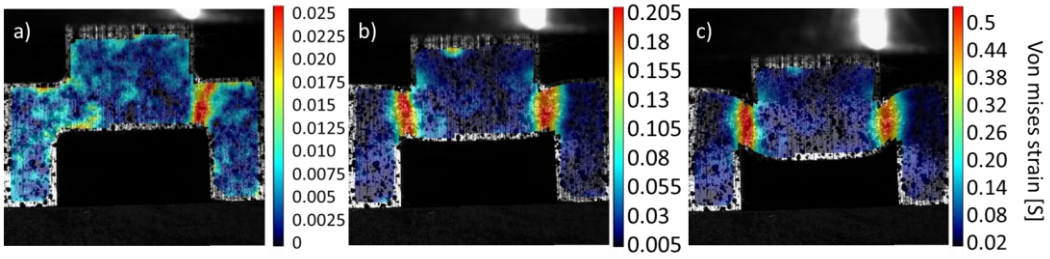

Figure 8.13 *DIC Von mises strain distribution of sample 5 at different moments during the test.*

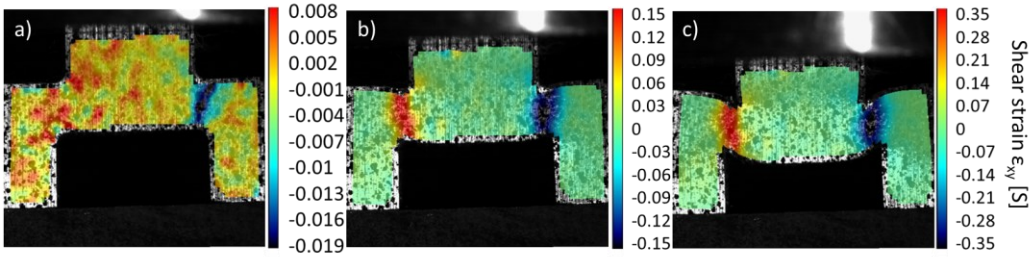

Figure 8.14 *DIC engineering shear strain (ε_{xy}) component of sample 5 at different moments during the test.*

In the beginning of the tests (image-a from the mentioned figures) the displacement (or strain) values were higher around the right gage section than the displacement (or strain) at the left gage section. A possible reason can be that the sample did not fit properly into the holder, caused by milling one of the contacting surfaces (brim-holder) more than the other.

By the midpoint and end of the test, the displacement (strain) distribution were almost symmetric (or antisymmetric in Figure 8.14), meaning that both gage sections deformed similarly. Most of the strain was concentrated at the gage section; however, its distribution was not homogenous and a considerable fraction of the strain spread out of the gage section. This phenomenon of complex strain-distribution along the gage section occurs in other flat-hat designs or models without milled shear-gage. [96], [103], [154]

Regarding sample 1, Figure 8.15 show a symmetric (antisymmetric for Figure 8.16) distribution of the strain on the surface of the specimen, meaning that both gage sections deformed similarly. The strain values were almost the same as those from sample 5, although the displacement of the head measured by the DIC system was different. The displacement of the head of the specimen was calculated by subtracting the lowest values of displacement (at the brims of the sample) from the highest values of displacement (attributed to the head of the sample) measured in the image gathered before the sample failed. Table 16 shows the values of such displacement and compares them with the displacement registered by the UTM and the SHPB at the end of the

experiments. The difference in the measurement of the displacement between the DIC system and the SHPB is considerably lower than between the DIC system and the UTM.

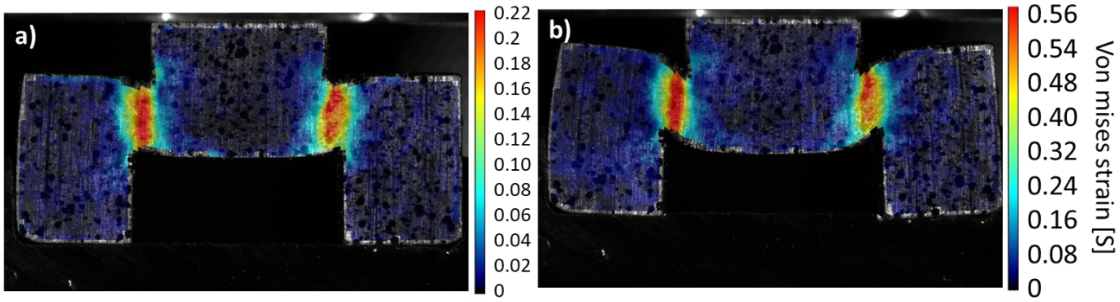

Figure 8.15 *DIC Von mises strain distribution of sample 1 at different moments during the test.*

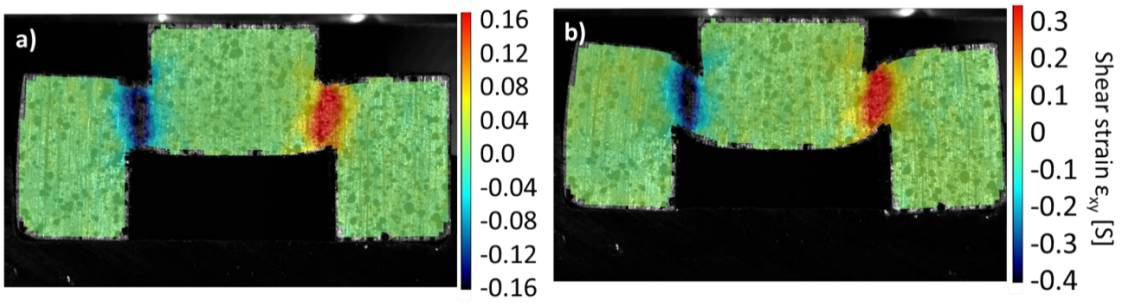

Figure 8.16 *DIC engineering shear strain (ε_{xy}) component of sample 1 at different moments during the test.*

Table 16 *Displacement measurements of Shear (in compression) samples 1 and 5 at the end of the experiments.*

	Device	Displacement (mm)
Sample 1	Universal testing machine	1.9
	DIC system (quasi-static)	1.3
Sample 5	SHPB	0.95
	DIC system (dynamic)	1.05

A possible reason for the considerable difference in the displacement measurements between the UTM and the DIC system could be related to the patterned surface of the samples. Figure 8.17 shows that sample 1 has a pattern with less black dots than sample 5, especially at the gage section; additionally, some of those dots have a size half the width of the gage section, hindering the displacement (and strain) measurements.

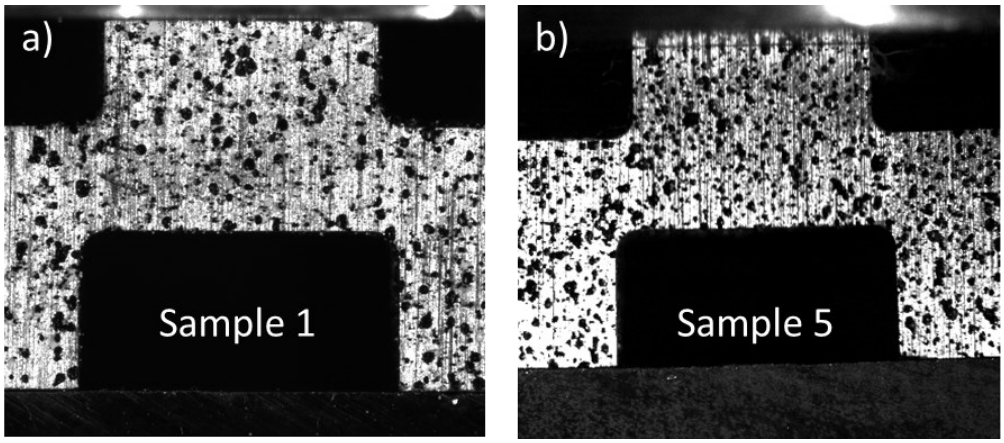

Figure 8.17 *Close-up to the patterned surfaces of Shear (in compression) sample (a) 1, and (b) 5.*

When comparing the DIC measurements to the simulated models, in both cases the samples deformed similarly. Figure 8.18 shows the distribution of strains at different times of the simulation; strains concentrated first at the fillets and advanced towards the centre of the gage section, forming almost a vertical band (the shear angle was approx. 11°). The distribution of strains was not uniform either and spread out of the gage section. This spreading-out phenomenon is more accentuated for the stress fields, as show in Figure 8.19 b). Figure 8.19 a) shows that the equivalent plastic strain (PEEQ) distribution was not uniform across the thickness of the geometry and that the holder did not deform.

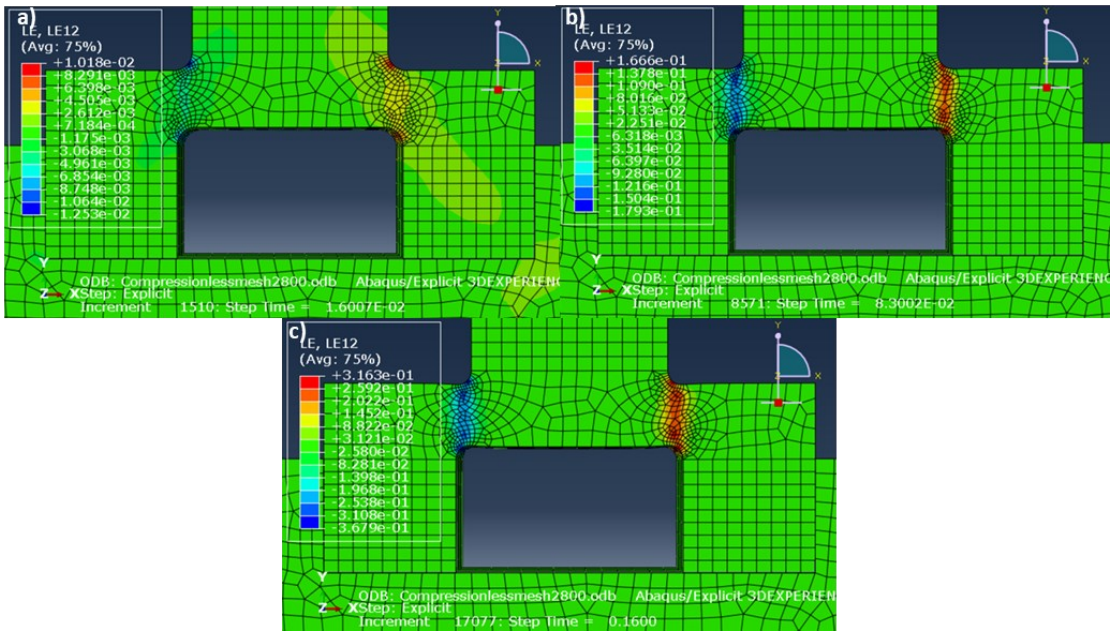

Figure 8.18 *Logarithmic shear strain component (ε_{xy}) of the high strain-rate (2800 s^{-1}) simulated specimen.*

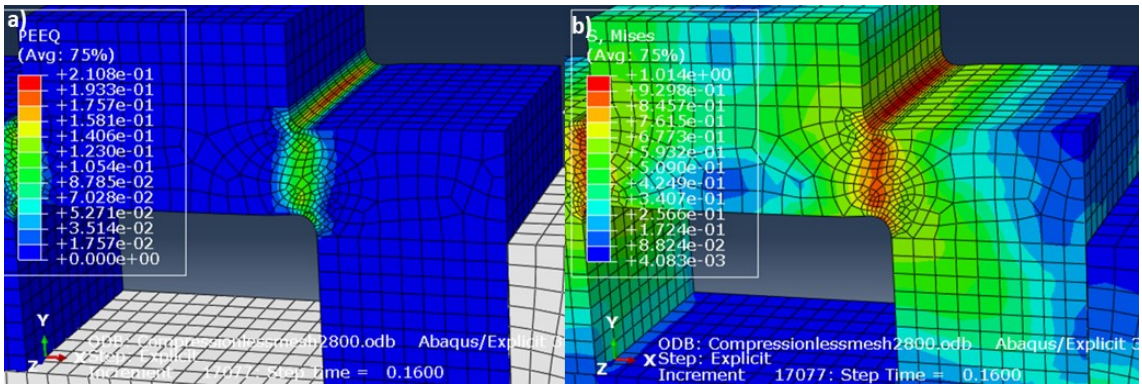

Figure 8.19 *(a) Equivalent plastic strain (PEEQ) and (b) Von Mises stress field across the thickness of the simulated sample under dynamic loading.*

8.2.2 Shear (in tension) samples

Table 17 shows the DIC displacement measurements of the gage section of the Shear (in tension) geometry and compares them with the displacements gathered by the UTM and SHTB at the end of the experiments. The difference between displacement measurements at a same loading condition is lower than those for Shear (in compression) samples.

Table 17 *Displacement measurements of Shear (in tension) samples 1 and 5 at the end of the experiments.*

	Device	Displacement (mm)
Sample 5	Universal testing machine	2.35
	DIC camera (quasi-static)	2.4
Sample 1	SHTB	1.6
	DIC camera (dynamic)	1.65

Sample 5 deformed at the same strain rate (0.1 s^{-1}) in both the experiment and the simulation, so a comparison of the strain distribution can be done.

Figure 8.20 shows how the strain concentrates in both cases at the gage section, starting first at the corners opposite to the fillets and developing a diagonal band afterwards. Figure 8.20 c) highlights a little distortion in the corner of elastic part next to the gage section caused by the heavy distortion of the elements adjacent to the gage section, as element elimination (fracture mode) was not included in the model. Figure 8.21 shows the homogenous stress and strain fields across the thickness of the model, as opposed to the Shear (in compression) geometry.

Figure 8.20 and Figure 8.22 show the Von Mises strain (PEEQ in Abaqus [124]) and the shear strain component in logarithmic scale from the DIC and the simulated models, which are in good agreement. However, the existing difference in maximum local strains can be attributed to the difference in element size from each mesh and its distribution within the gage section.

To minimize the difference in element size between the models and the DIC patterns, Ghadbeigi H. et al. [155] developed a DIC pattern for microstructural SEM-DIC measurements that could be extrapolated to millimetre-scale optical measurements. The pattern consists of laying a squared microgrid on the surface of the etched specimen using Electron Beam Lithography technique. [155]

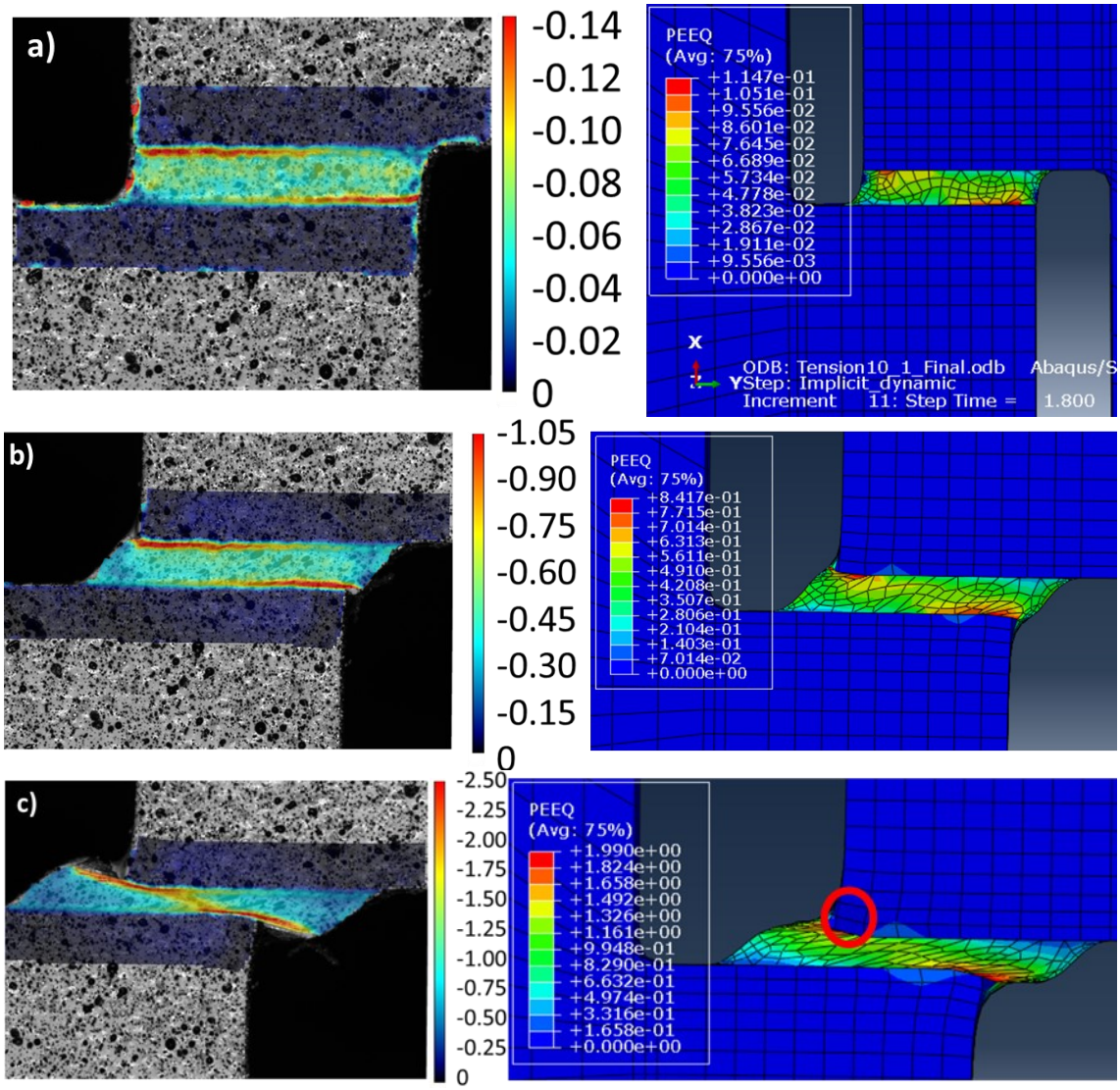

Figure 8.20 *Von mises strain distribution at the gage section of the Shear (in tension) sample (left, DIC; right, simulated) tested under quasi-static loading (a) at the beginning of the test, (b) at the midpoint and (c) at the last frame before failure.*

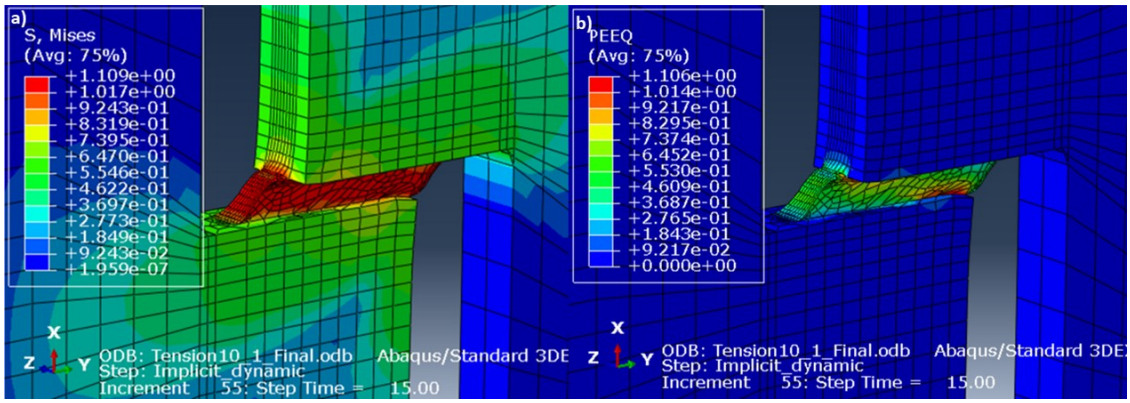

Figure 8.21 *(a) Von Mises stress and (b) Von Mises strain/Equivalent plastic strain (PEEQ) field across the thickness of the simulated sample under quasi-static loading.*

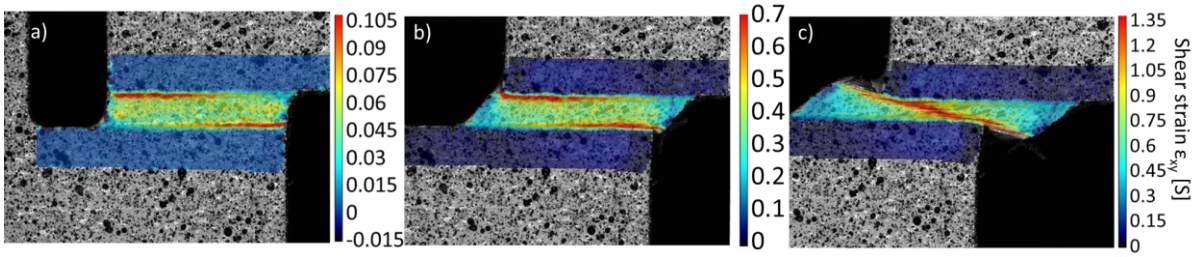

Figure 8.22 *DIC measurement of sample 5 engineering shear strain (ε_{xy}) component at different moments during the test.*

8.3 Stress – strain curves

After gathering and treating the experimental data for better readability (in the case of the SHB, “smoothening” functions were needed), the material response was analyzed and compared with the literature, followed by an analysis of the stress-strain curves from the simulated models.

The shear stress – shear strain curves of Cantor Shear (in tension) samples 4 and 5 from Figure 8.23 show that increasing the strain rate increases the strain hardening ability. This chance in the shape of the curves within the strain rate is in concordance with Figure 2.3 description of temperature and strain rate effect on fcc metals. Meyers et al. [75] tested Cantor alloy at a shear-strain rate of 1800 s^{-1}, yielding at 250 MPa. In this thesis, samples under quasi-static loading yielded at around 230 MPa and strain hardened continuously until fracture. Samples tested under higher dynamic loading yielded at 290 MPa approximately and strain hardened continuously until approximately a shear strain of 1.25, where the flow stress decreased until failure occurs. The fact that yielding does not increase in the later samples would lead to consider that the Cantor HEA lacks continuous absorption of impact energy, making this alloy not suitable for impact applications or have certain restrictions in this application area. However, Tsai et al. [156] demonstrated that as strain rate increases (tested up to 9000 s^{-1}), yield stress and strain hardening rate increases significantly. Considering that the sample design

was tested at a strain rate of 2000 s^{-1} (for an Al alloy) and the lowest experimental data available for the Cantor HEA is from a strain rate of 5000 s^{-1}, more tests should be performed between the mentioned strain rates to study the possible reasons of this lack of agreement with Tsai et al. [156] study.

According to Meyers [75], thermal softening overcame strain hardening at a shear strain of 7, leading to shear localization and ASB formation; this was confirmed via Staker's expression [78], which requires a detailed examination of the thermal softening effect. For this reason, to prove that the decrease in the flow stress of samples tested in dynamic loading conditions was caused by thermal softening overcoming strain hardening, performing temperature measurements and studying the thermal softening effect would be necessary.

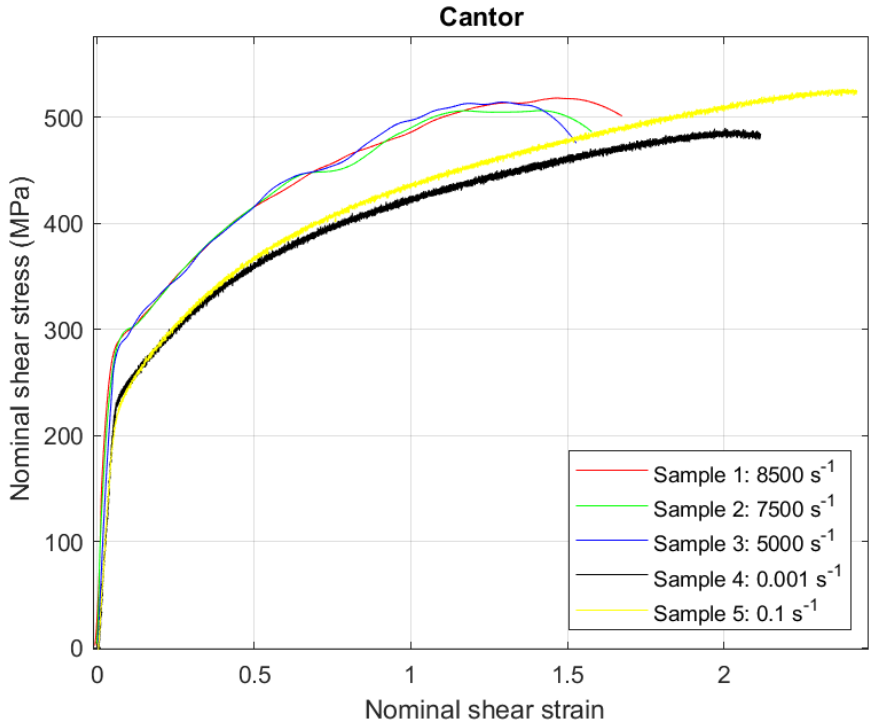

Figure 8.23 *Nominal shear stress-strain curve of the Shear (in tension) samples.*

Regarding $Al_{0.3}$CoCrFeNi HEA, Figure 8.24 shows that the Shear (in compression) curves strain harden continuously until fracture and those samples tested under the same loading conditions have great repeatability. The Shear (in compression) geometry allows the material to deform more than the Shear (in tension) geometry under quasi-static loading conditions, similarly to the preliminary flat-hat design [96].

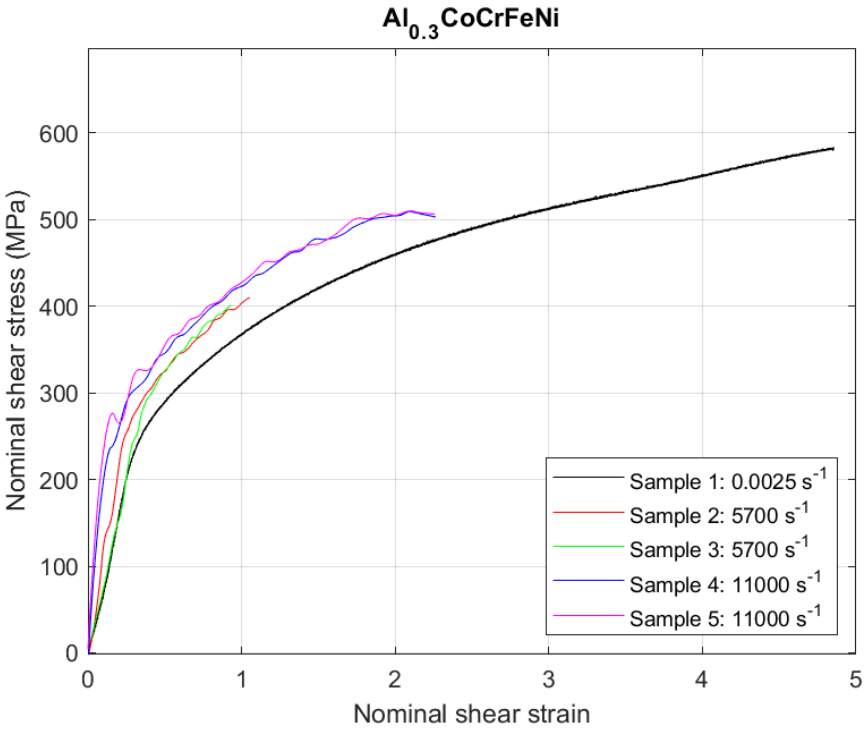

Figure 8.24 *Nominal shear stress-strain curve for the Shear (in compression) samples.*

It is worth to mention that the Shear (in compression) samples 1, 2 and 3, which ended stuck in the holder after the experiment, do not have a clear linear regime. Figure 8.25 shows in more detail this phenomenon.

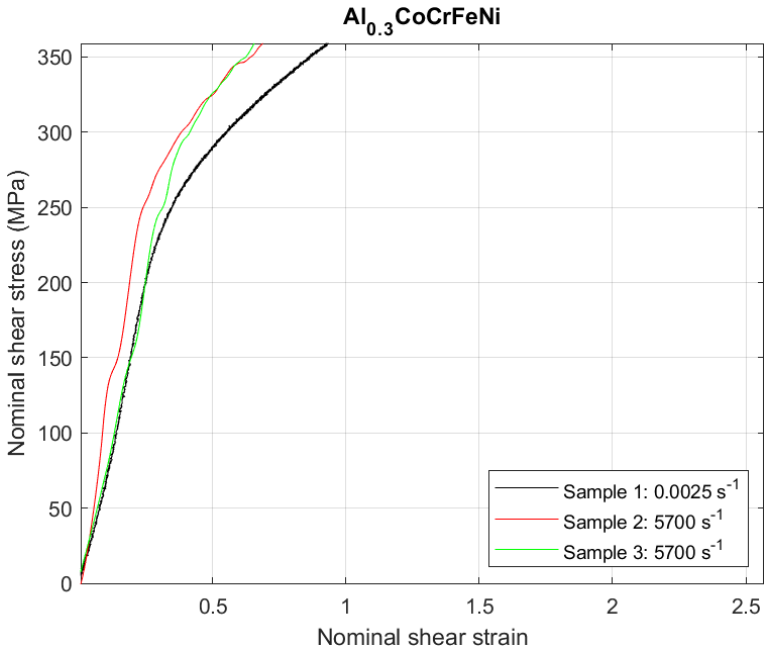

Figure 8.25 *Close-up to the elastic regime of the shear stress-strain curves for the Shear (in tension) samples.*

The shape of the $Al_{0.3}$CoCrFeNi curves changes slightly with increasing the strain rate, and so does the yielding points. Under quasi-static loading, $Al_{0.3}$CoCrFeNi yields at 250 MPa; while under dynamic loading the material yields at approximately 270 MPa and 300 MPa for the strain rates of 5700s^{-1} and 11000s^{-1} respectively. Samples 1 (strain rate: 0.0025s^{-1}), 2 and 3 (strain rate: 5700s^{-1}) strain hardened continuously, while samples 4 and 5 (strain rate (11000 s^{-1}) seem to soften at a shear strain of 2. However, performing temperature measurements and study the thermal softening effect is again necessary to verify Staker's expression [78] and that thermal softening overcame strain hardening effect.

Alloying CoCrFeNi with Al instead of Mn should lead to higher strain hardening rates due to the larger lattice distortion and SFE of Al compared with Mn [74], [75], [157]. However, the strain hardening of $Al_{0.3}$CoCrFeNi is not as big as in literature (Figure 8.26) nor higher than the tested Cantor alloy as in Figure 8.26. For the same shear strain, Cantor alloy has larger flow shear stress values. [75]

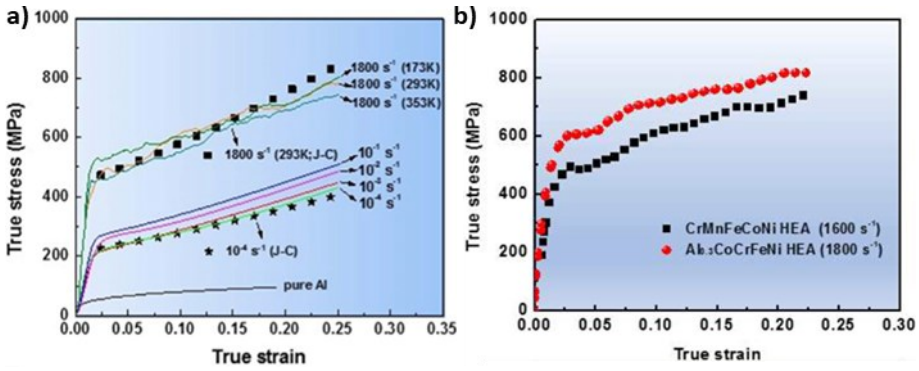

Figure 8.26 *(a) Mechanical response of Cantor alloy and $Al_{0.3}$CoCrFeNi HEAs under high strain rates* [74]*; (b) true stress-strain curve of $Al_{0.3}$CoCrFeNi HEA at different strain rates (with Johnson-Cook model fitting curves).* [75]

To conclude the analysis of the experimental shear stress-strain curves, the strain-rate sensitivity factor "m" (defined by $\frac{\partial \log(\sigma_y)}{\partial \log(\dot{\varepsilon})}$) was calculated for the $Al_{0.3}$CoCrFe HEA. First, the shear stress-strain curves were converted to effective shear stress-strain curves, applying Von Mises criterion. With the yield strength values from those curves, strain-rate sensitivity curve was elaborated, from which the slope "m" was extracted [103]. Figure 8.27 compares the strain-rate sensitivity curve obtained from the tests with that from the Li et al. research [74]. The low value of the experimental strain-rate sensitivity factor (0.015), compared with that from Li et al. research (0.052) [74]**,** is caused by the elevated yield strength obtained in the low strain rate tests. More tests should be done at low strain rate to study the lack of agreement with respect the strain-rate sensitivity factor.

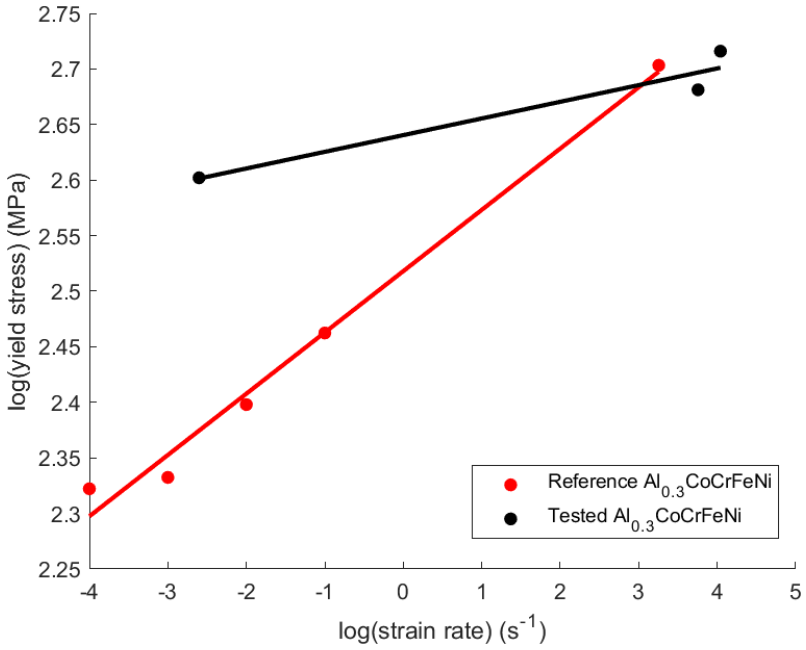

Figure 8.27 *Strain rate sensitivity curve, compared with Li et al.* [74] research.

Finally, regarding the shear stress-strain curves from the simulated models, the reaction forces from the reference point (SHPB geometry) or the cutting surface (SHTB geometry) were obtained together with the displacement in the y-axis of the nodes of the regions where the load was applied. Figure 8.28 shows the resultant shear stress – shear strain curve from applying Equations 36 and 37 and the dimensions of the gage section from Table 10 to the force – displacement data.

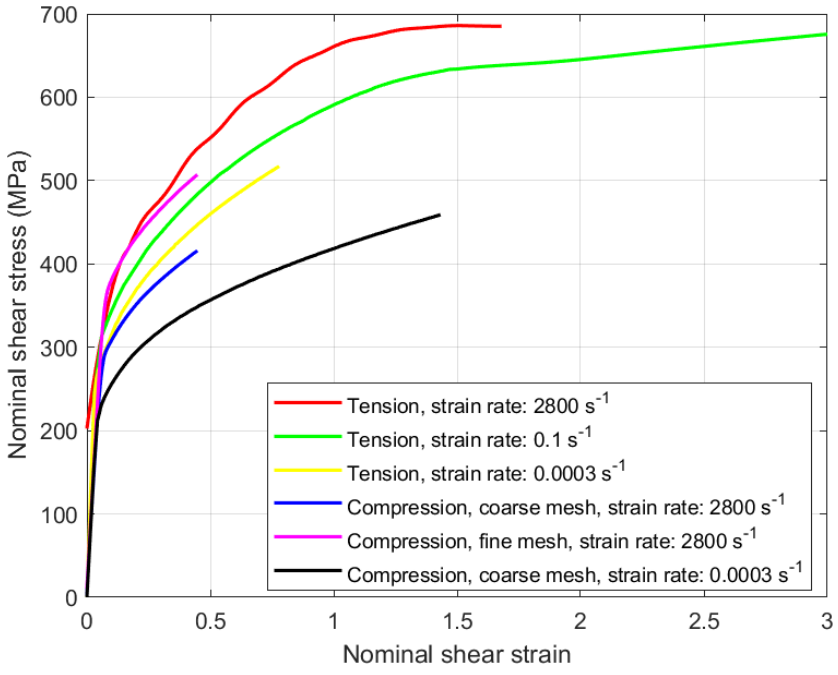

Figure 8.28 *Nominal shear stress-strain curves of the simulated models.*

All the models are shown together because their strain rates were not the same as the experimental ones, except for the Shear (in tension) geometry subjected to a strain rate of 0.1 s^{-1}. In the Shear (in tension) geometry subjected to a strain rate of 0.1 s^{-1}, the shear stress values differed from the experimental ones. A possible cause for such difference can be the use of only eight data points from a monotonic compression tests as input data instead of using a fitting model such as Johnson-Cook, limiting the accuracy of the model, especially when simulations reach the last value from the input tables [75], [158]. Also, the available data for all the simulations was for Cantor alloy only, so the compression curves from the simulated models could not be compared with the compression curves from the experiments, as the materials were different.

As explained in Software assumptions, Abaqus considers the true stress-strain data as suitable for both tension and compression simulations. However, Figure 8.28 shows that even if the two geometries are subjected to the same strain rate, each model responds differently. This can be related with the difference in mesh size and stress state developed in each geometry. To test if the simulations are affected by the mesh size, an additional simulation was carried for the Shear (in compression) design under dynamic loading. “Compression, coarse mesh” simulation has 10046 elements, and its calculation took approximately five minutes; while “Compression, fine mesh” has 153979 elements, and took more than three hours to reach the solution. The simulation with the fine mesh has a shear stress – shear strain curve similar to that of the Shear (in tension) geometry, but still differs due to the different stress state developed in each geometry.

9. CONCLUSION

The materials studied in this thesis were two HEAs, Cantor and Al-Cantor, great candidates for applications that involve machining, punching, perforation, shear operations and armours, where ASB formation limits the operating conditions of the components. However, shear properties and ASB formation in these alloys has been barely studied. For this reason, different shear geometries able to allow direct analysis of ASB formation were studied via FEM modelling (Abaqus Software) and tested under quasi-static (servo-hydraulic testing machine) and dynamic (SHPB and SHTB) loadings. Physical tests were coupled with DIC tools for analysing strain field evolution in the gage section. The aim of the thesis is to study the performance of specific geometries and compare their simulated and experimental results with the literature.

Shear (in tension) geometry is based on the design of Gardner et al. [104] for shear characterization of metal sheets, used in this thesis or the characterization of the Cantor HEA. There is a good correlation between the DIC measurements and the simulated results, but with a slight discrepancy in the maximum local strains due to the different element mesh sizes. The strain field was uniform across the thickness of the gage section and the shear stresses and strain concentrated at the gage section developing a diagonal band. The material response was not fully in concordance with the literature values [10], [74], [75], [156] as the curves were the same for the different dynamic loading experiments (5000 s^{-1}, 7500 s^{-1} and 8500 s^{-1}) and no increase in the yield stress or strain hardening rate was observed when increasing the strain rate. Therefore, physical tests at lower dynamic loadings coupled with infrared thermography should be performed to verify if the softening of the high-strain rate curves is caused by design limitations or if it is because thermal softening overcame strain hardening. In the latter case, Staker's expression for a critical shear strain for shear localization should be considered [78].

Shear (in compression) geometry is based in the flat hat design [98] to test $Al_{0.3}CoCrFeNi$ HEA, with some modifications for easing the manufacturing of the samples. Instead of restricting the movement of the brims by connecting them with more material underneath, a steel U-shape holder avoided the splitting of the brims. The resultant two-piece specimen presented some issues that were not envisaged during its design. Symmetric strain fields at the gage sections were registered by the DIC software, but its values were not reliable as the displacement of the head of the specimen was not properly measured and gage section did not contain a patterned surface small enough. Shear strains concentrated at the gage section but not uniformly. Indeed, from the simulations was

observed that the shear strains were not uniformly distributed across the thickness of the sample. As a result, the stress state at the gage section deviated from simple shear stress state. Very high shear-strain values were achieved when tested under quasi-static loading; but under dynamic loading, the value of shear-strain failure of the Shear (in compression) samples is similar to the Shear (in tension) samples. The flow shear-stress values of the tested $Al_{0.3}$CoCrFeNi were lower than those values of the tested Cantor HEA, which is contrary to the great strain hardening ability and elevated resistance to shear localization expected from the literature [74], [75], [157]. Therefore, the shear stress-strain curves obtained from this geometry offer a great contrast with respect other geometries used to test the $Al_{0.3}$CoCrFeNi HEA, as it occurred with the preliminary flat-hat design used for testing other materials [96]. A double shear specimen with the gage sections milled down, resembling the concept developed for the Shear (in tension) geometry, would be recommended instead [154]. This Shear (in compression) design allows measuring directly temperature rises, deformation and failure processes as well as gathering reliable data of the dynamic properties of materials up to strain rates of $10^5 s^{-1}$ [101], [154]. The manufacturing complexity of this geometry is higher than that of the design used in this investigation, but the stress state is closer to the ideal simple shear one, the design promotes ASB generation and their shear stress-strain curves can be used for studying the response of the material.

Abaqus FE tool was used for testing and analysing the specimens, strengthening their designs, reducing the number of physical tests needed and prototyping costs. The field outputs from the simulated models were in good agreement with the strain fields distribution and concentration calculated by the 2D-DIC system. Additionally, it complements this analysis technique by offering the stress and strain fields throughout the thickness of the component. However, the stress values from the simulated stress-strain curves depend on element mesh size at the region of interest and the input data used for the calculations. Further investigations should include mesh sensitivity analysis [22] and using fitting models such as Johnson-Cook's [4], [75], [158] one for introducing input data to improve the agreement between physical experiments and simulated models.

10. ANNEX

This annex includes a guide of how to build a Rittel specimen in Abaqus and the sketches of the final designs of the geometries manufactured.

10.1 Rittel's specimen

To sketch Rittel's specimen, start creating a 3D solid, deformable for revolution; then draw a rectangle and apply 90° angle revolution. Sketch a planar partition on the tap of the specimen as in Figure 10.1 a). Extend the partition by creating a cutting plane as in Figure 10.1 b). Duplicate the actual specimen using the "mirror" tool on the surface showed in Figure 10.1 c).

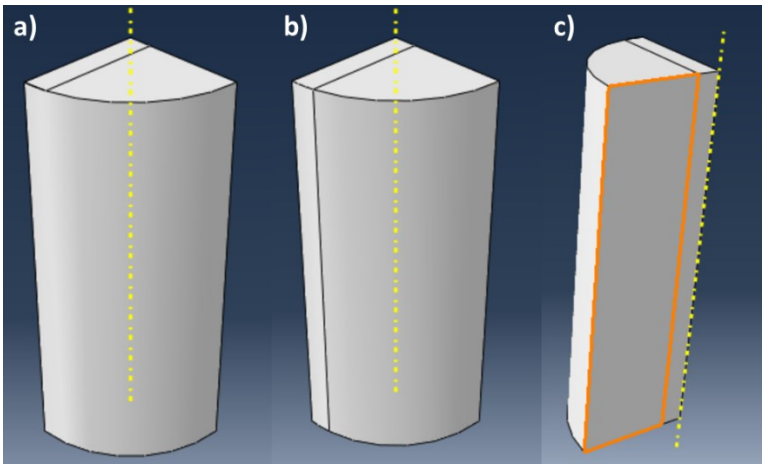

Figure 10.1 *Rittel's specimen sketch: 90° revolution rectangle operations.*

Select the surface of the cutting plane facing the curved part of the section of the cylinder as in Figure 10.2 a) to extrude material. Define the shape of the extrusion and its direction as in Figure 10.2 b) and c).

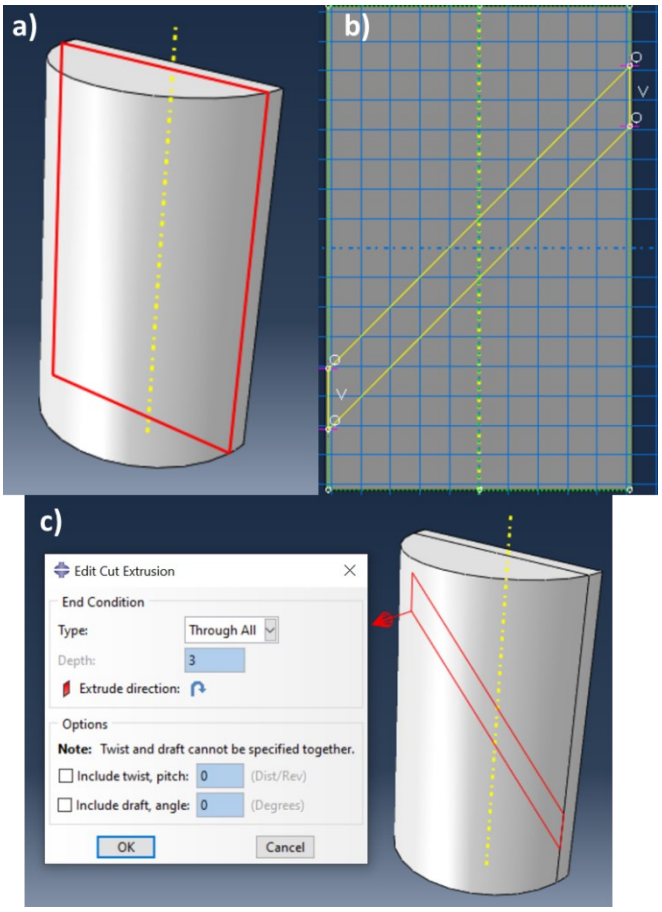

Figure 10.2 *Rittel's specimen sketch: extrusion operations.*

Finally, duplicate the specimen applying “mirror” tool on the surface from Figure 10.3 a).

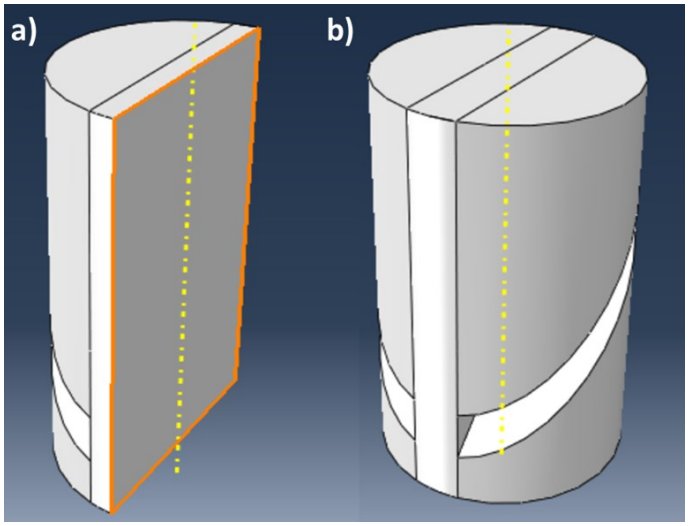

Figure 10.3 *Rittel's specimen sketch: final operation and resulting model.*

10.2 Specimen designs

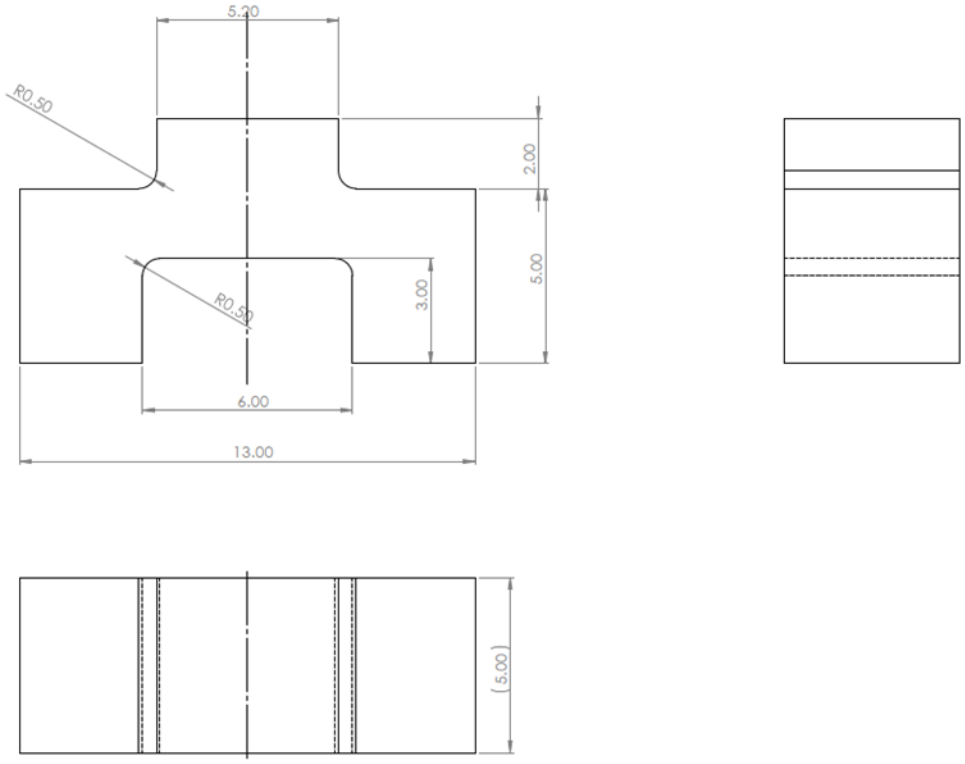

Figure 10.4 *Modified flat-hat sketch. Tolerances according to ISO-2768 fine.*

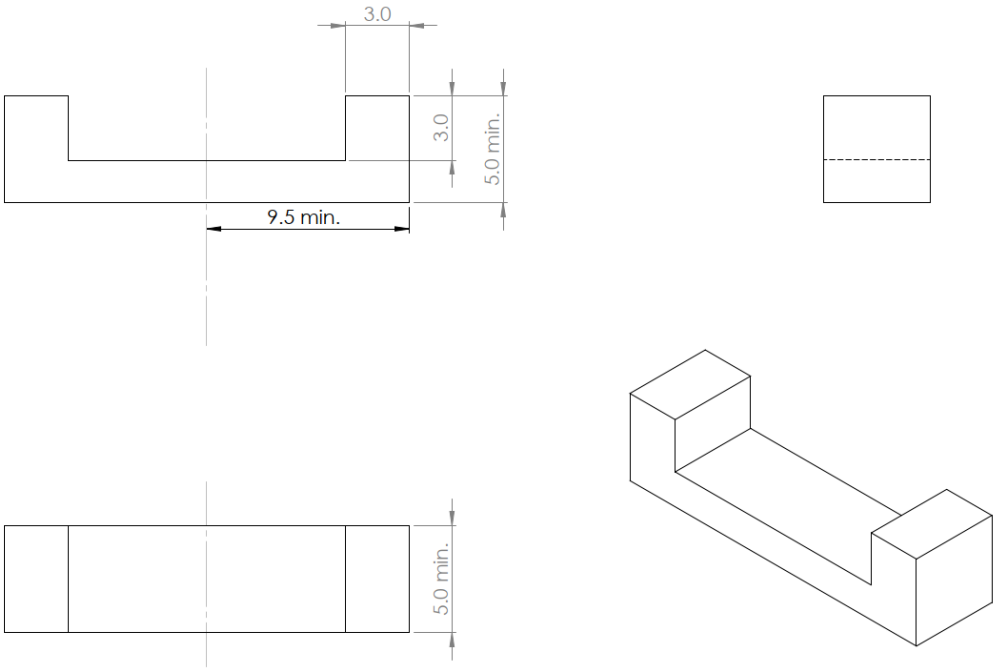

Figure 10.5 *Sketch of the holder.*

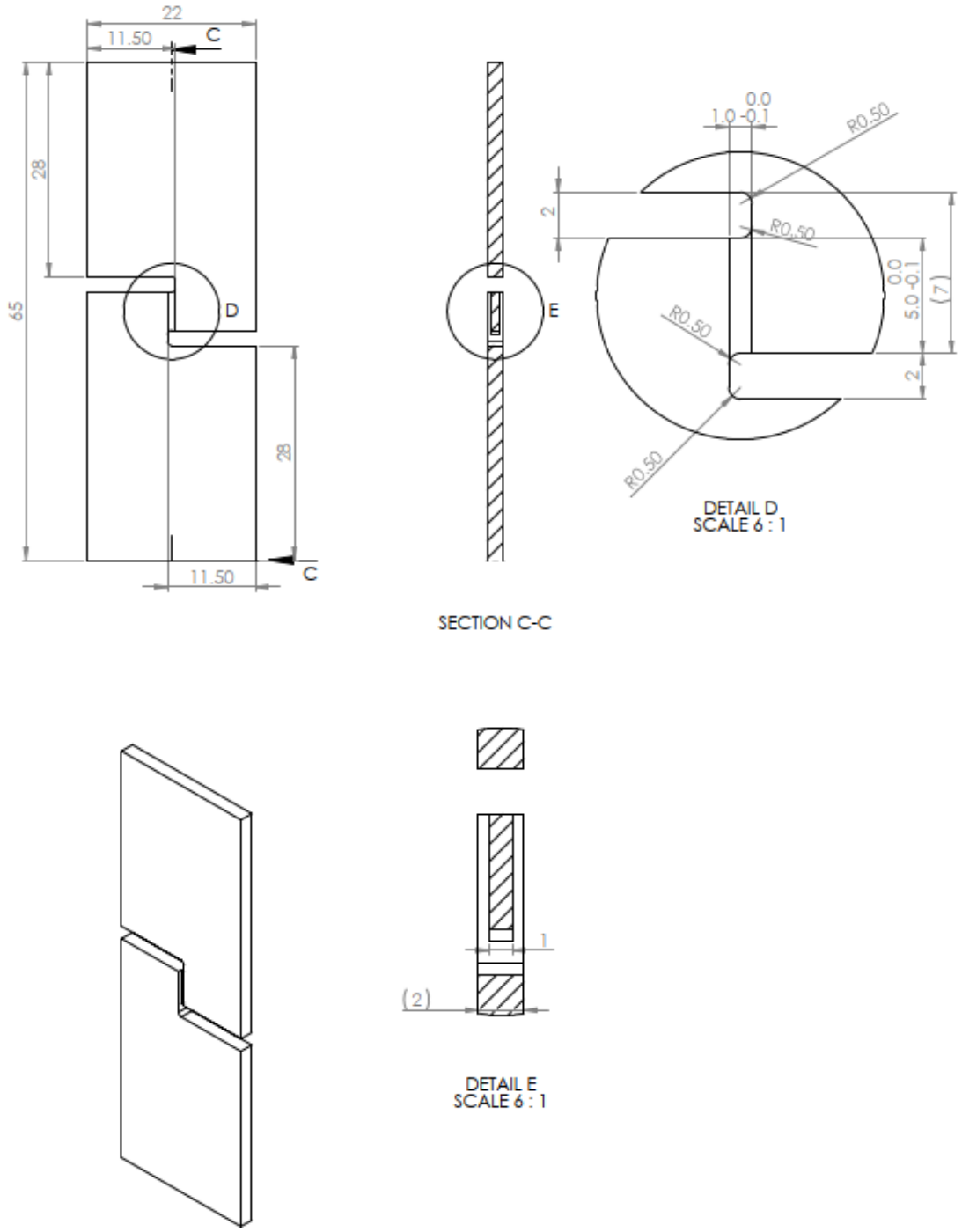

Figure 10.6 *Sketch of the Shear (in tension) specimen. Tolerance ISO-2768 fine for Detail D section and ISO-2768 for the rest.*

11. REFERENCES

[1] J. W. Yeh *et al.*, Nanostructured high-entropy alloys with multiple principal elements: Novel alloy design concepts and outcomes, *Advanced Engineering Materials*, vol. 6, no. 5, 2004, doi: 10.1002/adem.200300567.

[2] B. Cantor, I. T. H. Chang, P. Knight, and A. J. B. Vincent, Microstructural development in equiatomic multicomponent alloys, *Materials Science and Engineering A*, vol. 375–377, no. 1-2 SPEC. ISS., 2004, doi: 10.1016/j.msea.2003.10.257.

[3] M. C. Gao, P. K. Liaw, J. W. Yeh, and Y. Zhang, *High-entropy alloys: Fundamentals and applications*. 2016. doi: 10.1007/978-3-319-27013-5.

[4] G. C. Soares, M. Patnamsetty, P. Peura, and M. Hokka, Effects of Adiabatic Heating and Strain Rate on the Dynamic Response of a CoCrFeMnNi High-Entropy Alloy, *Journal of Dynamic Behavior of Materials*, vol. 5, no. 3, 2019, doi: 10.1007/s40870-019-00215-w.

[5] Kettunen P.O. and Kuokkala V.-T., Plastic Deformation and Strain Hardening, *Materials Science Foundations*, vol. 16–18, 2003.

[6] S. Nemat-Nasser, W. G. Guo, and J. Y. Cheng, Mechanical properties and deformation mechanisms of a commercially pure titanium, *Acta Materialia*, vol. 47, no. 13, pp. 3705–3720, Oct. 1999, doi: 10.1016/S1359-6454(99)00203-7.

[7] J. Rämö, Experimental Studies and Numerical Modeling of Strain Rate and Temperature Dependent Material Behavior in Dynamic Processes, Tampere, 2019.

[8] U. Messerschmidt, Dislocation dynamics during plastic deformation, in *Springer Series in Materials Science*, vol. 129, 2010.

[9] Peltonen V., High strain rate tensile testing of a nickel superalloy, Tampere, 2020.

[10] Z. Li, S. Zhao, R. O. Ritchie, and M. A. Meyers, Mechanical properties of high-entropy alloys with emphasis on face-centered cubic alloys, *Progress in Materials Science*, vol. 102, pp. 296–345, May 2019, doi: 10.1016/J.PMATSCI.2018.12.003.

[11] Güemes-Gordo A. and Martín-Piris N., *Ciencia de materiales para ingenieros*. Madrid: PEARSON EDUCACIÓN S.A., 2012.

[12] T. H. Courtney, Chapter 4: Plastic deformation in Single an Polycrystalline materials, in *Mechanical behavior of materials*, Second Edition., Waveland Press, 2005, pp. 159–160.

[13] M. A. Meyers, Experimental Techniques: Methods to Produce Dynamic Deformation, in *Dynamic Behavior of Materials*, 1994. doi: 10.1002/9780470172278.ch12.

[14] M.A. Meyers and K.K. Chawla, Shear Bands (Thermoplastic Shear Instabilities), in *Mechanical behavior of materials*, 2nd ed., Cambridge University Press, 2009, pp. 448–488.

[15] Delorme J., Extension of a finite element model to 2D for the prediction of adiabatic shear bands, Winnipeg, Manitoba, Canada, 2012.

[16] C. Zener and J. H. Hollomon, Effect of strain rate upon plastic flow of steel, *Journal of Applied Physics*, vol. 15, no. 1, 1944, doi: 10.1063/1.1707363.

[17] A. Marchand and J. Duffy, An experimental study of the formation process of adiabatic shear bands in a structural steel, *Journal of the Mechanics and Physics of Solids*, vol. 36, no. 3, 1988, doi: 10.1016/0022-5096(88)90012-9.

[18] R. F. Recht, Catastrophic thermoplastic shear, *Journal of Applied Mechanics, Transactions ASME*, vol. 31, no. 2, 1964, doi: 10.1115/1.3629585.

[19] J. Mescall, V. Weiss, Material Behavior Under High Stress and Ultrahigh Loading Rates, *Sagamore Army Materials Research Conference Proceedings*. 1983. doi: 10.1016/0378-3804(86)90073-2.

[20] S. Kuriyama and M. A. Meyers, Numerical modeling of the propagation of an adiabatic shear band, *Metallurgical Transactions A*, vol. 17, no. 3, 1986, doi: 10.1007/BF02643951.

[21] L. Seaman, D. R. Curran, and W. J. Murri, A continuum model for dynamic tensile microfracture and fragmentation, *Journal of Applied Mechanics, Transactions ASME*, vol. 52, no. 3, 1985, doi: 10.1115/1.3169106.

[22] S. Dolci, K. Carney, P. du Bois, and C. D. Kan, Adiabatic Shear Band Modeling in Inconel-718 Alloy, *16th International LS-DYNA Users Conference*, June 10-11. 2020.

[23] D. Rittel, A different viewpoint on adiabatic shear localization, *Journal of Physics D: Applied Physics*, vol. 42, no. 21, 2009, doi: 10.1088/0022-3727/42/21/214009.

[24] S. N. Medyanik, W. K. Liu, and S. Li, On criteria for dynamic adiabatic shear band propagation, *Journal of the Mechanics and Physics of Solids*, vol. 55, no. 7, 2007, doi: 10.1016/j.jmps.2006.12.006.
[25] K. Huang, A Study on the Multicomponent Alloy Systems Containing Equal-mole Elements, Taiwan, 1996.
[26] D. B. Miracle and O. N. Senkov, A critical review of high entropy alloys and related concepts, *Acta Materialia*, vol. 122. 2017. doi: 10.1016/j.actamat.2016.08.081.
[27] D. B. Miracle, J. D. Miller, O. N. Senkov, C. Woodward, M. D. Uchic, and J. Tiley, Exploration and development of high entropy alloys for structural applications, *Entropy*, vol. 16, no. 1, 2014, doi: 10.3390/e16010494.
[28] J. W. Yeh, Y. L. Chen, S. J. Lin, and S. K. Chen, High-Entropy Alloys – A New Era of Exploitation, *Materials Science Forum*, vol. 560, 2007, doi: 10.4028/www.scientific.net/msf.560.1.
[29] J. Gild *et al.*, High-Entropy Metal Diborides: A New Class of High-Entropy Materials and a New Type of Ultrahigh Temperature Ceramics, *Scientific Reports*, vol. 6, 2016, doi: 10.1038/srep37946.
[30] C. M. Rost *et al.*, Entropy-stabilized oxides, *Nature Communications*, vol. 6, 2015, doi: 10.1038/ncomms9485.
[31] S. Jiang *et al.*, A new class of high-entropy perovskite oxides, *Scripta Materialia*, vol. 142, 2018, doi: 10.1016/j.scriptamat.2017.08.040.
[32] Reed-Hill RE and Abbaschian R, *Physical metallurgy principles*, 3rd ed. Boston: PWS Publishing Company, 1994.
[33] P. Paufler, R. W. Cahn, P. Haasen (eds). Physical metallurgy 3rd revised and enlarged edition. North-Holland physics publishing, *Crystal Research and Technology*, vol. 20, no. 2, 1985, doi: 10.1002/crat.2170200229.
[34] K. G. Pradeep, N. Wanderka, P. Choi, J. Banhart, B. S. Murty, and D. Raabe, Atomic-scale compositional characterization of a nanocrystalline AlCrCuFeNiZn high-entropy alloy using atom probe tomography, *Acta Materialia*, vol. 61, no. 12, 2013, doi: 10.1016/j.actamat.2013.04.059.
[35] V. B. Ozdol *et al.*, Strain mapping at nanometer resolution using advanced nano-beam electron diffraction, *Applied Physics Letters*, vol. 106, no. 25, 2015, doi: 10.1063/1.4922994.
[36] J. Ding, Q. Yu, M. Asta, and R. O. Ritchie, Tunable stacking fault energies by tailoring local chemical order in CrCoNi medium-entropy alloys, *Proceedings of the National Academy of Sciences of the United States of America*, vol. 115, no. 36, 2018, doi: 10.1073/pnas.1808660115.
[37] D. R. Gaskell, *Introduction to the Thermodynamics of Materials*. 2012. doi: 10.4324/9780203428498.
[38] R. A. Swalin and J. Arents, Thermodynamics of Solids, *Journal of The Electrochemical Society*, vol. 109, no. 12, 1962, doi: 10.1149/1.2425309.
[39] A. R. Ruffa, Thermal potential, mechanical instability, and melting entropy, *Physical Review B*, vol. 25, no. 9, 1982, doi: 10.1103/PhysRevB.25.5895.
[40] C. A. Gearhart, Einstein before 1905: The early papers on statistical mechanics, *American Journal of Physics*, vol. 58, no. 5, 1990, doi: 10.1119/1.16478.
[41] A. Takeuchi and A. Inoue, Calculations of mixing enthalpy and mismatch entropy for ternary amorphous alloys, *Materials Transactions, JIM*, vol. 41, no. 11, 2000, doi: 10.2320/matertrans1989.41.1372.
[42] D. A. Porter, K. E. Easterling, and M. Y. Sherif, *Phase transformations in metals and alloys, third edition*. 2009.
[43] R. S. Mishra, N. Kumar, and M. Komarasamy, Lattice strain framework for plastic deformation in complex concentrated alloys including high entropy alloys, *Materials Science and Technology (United Kingdom)*, vol. 31, no. 10, 2015, doi: 10.1179/1743284715Y.0000000050.
[44] J. W. Yeh, S. Y. Chang, Y. der Hong, S. K. Chen, and S. J. Lin, Anomalous decrease in X-ray diffraction intensities of Cu-Ni-Al-Co-Cr-Fe-Si alloy systems with multi-principal elements, *Materials Chemistry and Physics*, vol. 103, no. 1, 2007, doi: 10.1016/j.matchemphys.2007.01.003.
[45] D. Turnbull, Metastable structures in metallurgy, *Metallurgical Transactions B*, vol. 12, no. 2, 1981, doi: 10.1007/BF02654454.
[46] D. Turnbull, On the gram-atomic volumes of metal-metalloid glass forming alloys, *Scripta Metallurgica*, vol. 11, no. 12, 1977, doi: 10.1016/0036-9748(77)90320-9.
[47] A. L. Greer, Confusion by design, *Nature*, vol. 366, no. 6453. 1993. doi: 10.1038/366303a0.
[48] K. Y. Tsai, M. H. Tsai, and J. W. Yeh, Sluggish diffusion in Co-Cr-Fe-Mn-Ni high-entropy alloys, *Acta Materialia*, vol. 61, no. 13, 2013, doi: 10.1016/j.actamat.2013.04.058.

[49] S. Ranganathan, Alloyed pleasures: Multimetallic cocktails, *Current Science*, vol. 85, no. 10, 2003.

[50] S. Fang, W. Chen, and Z. Fu, Microstructure and mechanical properties of twinned Al0.5CrFeNiCo0.3C0.2 high entropy alloy processed by mechanical alloying and spark plasma sintering, *Materials and Design*, vol. 54, 2014, doi: 10.1016/j.matdes.2013.08.099.

[51] J. D. Whittenberger, A Review of: 'SUPERALLOYS II' edited by CT. Sims, N.S. Stoloff, and W.C. Hagel A Wiley-Interscience Publication John Wiley & Sons, New York, NY, 1987, *Materials and Manufacturing Processes*, vol. 7, no. 3, 1992, doi: 10.1080/10426919208947432.

[52] G. D. Smith and S. J. Patel, The role of niobium in wrought precipitation-hardened nickel-base alloys, 2005. doi: 10.7449/2005/superalloys_2005_135_154.

[53] R. A. Hobbs, S. Tin, and C. M. F. Rae, A castability model based on elemental solid-liquid partitioning in advanced nickel-base single-crystal superalloys, *Metallurgical and Materials Transactions A: Physical Metallurgy and Materials Science*, vol. 36, no. 10, 2005, doi: 10.1007/s11661-005-0272-3.

[54] A. C. Yeh, Y. J. Chang, C. W. Tsai, Y. C. Wang, J. W. Yeh, and C. M. Kuo, On the solidification and phase stability of a Co-Cr-Fe-Ni-Ti high-entropy alloy, in *Metallurgical and Materials Transactions A: Physical Metallurgy and Materials Science*, 2014, vol. 45, no. 1. doi: 10.1007/s11661-013-2097-9.

[55] S. Tin and T. M. Pollock, PROCEEDINGS OF THE 2003 INTERNATIONAL SYMPOSIUM ON LIQUID METALS Predicting freckle formation in single crystal Ni-base superalloys, *Materials Science*, vol. 9, 2004.

[56] O. N. Senkov, G. B. Wilks, D. B. Miracle, C. P. Chuang, and P. K. Liaw, Refractory high-entropy alloys, *Intermetallics*, vol. 18, no. 9, pp. 1758–1765, Sep. 2010, doi: 10.1016/J.INTERMET.2010.05.014.

[57] O. N. Senkov, G. B. Wilks, J. M. Scott, and D. B. Miracle, Mechanical properties of $Nb_{25}Mo_{25}Ta_{25}W_{25}$ and $V_{20}Nb_{20}Mo_{20}Ta_{20}W_{20}$ refractory high entropy alloys, *Intermetallics*, vol. 19, no. 5, 2011.

[58] O. N. Senkov, J. M. Scott, S. v. Senkova, D. B. Miracle, and C. F. Woodward, Microstructure and room temperature properties of a high-entropy TaNbHfZrTi alloy, *Journal of Alloys and Compounds*, vol. 509, no. 20, 2011, doi: 10.1016/j.jallcom.2011.02.171.

[59] O. N. Senkov, S. V. Senkova, C. Woodward, and D. B. Miracle, Low-density, refractory multi-principal element alloys of the Cr-Nb-Ti-V-Zr system: Microstructure and phase analysis, *Acta Materialia*, vol. 61, no. 5, 2013, doi: 10.1016/j.actamat.2012.11.032.

[60] O. N. Senkov, S. V. Senkova, and C. Woodward, Effect of aluminum on the microstructure and properties of two refractory high-entropy alloys, *Acta Materialia*, vol. 68, 2014, doi: 10.1016/j.actamat.2014.01.029.

[61] O. N. Senkov, C. Woodward, and D. B. Miracle, Microstructure and Properties of Aluminum-Containing Refractory High-Entropy Alloys, *JOM*, vol. 66, no. 10, 2014, doi: 10.1007/s11837-014-1066-0.

[62] C. S. Chen, C. C. Yang, H. Y. Chai, J. W. Yeh, and J. L. H. Chau, Novel cermet material of WC/multi-element alloy, *International Journal of Refractory Metals and Hard Materials*, vol. 43, 2014, doi: 10.1016/j.ijrmhm.2013.11.005.

[63] C. M. Lin, C. W. Tsai, S. M. Huang, C. C. Yang, and J. W. Yeh, New TiC/Co1.5CrFeNi1.5Ti0.5 Cermet with Slow TiC Coarsening During Sintering, *JOM*, vol. 66, no. 10, 2014, doi: 10.1007/s11837-014-1095-8.

[64] Y. L. Chou, J. W. Yeh, and H. C. Shih, Effect of molybdenum on the pitting resistance of Co 1.5CrFeNi1.5Ti0.5Mox alloys in chloride solutions, *Corrosion*, vol. 67, no. 8, 2011, doi: 10.5006/1.3613646.

[65] P. K. Huang, J. W. Yeh, T. T. Shun, and S. K. Chen, Multi-principal-element alloys with improved oxidation and wear resistance for thermal spray coating, *Advanced Engineering Materials*, vol. 6, no. 1–2, 2004, doi: 10.1002/adem.200300507.

[66] T. K. Chen, T. T. Shun, J. W. Yeh, and M. S. Wong, Nanostructured nitride films of multi-element high-entropy alloys by reactive DC sputtering, *Surface and Coatings Technology*, vol. 188–189, no. 1-3 SPEC.ISS., 2004, doi: 10.1016/j.surfcoat.2004.08.023.

[67] M.-H. Tsai *et al.*, Thermal Stability and Performance of NbSiTaTiZr High-Entropy Alloy Barrier for Copper Metallization, *Journal of The Electrochemical Society*, vol. 158, no. 11, 2011, doi: 10.1149/2.056111jes.

[68] T. Egami, W. Guo, P. D. Rack, and T. Nagase, Irradiation resistance of multicomponent alloys, in *Metallurgical and Materials Transactions A: Physical Metallurgy and Materials Science*, 2014, vol. 45, no. 1. doi: 10.1007/s11661-013-1994-2.

[69] T. Nagase *et al.*, MeV electron-irradiation-induced structural change in the bcc phase of Zr-Hf-Nb alloy with an approximately equiatomic ratio, *Intermetallics*, vol. 38, 2013, doi: 10.1016/j.intermet.2013.02.009.

[70] T. Nagase, P. D. Rack, J. H. Noh, and T. Egami, In-situ TEM observation of structural changes in nano-crystalline CoCrCuFeNi multicomponent high-entropy alloy (HEA) under fast electron irradiation by high voltage electron microscopy (HVEM), *Intermetallics*, vol. 59, 2015, doi: 10.1016/j.intermet.2014.12.007.

[71] D. Hull and D. J. Bacon, Dislocations in Face-centered Cubic Metals, in *Introduction to Dislocations*, 2011. doi: 10.1016/b978-0-08-096672-4.00005-0.

[72] M. A. Meyers, O. Vöhringer, and V. A. Lubarda, The onset of twinning in metals: A constitutive description, *Acta Materialia*, vol. 49, no. 19, 2001, doi: 10.1016/S1359-6454(01)00300-7.

[73] N. Kumar *et al.*, High strain-rate compressive deformation behavior of the Al0.1CrFeCoNi high entropy alloy, *Materials and Design*, vol. 86, 2015, doi: 10.1016/j.matdes.2015.07.161.

[74] Z. Li, S. Zhao, H. Diao, P. K. Liaw, and M. A. Meyers, High-velocity deformation of Al0.3 CoCrFeNi high-entropy alloy: Remarkable resistance to shear failure, *Scientific Reports*, vol. 7, 2017, doi: 10.1038/srep42742.

[75] M. A. Meyers, Z. Li, S. Zhao, B. Wang, Y. Liu, and P. K. Liaw, Shear localization of fcc high-entropy alloys, in *EPJ Web of Conferences*, 2018, vol. 183. doi: 10.1051/epjconf/201818303028.

[76] Y. Zhang, J. Li, J. Wang, W. Y. Wang, H. Kou, and E. Beaugnon, Temperature dependent deformation mechanisms of Al0.3CoCrFeNi high-entropy alloy, starting from serrated flow behavior, *Journal of Alloys and Compounds*, vol. 757, 2018, doi: 10.1016/j.jallcom.2018.04.305.

[77] H. Y. Yasuda, K. Shigeno, and T. Nagase, Dynamic strain aging of Al0.3CoCrFeNi high entropy alloy single crystals, *Scripta Materialia*, vol. 108, 2015, doi: 10.1016/j.scriptamat.2015.06.022.

[78] M. R. Staker, The relation between adiabatic shear instability strain and material properties, *Acta Metallurgica*, vol. 29, no. 4, 1981, doi: 10.1016/0001-6160(81)90151-6.

[79] L. W. Meyer, L. Krüger, and T. Halle, Strength and failure characterisation and behaviour under impact loading, in *Impact engineering and application*, Jul. 2001.

[80] T. W. Wright, The physics and mathematics of ASB, *Cambridge University Press*, New York, 2002.

[81] J. P. Ansart and R. Dormeval, Adiabatic shearing in martensitic steels, in *Impact loading and dynamic behavior of materials*, vol. 2, H. D. K. and L. W. M. C. Y. Chiem, Ed. DGM, 1988.

[82] M. A. Meyers, Y. J. Chen, F. D. S. Marquis, and D. S. Kim, High-strain, high-strain-rate behavior of tantalum, *Metallurgical and Materials Transactions A*, vol. 26, no. 10, 1995, doi: 10.1007/BF02669407.

[83] S. M. Walley, D. D. Radford, and D. J. Chapman, The effect of aspect ratio on the compressive high rate deformation of three metallic alloys, in *Journal De Physique. IV: JP*, 2006, vol. 134. doi: 10.1051/jp4:2006134131.

[84] C. R. Siviour and S. M. Walley, Inertial and frictional effects in dynamic compression testing, in *The Kolsky-Hopkinson Bar Machine: Selected Topics*, 2018. doi: 10.1007/978-3-319-71919-1_8.

[85] J. M. Park *et al.*, Strain rate effects of dynamic compressive deformation on mechanical properties and microstructure of CoCrFeMnNi high-entropy alloy, *Materials Science and Engineering A*, vol. 719, pp. 155–163, Mar. 2018, doi: 10.1016/j.msea.2018.02.031.

[86] D. Rittel, G. Ravichandran, and S. Lee, Large strain constitutive behavior of OFHC copper over a wide range of strain rates using the shear compression specimen, *Mechanics of Materials*, vol. 34, no. 10, 2002, doi: 10.1016/S0167-6636(02)00164-3.

[87] D. Rittel, S. Lee, and G. Ravichandran, A shear-compression specimen for large strain testing, *Experimental Mechanics*, vol. 42, no. 1, 2002, doi: 10.1007/bf02411052.

[88] A. Dorogoy, D. Rittel, and A. Godinger, Modification of the Shear-Compression Specimen for Large Strain Testing, *Experimental Mechanics*, vol. 55, no. 9, 2015, doi: 10.1007/s11340-015-0057-6.

[89] R. Fadida, A. Shirizly, and D. Rittel, Static and dynamic shear-compression response of additively manufactured Ti6Al4V specimens with embedded voids, *Mechanics of Materials*, vol. 147, 2020, doi: 10.1016/j.mechmat.2020.103413.

[90] A. Dorogoy, D. Rittel, and A. Godinger, A Shear-Tension Specimen for Large Strain Testing, *Experimental Mechanics*, vol. 56, no. 3, 2016, doi: 10.1007/s11340-015-0106-1.

[91] A.R. Dowling, J. Harding, and J.D Campbell, Dynamic Punching of Metals, *J Inst Metals*, vol. 98, 1970.

[92] W. G. Ferguson, F. E. Hauser, and J. E. Dorn, Dislocation damping in zinc single crystals, *British Journal of Applied Physics*, vol. 18, no. 4, 1967, doi: 10.1088/0508-3443/18/4/304.

[93] J. D. Campbell and W. G. Ferguson, The temperature and strain-rate dependence of the shear strength of mild steel, *Philosophical Magazine*, vol. 21, no. 169, 1970, doi: 10.1080/14786437008238397.
[94] J. Harding, J. Huddart, The use of the double-notch shear test in determining the mechanical properties of uranium at very high rates of strain, United Kingdom: Institute of Physics, 1980.
[95] B. Budiwantoro, I. Faizah, D. A. Prabowo, B. Febrinawarta, and M. A. Kariem, Results comparison for hat-shaped, double-notch and punch testing of split Hopkinson shear bar technique, *Journal of Engineering and Technological Sciences*, vol. 51, no. 6, 2019, doi: 10.5614/j.eng.technol.sci.2019.51.6.5.
[96] L. W. Meyer and F. Pursche, Experimental Methods, in *Adiabatic Shear Localization*, 2012. doi: 10.1016/B978-0-08-097781-2.00002-2.
[97] F. F. Shi, R. Merle, B. Hou, J. G. Liu, Y. L. Li, and H. Zhao, A critical analysis of plane shear tests under quasi-static and impact loading, *International Journal of Impact Engineering*, vol. 74, 2014, doi: 10.1016/j.ijimpeng.2014.06.012.
[98] B. Budiwantoro, M. A. Kariem, and B. Febrinawarta, The Influence of Shear Angles on the Split Hopkinson Shear Bar Testing, *International Journal of Impact Engineering*, vol. 149, 2021, doi: 10.1016/j.ijimpeng.2020.103787.
[99] G. T. Gray, K. S. Vecchio, and V. Livescu, Compact forced simple-shear sample for studying shear localization in materials, *Acta Materialia*, vol. 103, 2016, doi: 10.1016/j.actamat.2015.09.051.
[100] A. Arab, Y. Guo, Q. Zhou, and P. Chen, A new S-shape specimen for studying the dynamic shear behavior of metals, *Metals*, vol. 9, no. 8, 2019, doi: 10.3390/met9080838.
[101] N. Yan, Z. Li, Y. Xu, and M. A. Meyers, Shear localization in metallic materials at high strain rates, *Progress in Materials Science*, vol. 119. 2021. doi: 10.1016/j.pmatsci.2020.100755.
[102] B. Jia, A. Rusinek, R. Pesci, R. Bernier, S. Bahi, and P. Wood, A novel technique for dynamic shear testing of bulk metals with application to 304 austenitic stainless steel, *International Journal of Solids and Structures*, vol. 204–205, 2020, doi: 10.1016/j.ijsolstr.2020.08.019.
[103] M. Isakov, J. Seidt, K. Östman, A. Gilat, and V. T. Kuokkala, Characterization of a ferritic stainless sheet steel in simple shear and uniaxial tension at different strain rates, in *ASME 2011 International Mechanical Engineering Congress and Exposition, IMECE 2011*, 2011, vol. 8. doi: 10.1115/imece2011-63141.
[104] K. A. Gardner, J. D. Seidt, M. Isakov, and A. Gilat, Characterization of sheet metals in shear over a wide range of strain rates, in *Conference Proceedings of the Society for Experimental Mechanics Series*, 2014, vol. 1. doi: 10.1007/978-3-319-00771-7_38.
[105] L. W. Meyer and S. Manwaring, Critical Adiabatic Shear Strength of Low Alloyed Steel Under Compressive Loading., 1986.
[106] E. K. Cerreta *et al.*, Microstructural examination of quasi-static and dynamic shear in high-purity iron, *International Journal of Plasticity*, vol. 40, 2013, doi: 10.1016/j.ijplas.2012.06.005.
[107] R. G. O'Donnell and R. L. Woodward, Instability during high strain rate compression of 2024 T351 aluminium, *Journal of Materials Science*, vol. 23, no. 10, 1988, doi: 10.1007/BF00540498.
[108] E. K. Cerreta, I. J. Frank, G. T. Gray, C. P. Trujillo, D. A. Korzekwa, and L. M. Dougherty, The influence of microstructure on the mechanical response of copper in shear, *Materials Science and Engineering A*, vol. 501, no. 1–2, 2009, doi: 10.1016/j.msea.2008.10.029.
[109] J. Peirs, P. Verleysen, J. Degrieck, and F. Coghe, The use of hat-shaped specimens to study the high strain rate shear behaviour of Ti-6Al-4V, *International Journal of Impact Engineering*, vol. 37, no. 6, 2010, doi: 10.1016/j.ijimpeng.2009.08.002.
[110] S. Nemat-Nasser, J. B. Isaacs, and M. Liu, Microstructure of high-strain, high-strain-rate deformed tantalum, *Acta Materialia*, vol. 46, no. 4, 1998, doi: 10.1016/S1359-6454(97)00746-5.
[111] Y. J. Chen, M. A. Meyers, and V. F. Nesterenko, Spontaneous and forced shear localization in high-strain-rate deformation of tantalum, *Materials Science and Engineering A*, vol. 268, no. 1–2, 1999, doi: 10.1016/s0921-5093(99)00110-0.
[112] Q. Xue and I. T. Gray, Development of adiabatic shear bands in annealed 316L stainless steel: Part I. Correlation between evolving microstructure and mechanical behavior, *Metallurgical and Materials Transactions A: Physical Metallurgy and Materials Science*, vol. 37, no. 8, 2006, doi: 10.1007/BF02586217.
[113] Q. Xue, E. K. Cerreta, and G. T. Gray, Microstructural characteristics of post-shear localization in cold-rolled 316L stainless steel, *Acta Materialia*, vol. 55, no. 2, 2007, doi: 10.1016/j.actamat.2006.09.001.

[114] C. A. Bronkhorst, E. K. Cerreta, Q. Xue, P. J. Maudlin, T. A. Mason, and G. T. Gray, An experimental and numerical study of the localization behavior of tantalum and stainless steel, *International Journal of Plasticity*, vol. 22, no. 7, 2006, doi: 10.1016/j.ijplas.2005.10.002.
[115] Z. Li, S. Zhao, S. M. Alotaibi, Y. Liu, B. Wang, and M. A. Meyers, Adiabatic shear localization in the CrMnFeCoNi high-entropy alloy, *Acta Materialia*, vol. 151, 2018, doi: 10.1016/j.actamat.2018.03.040.
[116] K.-H. Hartmann, H.-D. Kunze, and L. W. Meyer, Metallurgical Effects on Impact Loaded Materials, in *Shock Waves and High-Strain-Rate Phenomena in Metals*, 1981. doi: 10.1007/978-1-4613-3219-0_21.
[117] L. F. Liu, L. H. Dai, Y. L. Bai, and B. C. Wei, Initiation and propagation of shear bands in Zr-based bulk metallic glass under quasi-static and dynamic shear loadings, *Journal of Non-Crystalline Solids*, vol. 351, no. 40–42, 2005, doi: 10.1016/j.jnoncrysol.2005.07.030.
[118] R. Clos, U. Schreppel, and P. Veit, Experimental investigation of adiabatic shear band formation in steels, *Journal De Physique. IV : JP*, vol. 10, no. 9, 2000, doi: 10.1051/jp4:2000943.
[119] R. Clos, U. Schreppel, and P. Veit, Temperature, microstructure and mechanical response during shear-band formation in different metallic materials, *Journal de Physique IV (Proceedings)*, vol. 110, 2003, doi: 10.1051/jp4:20030679.
[120] Dassault Systèmes, ABAQUS 6.14 Getting Started with Abaqus: Interactive Edition, *ABAQUS 6.14 Getting Started*, 2014.
[121] Simulia, Abaqus 6.11 Theory Manual, *Providence, RI, USA: DS SIMULIA Corp*, 2017.
[122] Ajithramesh, R. Mathews, A. Pillai, and U. Divakaran, Finite Element Modeling of a Thin Circular Disc Manufactured by Forming Process used in Cyclic Loading and Unloading Applications, in *Materials Today: Proceedings*, 2019, vol. 22. doi: 10.1016/j.matpr.2020.03.434.
[123] M. Žmindák, Z. Pelagić, P. Pastorek, M. Močilan, and M. Vybošťok, Finite element modelling of high velocity impact on plate structures, in *Procedia Engineering*, 2016, vol. 136. doi: 10.1016/j.proeng.2016.01.191.
[124] P. Thyssen and S. Wenmackers, *Abaqus analysis user's manual v6.14*. 2014.
[125] H. Kolsky, An investigation of the mechanical properties of materials at very high rates of loading, *Proceedings of the Physical Society. Section B*, vol. 62, no. 11, 1949, doi: 10.1088/0370-1301/62/11/302.
[126] M. Meyers, *Experimental Techniques: Methods to Produce Dynamic Deformation*, Anonymous. Dynamic Behavior of Materials, 1994.
[127] W. W. Chen and B. Song, *Split Hopkinson (Kolsky) Bar: Design, Testing and Applications.* 2013.
[128] Hopkinson techniques for dynamic recovery experiments, *Proceedings of the Royal Society of London. Series A: Mathematical and Physical Sciences*, vol. 435, no. 1894, 1991, doi: 10.1098/rspa.1991.0150.
[129] W. E. Baker and C. H. Yew, Strain-rate effects in the propagation of torsional plastic waves, *Journal of Applied Mechanics, Transactions ASME*, vol. 33, no. 4, 1964, doi: 10.1115/1.3625202.
[130] Y. Zhou, Q. Fang, and L. Chen, A preliminary research on the rotating-wheel TSHB testing system, in *In Proceedings of 11th National Conference on Explosion Mechanics*, 2016, p. 248.
[131] X. Jiang, Y. Xiao, L. Chen, Q. Fang, and Y. Zhou, An electromagnetic driven torsional split hopkinson bar, in *Proceedings of 2nd International Conference on Impact Loading of Structures and Materials*, 2018, pp. 103–105.
[132] X. Nie, R. Prabhu, W. W. Chen, J. M. Caruthers, and T. Weerasooriya, A Kolsky Torsion Bar Technique for Characterization of Dynamic Shear Response of Soft Materials, *Experimental Mechanics*, vol. 51, no. 9, 2011, doi: 10.1007/s11340-011-9481-4.
[133] J. Duffy, J. D. Campbell, and R. H. Hawley, On the use of a torsional split hopkinson bar to study rate effects in 1100-0 Aluminum, *Journal of Applied Mechanics, Transactions ASME*, vol. 38, no. 1, 1971, doi: 10.1115/1.3408771.
[134] L. Krstulović-Opara, M. Surjak, M. Vesenjak, Z. Tonković, J. Kodvanj, and Ž. Domazet, Comparison of infrared and 3D digital image correlation techniques applied for mechanical testing of materials, *Infrared Physics and Technology*, vol. 73, pp. 166–174, Nov. 2015, doi: 10.1016/j.infrared.2015.09.014.
[135] T. Vermeij and J. P. M. Hoefnagels, A consistent full-field integrated DIC framework for HR-EBSD, *Ultramicroscopy*, vol. 191, 2018, doi: 10.1016/j.ultramic.2018.05.001.
[136] A. D. Kammers and S. Daly, Digital Image Correlation under Scanning Electron Microscopy: Methodology and Validation, doi: 10.1007/s11340-013-9782-x.
[137] S. A. Hall, N. Lenoir, G. Viggiani, J. Desrues, and P. Bésuelle, Strain localisation in sand under triaxial loading: Characterisation by x-ray micro tomography and 3D Digital Image Correlation, 2009.

[138] M. Mehdikhani, C. Breite, Y. Swolfs, M. Wevers, S. v. Lomov, and L. Gorbatikh, Combining digital image correlation with X-ray computed tomography for characterization of fiber orientation in unidirectional composites, *Composites Part A: Applied Science and Manufacturing*, vol. 142, 2021, doi: 10.1016/j.compositesa.2020.106234.
[139] S. Y. Wu *et al.*, Dynamic shear localization of a titanium alloy under high-rate tension characterized by x-ray digital image correlation, *Materials Characterization*, vol. 137, 2018, doi: 10.1016/j.matchar.2018.01.011.
[140] N. McCormick and J. Lord, Digital image correlation, *Materials Today*, vol. 13, no. 12, 2010, doi: 10.1016/S1369-7021(10)70235-2.
[141] J. Górszczyk, K. Malicki, and T. Zych, Application of digital image correlation (DIC) method for road material testing, *Materials*, vol. 12, no. 15, 2019, doi: 10.3390/ma12152349.
[142] I. Jones *et al.*, A Good Practices Guide for Digital Image Correlation, *International Digital Image Correlation Society*, p. 94, 2018, [Online]. Available: http://idics.org/guide/
[143] Tampere University, Impact, Multiscale Materials Testing Research Group, https://research.tuni.fi/impact/equipment/digital-image-correlation/.
[144] W. LePage, A Practical Guide to DIC.
[145] A. Soltani *et al.*, An Optical Method for the In-Vivo Characterization of the Biomechanical Response of the Right Ventricle, *Scientific Reports*, vol. 8, no. 1, 2018, doi: 10.1038/s41598-018-25223-z.
[146] Craig Hillman, Digital Image Correlation: A Key Technique for Materials Characterization, *Ansys Blog*, Jan. 08, 2020.
[147] M. Sasso, E. Mancini, G. Chiappini, F. Sarasini, and J. Tirillò, Application of DIC to Static and Dynamic Testing of Agglomerated Cork Material, *Experimental Mechanics*, vol. 58, no. 7, 2018, doi: 10.1007/s11340-017-0369-9.
[148] J. L. Smith, J. D. Seidt, and A. Gilat, Full-field determination of the taylor-quinney coefficient in tension tests of Ti-6AL-4V at strain rates up to 7000 s−1, in *Conference Proceedings of the Society for Experimental Mechanics Series*, 2019, vol. 12. doi: 10.1007/978-3-319-97481-1_20.
[149] C. Ran, Q. Liu, P. Chen, and Q. Chen, Dynamic forced shear characteristics of Ti-6Al-4V alloy using flat hat-shaped specimen, *Engineering Fracture Mechanics*, vol. 238, 2020, doi: 10.1016/j.engfracmech.2020.107286.
[150] B. Wang, X. Xiao, V. P. Astakhov, and Z. Liu, The effects of stress triaxiality and strain rate on the fracture strain of Ti6Al4V, *Engineering Fracture Mechanics*, vol. 219, 2019, doi: 10.1016/j.engfracmech.2019.106627.
[151] A. Stumpf, J. P. Malet, and C. Delacourt, Correlation of satellite image time-series for the detection and monitoring of slow-moving landslides, *Remote Sensing of Environment*, vol. 189, 2017, doi: 10.1016/j.rse.2016.11.007.
[152] B. Gludovatz, E. P. George, and R. O. Ritchie, Processing, Microstructure and Mechanical Properties of the CrMnFeCoNi High-Entropy Alloy, *JOM*, vol. 67, no. 10, 2015, doi: 10.1007/s11837-015-1589-z.
[153] Support, (2018, November 8), Units in Abaqus (1), retrieved from https://caeassistant.com/blog/units-in-abaqus-1/
[154] Z. Xu, X. Ding, W. Zhang, and F. Huang, A novel method in dynamic shear testing of bulk materials using the traditional SHPB technique, *International Journal of Impact Engineering*, vol. 101, pp. 90–104, Mar. 2017, doi: 10.1016/J.IJIMPENG.2016.11.012.
[155] H. Ghadbeigi, C. Pinna, and S. Celotto, Quantitative Strain Analysis of the Large Deformation at the Scale of Microstructure: Comparison between Digital Image Correlation and Microgrid Techniques, *Experimental Mechanics*, vol. 52, no. 9, 2012, doi: 10.1007/s11340-012-9612-6.
[156] Shao-Pu Tsai, Yu-Ting Tsai et al. High-entropy CoCrFeMnNi alloy subjected to high-strain-rate compressive deformation, *Materials Characterization*, vol. 148, 2019, https://doi.org/10.1016/j.matchar.2018.10.028.
[157] Muskeri, S., Gwalani, B., Jha, S. et al. Excellent ballistic impact resistance of $Al_{0.3}$CoCrFeNi multi-principal element alloy with unique bimodal microstructure. *Sci Rep*, 11**,** 22715 (2021). https://doi.org/10.1038/s41598-021-02209-y
[158] C. T. Wang et al., Strain Rate Effects on the Mechanical Properties of an AlCoCrFeNi High-Entropy Alloy, *Metals and Materials International*, vol. 27, no. 7, 2021, doi: 10.1007/s12540-020-00920-5.